UNIVERSITÀ
DI PAVIA

UNIVERSITY OF PAVIA

FACULTY OF ENGINEERING

DEPARTMENT OF
ELECTRICAL, COMPUTER AND BIOMEDICAL ENGINEERING

PHD SCHOOL IN
ELECTRONIC, COMPUTER SCIENCE AND ELECTRICAL
ENGINEERING

Microwave Radar Systems for Cryosphere Monitoring

Candidate: Martina Lodigiani

Supervisor: Prof. Marco Pasian

XXXVI cycle, 2023

There was nothing in sight except falling snow, and Moomintroll was caught by the same kind of excitement he used to feel at times when he was wading out for a swim. He threw off his bath-gown, and himself headlong in to a snowdrift. “So that’s winter too!” he thought. “You can even like it!”

Moominland Midwinter

Contents

List of Figures

List of Tables

List of Acronyms

AINEVA Interregional association for coordination and documentation of snow and avalanche problems. 36, 39

ARC Arctic Research Center. 71

ARPA Agenzia Regionale per la Protezione Ambientale - Regional Agency for Environmental Protection. 36, 53

ASI Agenzia Spaziale Italiana - Italian Space Agency. 51, 64

AtG Above the Ground. 22, 23, 89, 109, 111

BW Bandwidth. 81, 109

CMP Common Mid-Point. 23

EM Electro-Magnetic. 22, 28, 31, 41, 62, 89, 90, 92, 93, 94, 97, 113

EO Earth Observation. 95

FMI Finnish Meteorological Istitute - Ilmatieteen laitos. 71, 72

GB-SAR Ground Based SAR. 22

GND GrouND. 111

GNSS Global Navigation Satellite System. 80

GPR Ground Penetrating Radar. 22, 23, 53, 68, 69, 80, 82, 85, 86, 113, 115

IHP International Hydrological Programme. 36

LGM Last Glacial Maximum. 77

LNA Low Noise Amplifier. 34

LWC Liquid Water Content. 22, 38, 48, 62, 63, 65, 66, 67, 69, 70, 71, 72, 73, 85, 90, 91, 92, 97, 98, 101, 105, 113, 114

OGS Optical-equivalent Grain Size. 37

OSB Oriented Strand Board. 110, 111

PEC Perfect Electric Conductor. 92, 95

PIFA Planar Inverted-F Antenna. 31, 81, 115

PP Precipitation Particle. 41

RCS Radar Cross Section. 63, 64, 95, 96

RF Radio Frequency. 27

RMS Root Mean Square. 95, 96, 98, 101

RPAS Remotely Piloted Aircraft System. 80

SAR Syntetic Apertur Radar. 22, 91, 95, 98

SLF Federal Institute for Snow and Avalanche Research. 66, 69, 70, 72, 73, 97, 105, 114

SoC System on Chip. 23, 109

SOLT Short, Open, Load, Through Calibration. 34

SWE Snow Water Equivalent. 22, 51, 53, 54, 60, 91, 101, 113, 114

ToF Time of Flight. 22, 23, 29, 35, 81

TRL Through Reflect Line. 34

UAV Unmanned Aerial Vehicle. 21, 116

UHF Ultra High Frequency. 31, 81

UNESCO United Nations Educational, Scientific and Cultural Organization. 36

UNIMIB University of Milano-Bicocca. 53, 68

UWB Ultra Wide Band. 23, 89, 109, 110, 116

VNA Vector Network Analyzer. 27, 34, 35, 54, 81, 116

WSL Swiss Federal Institute for Forest, Snow and Landscape Research. 66, 97, 105

Abstract

The cryosphere is the portion of the Earth covered by frozen water and experiencing temperatures below 0°C for at least part of the year. In latest years, the warming temperatures and the change of the climate act to reduce the mass of permanent ice and to limit the creation of new snow and ice. This causes several problems, such as scarce fresh water availability, natural disasters and modification of several landscapes, especially in the mid-latitude areas. The accurate and continuous monitoring of these regions has become crucial to understand the dynamics of ongoing changes and to assess the associated environmental and socio-economic impacts. Several technological methods have been developed, despite one of the most used technique is still the manual analysis. For a non-invasive observation, photogrammetry, Global Navigation Satellite System (GNSS) or Remotely Piloted Aircraft System (RPAS) are used for small areas, while satellite images are employed for bigger areas. Also Ground Penetrating Radar (GPR) and seismic methods are powerful instruments, able to detect different layers. In particular, radar allows to acquire high spatial and temporal resolution data, and it can be tailored to supply accurate information about different cryospheric bodies. Indeed, by using different frequencies, it can penetrate and interact with the medium in different way. The principal parameters which can be investigated by means of radar systems are the depth of the medium D (also expressed as HS), either snow or ice, and its density ρ, the Liquid Water Content (LWC), which measure the percentage of humidity in the medium, and the so called Snow Water Equivalent (SWE), i.e. how much water is stored in it. Other parameters, e.g. the temperature or the hardness, cannot be measured, even if some attempts to retrieve them from the density were done in literature [1][2]. A standard GPR can obtain such information, but it needs the support of assumptions, external measurements, or very complicated techniques barely applicable in the field. In order to overcome such limitations and improve the accuracy of the measurements, a novel ground-based radar system called Snowave has been developed. Snowave is a dual receiver radar architecture able to compute the depth and the dielectric constant of a medium without any external aids or assumptions, and thus solving the ambiguity in determining the wave velocity within the medium. This principle was already shown in previous works [3][4], studying the feasibility of the concept, and proving it with few dry snow measurements in the field. In this work, a more accurate investigation on the applicability is presented, moving through several snow conditions (various depths and densities), including also wet snow. Indeed, this system, Snowave, thanks

to its light and compact profile making it portable in any environment, has been tested in the Alps in several conditions, from dry and soft [5] to wet and dense [6][7] snow. Especially for this last condition, different types of measurement have been done. Punctual and instantaneous measurements have been carried out in the Alps, following the same idea of the dry snow monitoring, while a couple of attempts to investigate the small variation occurring during the melting-refreeze cycle (i.e. daily variation from dry to slightly wet snowpack) produced successful results, proved also by an extensively 15-days campaign in Arctic environment.
One big enhancement of the system is related to the possibility to monitor not only snow coverage, but also glaciers. Indeed, few works have been done in this direction: in order to fully investigate such dense medium, with a relatively high dielectric constant and very high thickness, a different type of radiator was needed. Some custom-made antennas were simulated, produced and then tested in glacial environment, returning a complete result about the condition of the glacier, with more information with respect to a standard GPR.
In addition to the work relative to the field campaign, a preparatory study on the problems occurring using an above-the-ground configuration has been done, from an attempt with a lighter and smaller radar used on a fixed platform, to the development of a combined analytical and full-wave model to predict the effect of the surface roughness on the backscattering when using an off-nadir configuration. In this case, the model was cross-checked with satellite backscattering data. However, this methodology can also be extended to systems operating in close proximity to the ground, e.g. with Snowave on a fixed or a mobile platform.
In conclusion, this thesis presents the validation of a radar system for cryospheric monitoring, able to provide insights into the dynamics of the cryosphere and to enhance the ability to predict and mitigate climate change impacts and/or natural hazards.

Keyword:
Climate change, dry snow, glacier monitoring, ground-based radar, liquid water content (LWC), melting process, radar, snow density, snow monitoring, snow water equivalent (SWE), snowpack, surface roughness, wet snow

Chapter 1

Introduction

The cryosphere, derived from the Greek words "κρύος" (kryos) meaning "cold" and "σφαῖρα" (sphaira) "globe," represents the portion of the Earth's hydrosphere where water is frozen and in solid form. It comprises different natural bodies, such as snow, ice formations and permafrost. This intricate system plays a fundamental role in the Earth's climate and hydrological cycles, influencing weather patterns and sea levels. Understanding the cryosphere is crucial in the context of climate change, as its dynamics are highly sensitive to temperature fluctuations.

1.1 Importance of the cryopshere

The cryosphere is a crucial part of the Earth environment, comprising the natural bodies which exist at temperature below 0°C, such as snow cover, glaciers, ice sheet, ice shelves, ice caps, sea ice, lake ice, river ice and frozen ground, including permafrost, interacting and, in some cases, overlapping with the hydrosphere [8]. It has a global extension and it can be found in regions with very low temperatures, such as the poles (e.g. Arctic, Antarctica, Greenland) and high-altitude areas like in the mountains, as the water needs to be at a temperature below 0°C [9]. Figure 1.1 illustrates the global distribution of the cryosphere, specifying its different components. However, this map is not static, as it changes rapidly following the temperature fluctuations and the local and temporal weather conditions, especially regarding the wind behavior. Even if most of the ice volume is located in Antarctica, the northern hemisphere has the largest surface extension, in particular during winter (considering also the seasonal snow coverage), occupying ∼13% of the Earth surface [10][11]. Being part of the hydrosphere, the cryosphere stores a large amount of fresh water, which is the 75% of the on-land water and only the 2.5% of the total amount of water on the planet Earth[1]. It could be found in great quantity especially in snow, glaciers and ice sheets. Indeed, most of the Earth's fresh water resides in two major ice sheets, Antarctica and Greenland[12]. Freshwater is essential for the population, as it can be used

[1]The rest of the water presented on the planet can be found in salty water, mostly in oceans.

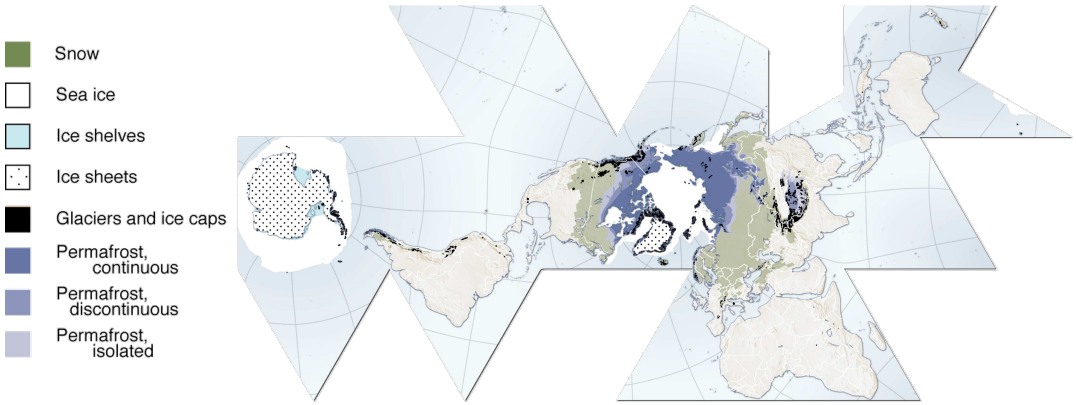

Figure 1.1: Global distribution of the cryospheric components (Credit: Hugo Ahlenius, UNEP/GRID-Arendal, 2016)

for several applications. Among them, the hydroelectric power generated with it serves as the major source of energy for remote mountainous villages, difficult to reach with other kind of energy. Additionally, in certain instances, it may also provide power to nearby regions [13]–[16]. Specifically in plains areas, the seasonal availability of fresh water significantly impacts crop irrigation levels. In most cases, this water is sourced from the thawing of cryospheric components, especially snow, which is stored in dams and released through dedicated infrastructures [17]–[19].

The climate change strongly affects the availability of fresh water, and the cryosphere in general. Indeed, the Earth's climate system is intricately linked to the cryosphere, influencing surface energy, moisture flows, clouds, precipitation, hydrology and atmospheric and oceanic circulation [20][21]. These links are related to the physical properties of the cryospheric bodies, such as their high surface reflectivity, called albedo, and the exchange of latent heat during the phase transitions, influencing the energy balance of the planet, seen at the surface level. The presence or absence of snow and ice in polar areas is significantly influenced by the temperature difference between latitudes, affecting also winds and ocean currents. This creates a positive feedback loop, amplifying changes in temporary bodies, such as seasonal snow or sea ice, which change their presence and extension during the seasons. On the other hand, elements like glaciers and permafrost, thanks to their durability throughout the years, help average out short-term variations, making them indicators of climate change [20].

Therefore, monitoring the cryospheric components can help to trace and evaluate the effect of the climate change, as well as giving a prevision of the freshwater stored in the cryospheric components.

In addition, monitoring the cryosphere is also used to predict and, if possible, mitigate environmental risks. The natural metamorphosis of such bodies is a process leading, in most of the cases, to an unstable condition, which needs to be controlled in order to avoid disasters. Indeed, snow avalanches and collapse of ice and rocks are frequent processes in mountainous areas, and it is necessary to study the evolution of such bodies to produce risk bulletins and taking some

countermeasures, e.g. avalanche protection structures or roadblocks.
In the next section, an overview of the state of the art relative to the monitoring techniques is presented.

1.2 Monitoring techniques: state of the art

The monitoring and understanding of the cryosphere, comprising snow and ice-covered regions, play a crucial role in understanding and predicting global climate dynamics. The monitoring activities can be diverse:

- ground-based observations - this refers to data collected through direct measurements on the ground. Scientists and researchers use specialized instruments to measure parameters such as snow depth, density, and temperature. These on-site measurements provide valuable information about local cryospheric conditions and are essential for validating and calibrating remote sensing data. For snow investigation, in particular, the manual analysis done on a site is the standard method to retrieve information about the snow coverage condition.

- remote sensing observations - remote sensing involves the use of satellite or aerial technology, the so called Unmanned Aerial Vehicle (UAV), to collect data from a distance. Various sensors on satellites can measure properties of the cryosphere, including snow cover extent, ice thickness, and changes in glaciers. Remote sensing provides a broader perspective, covering large and often inaccessible areas, and is functional in monitoring long-term trends and changes in the cryosphere.

- modelization - mathematical models are used to simulate the behavior of the cryosphere and related processes. These models incorporate data from ground-based observations and remote sensing to predict future changes in snow and ice-covered regions. By understanding the complex interactions within the cryosphere, these models help in forecasting scenarios related to climate change, such as sea level rise due to melting glaciers or changes in regional weather patterns.

The combination of these approaches is necessary to entirely understand the cryosphere. The monitoring of the cryosphere can be conducted using various technological instruments, including sensors, photogrammetry, radars and other instruments [22]. All these tools provide data for understanding the complex dynamics of the cryosphere and its responses to climate change.
Among all the possible tools, microwave instruments represent smart options in cryospheric monitoring demonstrating their capability not only to penetrate snow and ice but also to navigate through clouds, enabling investigations even in challenging weather conditions from remote platforms [23].

Operating within the frequency range from 300 MHz to 300 GHz, these instruments offer significant advantages for studying the cryosphere. Indeed, microwaves have the capability to penetrate snow and ice to a certain extent. The frequency used in these instruments plays a crucial role, as it influences the depth of penetration and the information acquired. Their sensitivity to the dielectric properties of materials, including snow and ice, provides insights to describe the medium. By analyzing how microwaves interact with different snow and ice conditions, it is possible to deduce essential parameters such as $SnowWaterEquivalent(SWE)$ and density. These parameters hold significant importance for hydrological studies, forecasts, and safety assessments.
Among the various microwave systems, radars are frequently used for monitoring purposes. Radars operate by emitting Electro-Magnetic (EM) waves at microwave frequencies and analyzing the time taken for the signal to return after reflection. Depending on the type of monitoring, the wave has to penetrate different medium: for ground-based radars, the wave propagates within the medium, while, for Above the Ground (AtG) configurations, the wave is directed toward the Earth's surface. In the latter case, the signal reflects twice, once at the air-medium interface and then at the medium-soil interface. By analyzing the Time of Flight (ToF) of the received signal, and evaluating its velocity, radar instruments retrieve various characteristics of the medium, including altitude, internal structure, and surface type, be it ice, snow, or rock. Radar sounders, for example, can obtain subsurface profiles (radargrams), providing information on the essential climate variables and to understand the processes and structures in the ice [24]. Again, interferometric techniques, like , are efficient for mapping the surface elevation and its temporal change over glaciers and ice sheets [25]–[27]. Also radar altimeter can be used for cryosphere investigation, measuring e.g. the height of the ice surface. It is particularly useful for monitoring changes in glacier volume, sea level rise, and iceberg dynamics [28][29]. To retrieve a 3D structure and a permittivity profile of a snowpack, instead, tomographic SAR data processing is used, e.g. in [30], [31]. Also GPS is used to retrieve SWE, Liquid Water Content (LWC) and snow height [32], [33].
Among different types of radar, Syntetic Apertur Radar (SAR) and Ground Penetrating Radar (GPR) are the most used instruments for both satellite-based and ground-based configurations. A satellite-based SAR is mounted on board of a satellite, and it provides high-resolution images of the Earth's surface, regardless of atmospheric or lighting conditions [34]. This makes SAR an essential tool for monitoring polar regions, enabling observation of changes in glacier cover, glacier dynamics, and ice shelves. SARs are also employed in ground-based configurations [35], called Ground Based SARs (GB-SARs), to monitor glacier movements at a local scale. These systems, often deployed in polar research stations, allow precise measurements of glacier velocities and deformations.

1.3 Novelty and importance of this research

In this thesis, a novel radar system called Snowave has been introduced. Snowave is a ground-based multi-band radar working with the same principle of a GPR, overcoming some of its limitations. Indeed, standard GPR systems, working with one transmitter and one receiver, can compute the ToF of a signal penetrating into a medium. From there, in order to retrieve the distance traveled by the wave, and thus the thickness of the medium, the velocity has to be known. The determination of this velocity relies on the dielectric properties of the medium, creating an ambiguity. Indeed, the system presents one equation and two unknown, posing a problem on the determination of either one of the two. To overcome this problem, standard methods usually assume the velocity based on other observations, or rely on the computation of that one using data acquired with other instruments or sensors. However, these methods impose limitations, as each measurement must be correlated with other observations. Another option is to use complex techniques, e.g. Common Mid-Point (CMP), not easy to apply in the field). Therefore, the use of only two antennas, one to transmit and the other to receive, cannot easily solve this ambiguity by itself. Therefore, Snowave tries to solve this problem by using an additional receiver. By comparing the two ToF arriving from the same transmitter and detected by two receivers, two different propagation paths are found. This allows to have two equations and two unknowns for estimate the thickness of the medium and the velocity of the wave in it. The problem does not have any ambiguity at this stage, and thickness and velocity can be determined. The concept will be explained more exhaustively in Ch. 2, while some applications and real tests will be discussed in Ch. 3 and Ch. 4.

In this work, a part related to the AtG configuration issues has been considered too in Ch. 5. Indeed, a modelization work has been done in order to evaluate the effect of the surface roughness in the backscattered signal from AtG, using satellite data to cross-check the model. Moreover, a first test with an Ultra Wide Band (UWB) radar System on Chip (SoC) for that type of configuration is also presented.

Chapter 2

Snowave radar system and accompanying measurements

In this chapter, a detailed description of the radar instrument employed for cryosphere monitoring is provided. The mechanical setup, including all its components and their respective functions, is presented. Additionally, the physical principle behind it is explained. Furthermore, an overview of the in-situ investigation method is outlined, which integrates radar observations with standard manual analysis techniques.

2.1 System Architecture

Among the radar instruments and techniques used for cryosphere monitoring, Snowave (Fig. 2.1), a radar architecture developed at the University of Pavia, is one of its kind. Snowave is a light, compact and robust multi-static radar architecture operating in different frequency bands. The general scheme is depicted in Fig. 2.2, and it shows three radiators laying on the surface of the material, looking downward[1].

[1]In the past, some theoretical experiments have been carried out with a upward-looking configuration [36][37], but the idea was soon discarded. Although a fixed system might be useful to monitor the complete evolution of a snowpack over a season, it contradicted the original idea of having a portable system to use whenever and wherever required.

Figure 2.1: Snowave logo.

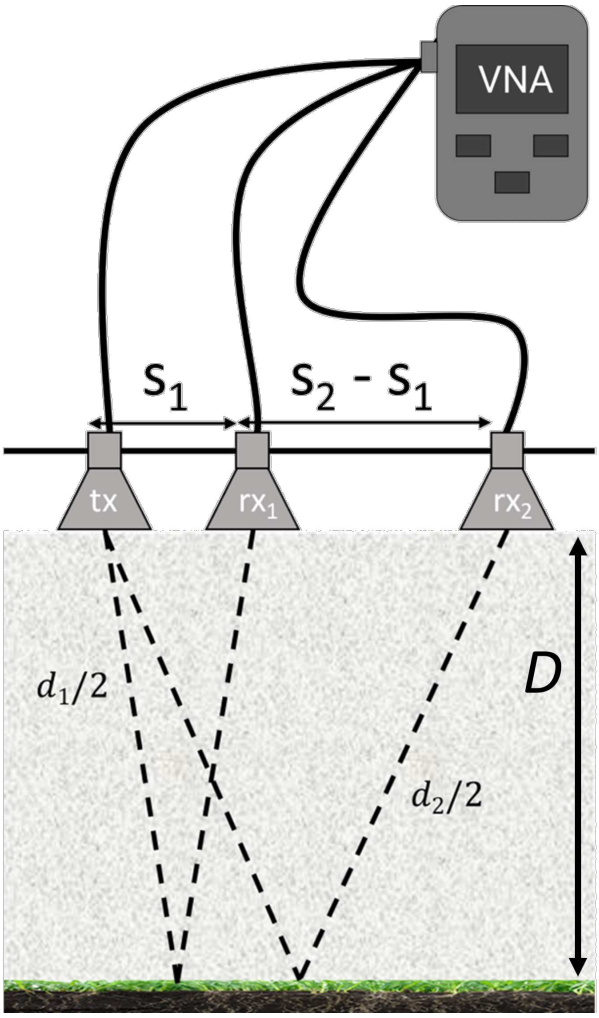

Figure 2.2: Snowave architecture. On the top there's the Vector Network Analyzer (VNA), connected to the radiators through three coaxial cables (usually also a manual switch is used, not represented here). tx is the transmitter, rx_1 and rx_2 are the two receivers. The distances between these radiators are indicate with s_1 and $_2$. D is the depth of the snowpack. d_1 and d_2 are the propagation distances of the EM wave inside the medium.

Figure 2.3: Equipment for the setup, from the left, top: Field Fox VNA; coaxial cable with N-type output; mechanical RF switch up to 12 GHz; some of the RF adapters used to connect the antennas.

The first radiator on the left of the picture, called tx, is emitting a signal which penetrates into the snowpack and travels downward toward the ground. Once reached the soil, the signal scatters, with a portion of its power being reflected back toward the surface. There, it is collected by two different antennas, rx_1 and rx_2, which are positioned at a distance s_1 and s_2 from the transmitter, respectively. The generation of the signal, as well as the recording of the reflected powers, are done by means of a commercial Vector Network Analyzer (VNA) by Keysight FieldFox N9916A, which is connected to the radiators through three coaxial cables and various RF adapters (see Fig. 2.3). In order to match the number of cables and the number of the VNA ports (2, one input and one output), a manual Radio Frequency (RF) switch is used at the receiving end. The magnitude and phase of the reflected signal, recorded by each receiver, is visualized in terms of S_{21} parameter in frequency domain, using the transmitted signal as a reference. By performing a Fourier Transform, the signal goes from frequency to time domain and it becomes possible and easy to analyze the signal's time-of-flight as it penetrates the medium.
In general, by looking at the radar traces in time domain, the target generates a peak at the moment corresponding to its distance from the receiver. For example, when a target is 1 m away in the air, the peak in the time domain radar trace is located at 6.66 ns (3.33 ns to reach the target plus 3.33 ns to return at the receiver after the reflection), considering that the velocity of the signal equals the speed of light, i.e. $c = 3 \cdot 10^8$ m/s. The computation of the distance of the target is trivial and unambiguous.

Instead, in case the propagation occurs within a medium, different from air, its EM properties need to be taken into account. The parameters to be considered are the complex dielectric constant ε and the complex magnetic constant μ, which are represented in Eq. 2.1:

$$\varepsilon = \varepsilon_0(\varepsilon' - j\varepsilon'') \qquad \mu = \mu_0(\mu' - j\mu'') \tag{2.1}$$

In these equations, ε_0 and μ_0 are constant values, equals $8.85 \cdot 10^{-12}$ F/m and $4\pi \cdot 10^{-7}$ H/m, respectively. ε', ε'', μ' and μ'' are real adimensional quantities and they determine how an EM wave propagates within a material.
The complex dielectric constant ε is a quantity that takes into account both the dielectric losses and the capacitive properties of a material and it is composed by a real and an imaginary part:

- the real part (ε') indicates the material's ability to store electrical energy when subjected to an electric field.
- The imaginary part (ε'') indicates the dielectric losses of the material, i.e., the electrical energy that is dissipated under the influence of the electric field. A higher value of ε'' indicates greater dielectric losses in the material.

The complex dielectric constant is often expressed as a function of the frequency of the applied electric field and can vary with it.
The complex magnetic constant μ, is a property of materials that takes into account both magnetic permeability (μ') and magnetic loss (μ''). Magnetic permeability measures a material's ability to respond to an applied magnetic field, while magnetic loss represents the energy dissipated under the influence of a time-varying magnetic field. Specifically, snow and ice are characterized by a low magnetic susceptibility, resulting in a weak response to magnetic fields, making the effect of μ' and μ'' negligible. Therefore, the second equation in 2.1 can be approximated as in the vacuum. Moreover, in the microwave frequency range, dry snow and ice are lossless medium, and therefore the complex dielectric constant can be expressed with only the real part. The new expressions are written in Eq. 2.2.

$$\varepsilon = \varepsilon_0\varepsilon' = \varepsilon_0\varepsilon_r \qquad \mu = \mu_0 \tag{2.2}$$

Using these approximations, the velocity of the EM wave propagating into snow or ice can be computed as:

$$v \approx c/\sqrt{\varepsilon'} \tag{2.3}$$

This formula shows that the EM signal is moving at a slower pace within the medium with respect to the propagation in air. It is worth noting that this approximation is true for lossless medium, such as dry snow and ice, but it can be used also for low-losses material, like wet snow, where the imaginary part of the dielectric constant is much lower than the real part ($\varepsilon'' \ll \varepsilon'$).
In the radar trace, the peak is shifted in time with respect to the position in

air, indicating that the signal is moving slower. Thus, determine the position of the target in this case creates ambiguity, since both the distance and the velocity (and therefore the dielectric constant) are unknown. A second receiver in a different position in a radar system like Snowave can solve this ambiguity as follows. First of all, the time at which the target generates a reflected peak can be found for both the receivers with these equations (Eq. 2.4):

$$\begin{aligned} T_1 &= d_1/v \\ T_2 &= d_2/v \end{aligned} \tag{2.4}$$

where d_1 and d_2 are the oblique propagation distances following the two paths of the signal, related to the ToF visible from the radar traces. The velocity v is the same for both the propagation paths under the condition of an homogeneous medium. This may be not always true, since the snowpack may have a very high variability. Nevertheless, in most of the cases it is sufficient to have a bulky indication of the snowpack/glacier parameter. Additionally, the proximity between the measurement paths is often minimal, thereby minimizing the presence of inhomogeneities within the medium.
Introducing the distances between the transmitter and the first receiver rx_1 and the transmitter and the second receiver rx_2, s_1 and s_2 respectively, the depth of the medium D (see Fig. 2.2 for the notation) from the radar to a flat target (like the soil) can be calculated using the Pythagorean theorem:

$$\begin{aligned} d_1^2 &= (2D)^2 + s_1^2 \\ d_2^2 &= (2D)^2 + s_2^2 \end{aligned} \tag{2.5}$$

Combining Eq. 2.4 and Eq. 2.5, the ToF of the two signals can be computed, as in Eq. 2.6:

$$\begin{aligned} T_1 &= \frac{\sqrt{(2D)^2 + s_1^2}}{v} \\ T_2 &= \frac{\sqrt{(2D)^2 + s_2^2}}{v} \end{aligned} \tag{2.6}$$

From the last two equations, the only unknown values are D and v. After algebraic manipulation, and including Eq. 2.3, the so called Snowave equations can be found (Eq. 2.7 and Eq. 2.8):

$$D^2 = \frac{s_2^2 T_1^2 - s_1^2 T_2^2}{4(T_2^2 - T_1^2)} \tag{2.7}$$

$$\varepsilon' = c^2 \cdot \frac{(T_1 - T_2)(T_1 + T_2)}{(s_1 - s_2)(s_1 + s_2)} \tag{2.8}$$

The target is now precisely localized through the value of D and the medium can be characterized with its dielectric constant ε'. It will be shown that for cryospheric monitoring it is crucial to understand the dielectric constant of the natural body, in order to discriminate different types of snow or ice.

2.2 Components

Depending on the type of snow or ice, signal at different frequencies works differently. Depending on the wavelength, the penetration depth, i.e. the measure of how deep the electromagnetic radiation can penetrate into the material, can vary a lot, and especially when the attenuation from the water comes to play. That's why for different types of investigation, different bands and thus antennas are used. Very low frequencies are commonly employed for probing deep targets, such as the bedrock of a glacier. Due to their long wavelengths, imperfections or disturbances (such as air bubbles, rocks, and other objects) do not significantly impact the measurements, as they are too small to be detected. In some cases, it is possible also to detect the interface between the snow accumulated as firn and the beginning of the pure ice of the glacier. Frequencies around few GHz are used for deep dry snowpacks or slightly to moderated wet snowpacks, thanks to the relatively long wavelength and the robustness of the signal against the attenuation. Going up in frequency, the signal becomes more and more intolerant to the presence of water. Those bands are used in dry condition to investigate the history and the future of dry snowpacks looking at the layering.

Fig. 2.4 illustrates different types of antenna corresponding to different frequency bands used during the Snowave campaigns. The radiators in the first row (a - d) are employed for snow monitoring. The first one (Fig. 2.4a) is a L-band WR650 radiator operating between 1.15 and 1.72 GHz. Given its lower frequency, this antenna's dimensions are relatively large, with an aperture of 165.1 mm x 82.55 mm. Fig. 2.4b shows the transition WR340 in S-band, spanning from 2.2

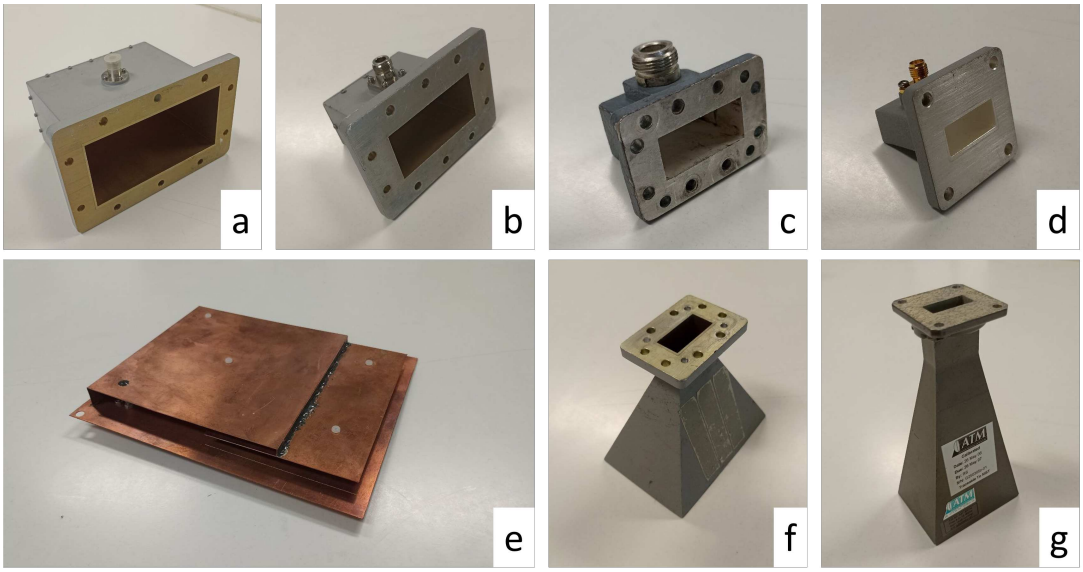

Figure 2.4: Type of radiators used in Snowave: (a) L band coaxial truncated waveguide; (b) S band coaxial truncated waveguide; (c) C band coaxial truncated waveguide; (d) X band coaxial truncated waveguide; (e) custom-made UHF PIFA antenna; (f) horn antenna in C band; (e) horn antenna in X band.

Table 2.1: Frequency bands used in the Snowave system.

Frequency	**Wavelength**	**Antenna**	**Type of monitoring**
UHF (300 MHz)	1 m	PIFA	Glacier and firn
L (1 - 2 GHz)	15 - 30 cm	WR650	Dry to moderately wet snowpack
S (2 - 3.5 GHz)	8.6 - 15 cm	WR340	Dry to slightly wet snowpack
C (5.5 - 8 GHz)	3.7 - 5.5 cm	WR137	Dry snowpack
X (8 - 12 GHz)	2.5 - 3.7 cm	WR90	Dry snowpack, very sensitive to every interface

GHz to 3.3 GHz, with dimensions of 86.36 mm x 43.18 mm. The C-band WR137 works from 5.85 GHz to 8.20 GHz and has a dimension of 34.8488 mm x 15.7988 mm (Fig. 2.4c). The last one in Fig. 2.4d is a WR90 and it is the smallest one (22.86 mm x 10.16 mm) used in Snowave. In this case, the working frequency goes from 8.20 GHz to 12.40 GHz (X-band). These antennas present resolutions in the order of centimeters or tens of centimeters, depending on the type of snow (dry or wet, with ε' between 1.2 and 2.8) and on the bandwidth used during the measurements:

$$\zeta = v/2B \tag{2.9}$$

The antennas show a minimum gain (around 4 to 7 dB) and directivity but, in order to steer the EM wave toward the ground, horn antennas are connected sometimes: Fig. 2.4f is the horn antenna for the WR137, while Fig. 2.4g is the horn antenna for the WR90. It is worth noting that using horns is not always advantageous, especially in cases of thin snowpacks. In such situation, the electromagnetic wave must travel along a path that is highly oblique to the perpendicular of the aperture plane, which may not yield significant benefits.

Fig. 2.4e shows a custom antenna working in Ultra High Frequency (UHF) range (central frequency at 300 MHz) specifically utilized for glacier monitoring [38]. Since the wavelength at that frequency is very long ($\lambda = 1$ m), an antenna with a standard design would have been huge. Therefore, instead of using commercial aperture antennas as for snow monitoring, a more particular design has been analyzed and realized [39]–[42]. As seen from the picture, the design is similar to a patch antenna in a Planar Inverted-F Antenna (PIFA) configuration which decreases the dimension down to $\lambda/4$ (from 1 m to 25 cm). In addition, a folded capacitive load has been incorporated at the termination of the "F"

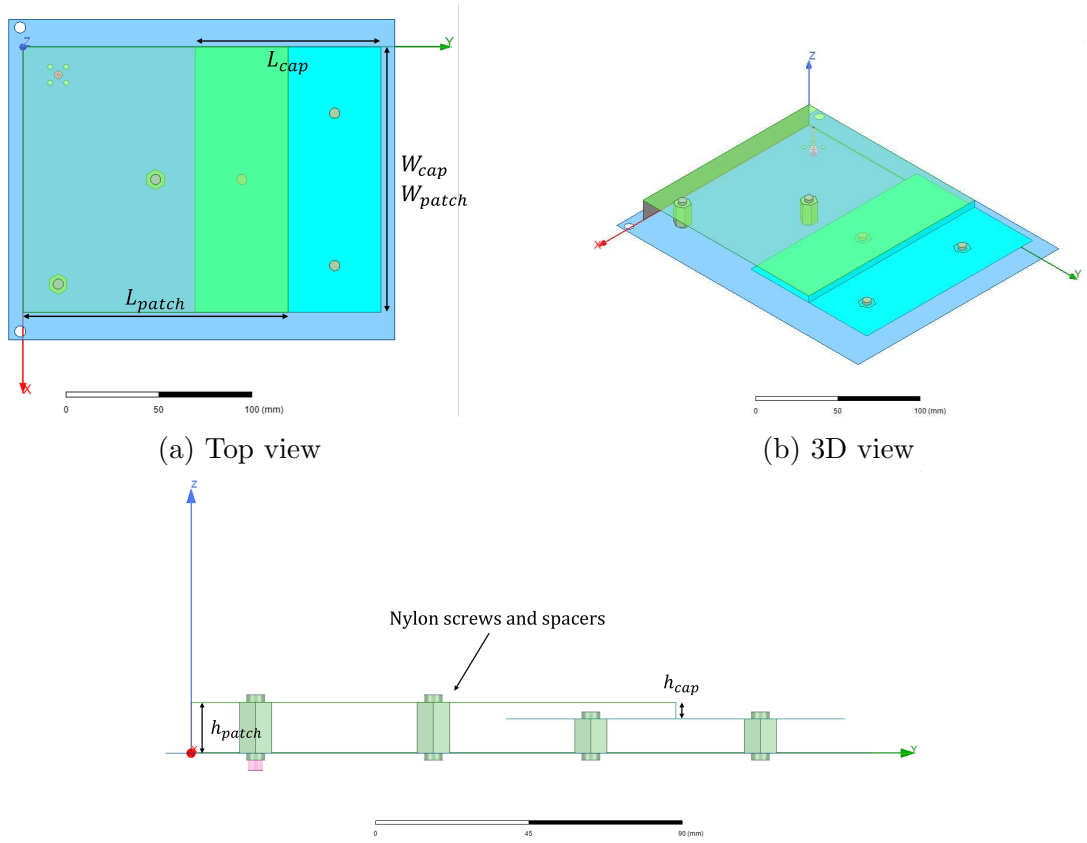

(a) Top view

(b) 3D view

(c) Side view

Figure 2.5: Final design of the capacitive loaded PIFA antenna. Dimensions: $L_{patch} = W_{patch} = W_{cap} = 14.29cm$; $L_{cap} = 10cm$; $h_{patch} = 1.5cm$; $h_{cap} = 0.5cm$.

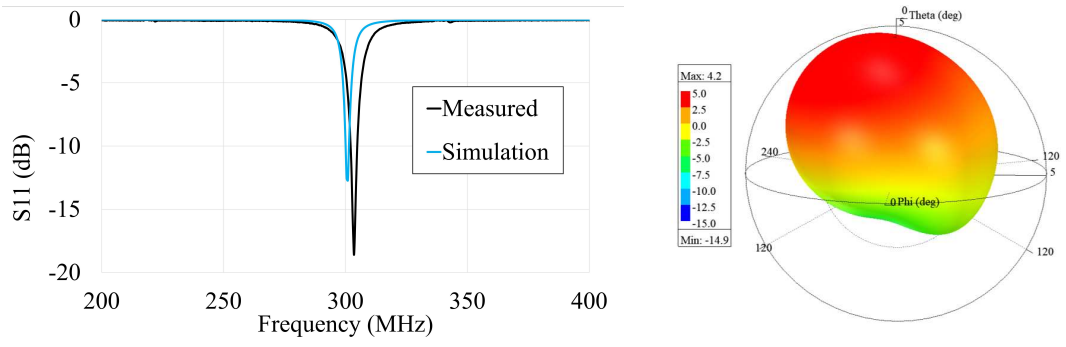

(a)

(b)

Figure 2.6: Characteristics of the antennas: (a) S_{11} parameter, comparison between simulated and measured antenna; (b) Simulated gain of the antenna.

element. This adaptation has further contributed to the size reduction, resulting in dimensions slightly above $\lambda/8$. Fig. 2.5 illustrates the design of the antenna, while the final dimensions are written in its description. For the fabrication, a metal sheet of a copper alloy Cu-DHP R290 with a thickness of 0.5 mm has been used. For the capacitive load, the open end of the radiating patch has been folded towards the ground plane, establishing a connection with a plate positioned parallel to the ground (like a parallel-plate capacitor). To maintain a consistent and uniform distance between the capacitor plate and the ground plane, nylon screws and spacers were employed[2]. These nylon components had no considerable impact on the electromagnetic response of the system, even proved by the simulations. All the conjunctions were metalized and glued together with a conductive paste and standard epoxy adhesive.
After the fabrication, the antenna has been measured and compared with the result of the simulation, done with a commercial full-wave solver, Ansys high frequency simulation software (Ansys HFSS). Only the frequency matching in terms of S_{11} parameter has been directly measured due to the frequency. Indeed, such low frequency falls below the range covered by the available anechoic chamber, and reaching the far field was not possible with that facility[3]. In Fig. 2.6a, the measured S_{11} reached a value of -18 dB, which is indicative of a positive frequency matching. A frequency shift occurs due to minor inaccuracies in the fabrication process. However, since the antenna needs to communicate with two other identical radiators exhibiting the same S_{11} curve, this frequency shift is negligible. Figure 2.6b depicts the gain of the structure, which exhibits high isotropy and reaches a maximum value of 4.2 dB, consistent with the commercial aperture antennas discussed earlier.

For glacier monitoring, the directivity of this antenna could be not sufficient to reach the very deep bedrock or to detect the reflected echo. Therefore, two equivalent USB-powered amplifiers were used during the field campaigns and

[2]Nylon screw and spacers were not the only idea. During the first fabrication, the plate of the capacitor was supported by a layer of foam (ROHACELL 71HF) with very low density and extremely low dielectric constant, similar to air. The robustness of the structure and its accuracy was not guaranteed, therefore it has become necessary find another solution.

[3]At 300 MHz, the far field is at a distance greater than 10 m.

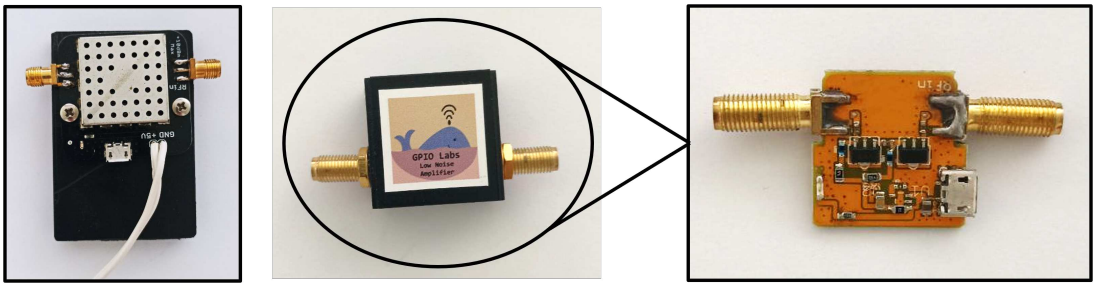

Figure 2.7: The two amplifiers used during glacier monitoring campaigns. The first on the left is referred as "Black", while the second one is "Whale". On the right, the circuit inside the box of the Whale amplifier is depicted.

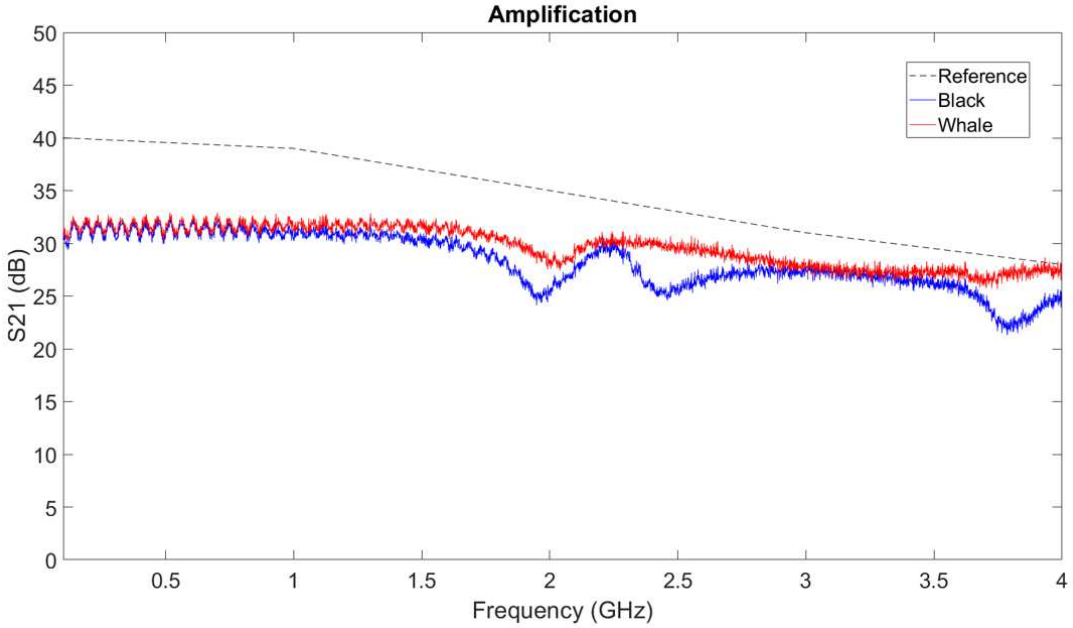

Figure 2.8: Comparison between the amplification from the datasheet (black dashed line) and the measured amplification for both the Black and Whale amplifiers.

they are shown in Fig. 2.7. Both of them are Low Noise Amplifiers (LNAs) from *GPIO Labs* working from 100 MHz to 8 GHz. The maximum nominal gain is 40 dB, with a noise figure at 2 GHz of 2.9 dB. Actually, the connectors (SMA type), usually very delicate, didn't have the minimum mechanical robustness to resist during the screw/unscrew process during the measurements on the field. Indeed, while carrying out both indoor and outdoor tests, it happens that the connectors broke. Every time it happened, it was possible to fix it, but the performances afterward were not optimal. The amplification reached after this process and used during the monitoring campaigns is shown in Fig. 2.8.

2.3 Calibration

Before each set of measurements, several preparatory steps are necessary to ensure the accuracy of the tests. The first thing to do is to check each component and each connection, in order to avoid the problem of loose connectors or bent or damaged cables. Then, the calibration of the equipment (in this case, the VNA) is essential to eliminate the potential influence of the components (cables, connectors, switch and more) on the measurement results. Typical calibration methods are the Short, Open, Load, Through Calibration (SOLT) calibration (Short, Open, Load, Through) or the Through Reflect Line (TRL) (Through Reflect Line), but other are often used. Since the calibration in the test field

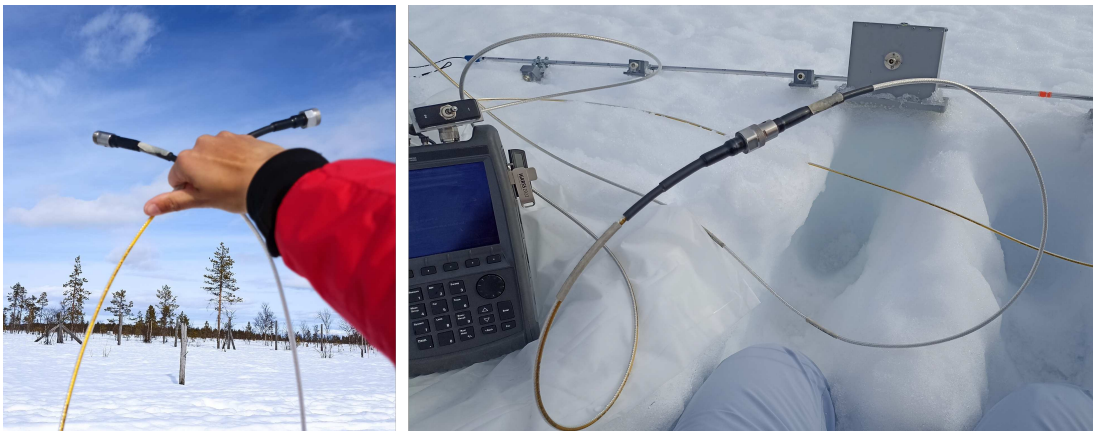

Figure 2.9: Two step of calibration when the antennas are not connected.

doesn't need to be extremely precise[4] and the harsh environment not always permits to be accurate during the tests, no calibration kit is normally used. The calibration process involves providing the VNA with two reference measurements. The first one can be approximated to an open circuit and it is carried out by orienting the two terminals in opposite directions, typically facing the sky. The second reference measurement involves a through measurement. Depending on the equipment used each time, this is achieved by either screwing the terminating connectors or directly joining the antennas face-to-face.

The calibration has been done in two different way during the test which will be described in the next chapters. When feasible, it was carried out utilizing the aperture of the antenna as the calibration plane. This implies that the cables, connectors, and antennas were all connected during calibration. Consequently, the received signal, once transformed into the time domain, exhibits the peak of the target at the precise distance. In cases where this approach wasn't applicable[5], calibration was performed with the adapters and antennas disconnected (see Fig. 2.9). In such instances, the cable ends were taken as the calibration plane. During measurements, the signal path through the antennas and other components creates a delay in the time-domain trace and it needs to be quantified.

Therefore, measurements in a controlled environment such as the anechoic chamber have been carried out. By measuring the ToF at known distances, it is possible to calculate the delay experienced by the signal inside the antennas and the adapters all the way to the cables. This experiment has been carried out for those antennas able to create a significant error compared to the distance to be measured. In the graphs in Fig. 2.10 are shown the delays introduced by the antennas in L-, S- and C- band for different distances from target. The blue and red curves indicate that the two antennas are positioned at two different distances on the baseline, 30 cm and 70 cm respectively. The black dotted

[4]Other natural and geographical factors will create inaccuracies on the measure, which will hide the inaccuracy of the calibration. It will be better explained in the next chapter.

[5]Due to not-connectable antennas (es. PIFA) or to software problems of the device.

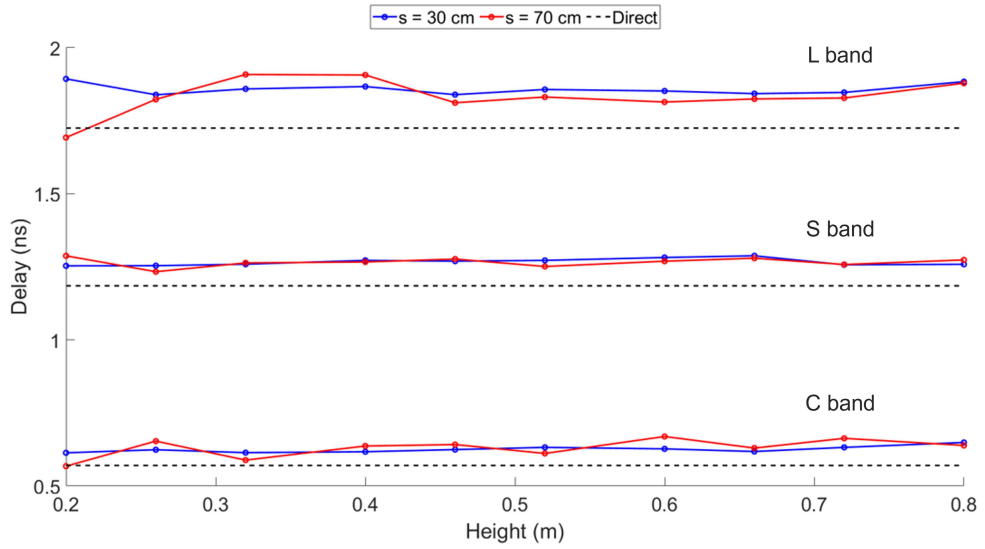

Figure 2.10: Delay in the measurements due to the path of the signal into the antennas.

line is instead the delay introduced when the antennas were directly connected (aperture-to-aperture). It is logic that, for lower frequency, and therefore for bigger antennas, the delay is greater. Although the disparity between the values for varying distances is slight, it remains non-negligible. This will be taken into account in the analysis of the radar traces exposed in the next chapters.

2.4 Manual Analysis

During the field campaigns, several radar data are collected. Such data, resulting in values of depth, density and water content after the proper analysis, have to be compared with accurate data taken in the measurement site. The conventional and widely adopted approach for investigating these parameters is manual analysis. Indeed, it returns a complete spectrum of parameters useful to understand the snow conditions, to evaluate the evolution of water resources, and assessing the implications of climate change. The manual analysis follows the guidelines of the International Hydrological Programme (IHP) of the United Nations Educational, Scientific and Cultural Organization (UNESCO)[43]. In Italy, the primary organization for investigating snowy environments and producing avalanche bulletins is the Interregional association for coordination and documentation of snow and avalanche problems (AINEVA). This organization collaborates with regional agencies, e.g. the Agenzia Regionale per la Protezione Ambientale - Regional Agency for Environmental Protection (ARPA), to cover the entire Italian Alps region and part of the Apennines. Operators conduct observations of snow coverage conditions on selected, representative, and safe sites. This involves digging snow pits and visually assessing the snow's characteristics. A thorough observation typically takes around 2 to 3 hours, during which opera-

Table 2.2: Characteristics of snow on the ground [43].

Description	**Units**	**Symbol**
Grain shape	- -	F
Grain dimensions	mm	E
Density	kg/m^3	ρ_s
Hardness	N	R
Liquid Water Content	%	θ_w, LWC
Snowpack temperature	°C	T$_s$
Height	cm	L

tors are exposed to cold and occasionally harsh environmental conditions for an extended duration.

These surveys are consistently carried out in the same geographical area, under similar exposures, and at a consistent altitude. The tests are challenging to replicate exactly in the same location or within a short timeframe due to the inherent non-repeatability of the test. In Tab. 2.2 are reported the main factors which can be found by means of the manual analysis, using the equipment shown in Fig. 2.11.
After finding an adequate spot, excavating the pit and identifying the layers using visual interpretation, hands (with gloves) or a brush, the next step involves examining the snow grains. The type and size of grains are determined using a crystallographic board and a magnifying lens, with at least 8x magnification. It's important to note that grain size determined through standard field techniques may not represent the electromagnetic properties of snow with accuracy. To address this limitation, the concept of an Optical-equivalent Grain Size (OGS) is introduced [44]. OGS is linked to the specific surface area and microstructure of the snow, providing a more comprehensive representation. This approach is particularly valuable for remote sensing applications and can be estimated based on factors like dendrite branch width, thickness of thin plates or dendrites, needle diameter, or hollow crystal shell thickness [45][46] (see also Chapter 3).
The snow density ρ_s is expressed as the mass of a snow sample contained in a sampler with known volume (kg/m^3). The standard sampler is a metallic tube with 20 cm of length and 5 cm of diameter, but wedge samplers can also be employed. To weight the sampler, can be used either a traditional digital scale or a spring scale. This measure can be directly compared with the results of the radar investigation [47][48].

Figure 2.11: Standard equipment for manual analysis.

Hardness measures the snow's ability to resist the penetration of an object. The measurement is strongly operator-dependent, therefore an accurate measure is difficult to achieve. One instrument that can be used is the penetrometric probe, i.e a metallic probe with a sharp tip at the end and a weight on the top. The weight hits the probe and penetrate into the snowpack. Depending on the force applied and how much the probe penetrate, the hardness profile (measured in N) is computed [49]. Another method is the hand test introduced in 1950 in [50]. This method involves using various degrees of penetration, such as fist, four fingers, single finger, pencil, and knife, each associated with specific force ranges (respectively 20 N, 100 N, 250 N, 500 N, 1000 N, on average). For each layer within the snowpack, the hardness value is determined by identifying the object that can gently penetrate the snow with minimal force. It's worth noting that this test is subjective and depends on the individual's perception and judgment. The LWC refers to the amount of water present in the snow in its liquid state, which can derive from melting, rain or a combination of both. In the field, several type of measurements can be done: cold (freezing) or alcohol calorimetry, hot (melting) calorimetry[6] [51], the dilution method [52], and dielectric measure-

[6]It necessitates a well-designed apparatus and careful observation to achieve precise measurements.

ments [53]. This approach will be further explained in the upcoming chapters, as well as other parameters crucial for a comprehensive snowpack analysis.
The result of this survey is usually displayed using official models proposed by AINEVA, reporting snowpack information, the outcomes of other stability tests and even weather conditions.

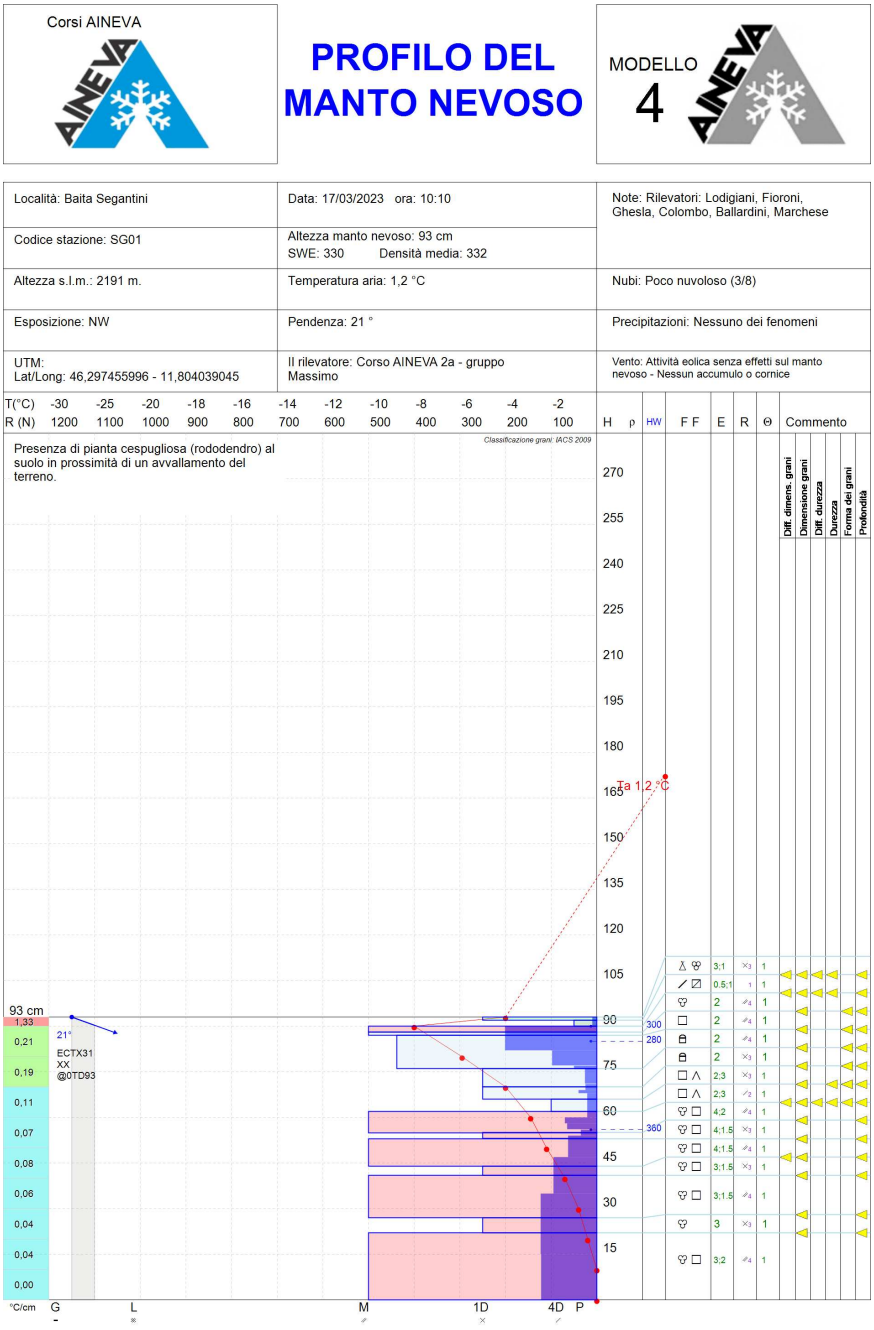

Figure 2.12: Example of an AINEVA module 4 for the snowpack condition observation. Courtesy: AINEVA - Trento - Italy.

Chapter 3

Snow monitoring

In this chapter, a real-world application is introduced. Starting from the formation of the snow and its metamorphism, different types of snow are described, showing different EM behaviors. For both dry and wet snow, the campaigns carried out with Snowave are presented. For wet snow, different type of features will be investigated in the different campaigns.

3.1 Snow formation and metamorphisms

Snow is a solid crystalline form of water, with a molecular structure organized in an hexagonal geometry. These crystals are generated in the atmosphere, and more in particular inside the clouds, at different altitudes, temperatures and humidity supersaturation conditions [54]. In theory, the water droplets in the cloud should freeze as soon as they go below 0°C. Actually, it can be possible to have the so called *super-cooled status*[1] in pure-air condition, i.e. without the contamination of foreign particles in the air mass, where the droplets can remain liquid even down to -40°C. This is a very unstable condition, and even the smallest perturbation can make the droplets freeze instantaneously. However, usually the mass of air contains impurities, such as salts, chalk, sulfates and silicates, which act as catalysts and attract the water molecules, making the solidification process possible already at -9°C. The water molecules arrange themselves around the ice nucleus following an hexagonal geometry and grow along the axis based on the value of temperature and humidity [55]–[59], as reported in the illustration in Fig. 3.2.
In the atmosphere, several shapes of crystals can be produced, based on the temperature and the saturation level. These are called Precipitation Particle (PP),

[1]Super-cooling refers to a substance being cooled below its freezing point while maintaining a liquid or gaseous state, bypassing the usual transition to a solid. This state occurs under specific conditions, like the absence of nucleation sites or disturbances that trigger solid formation. Liquids can exist in this unstable state below their freezing points and only freeze when externally prompted, such as by a seed crystal or agitation. For instance, super-cooled water can remain liquid below 0°C until disturbed or encountering a nucleation site, leading to rapid freezing.

identifiable with the symbol +. In table 3.1, the different shapes formed in the cloud are described. In the second column, there are the codes of those crystals according to the International Classification of Seasonal Snow on the Ground [43]. The pictures in Fig. 3.3 depict different precipitation particles in a magnified view. It is important to notice that some shapes are similar but they can be discriminate using other properties, such as the color (transparent or opaque) and the dimension.

After the precipitation event, the layers of snow accumulate on top of each other to form a snowpack. The snowpack is a complex structure in continuous evolution, and it is a mix of:

- solid water, like amorphous ice and crystalline structures;
- liquid water, but only when the snow is wet, and the droplets lay in the ice pores;
- water vapor in the ice pores;
- air;

These substances are in a metastable equilibrium[2] and act to change the characteristics of the entire snowpack with time. This evolution is ruled by several factors, such as the application of a load or the thermal processes. When a load is applied, e.g. due to a new precipitation, an human, or an animal, it exerts weight on the layers underlying, causing a reduction of the thickness and of the

[2]metastable equilibrium refers to an unstable equilibrium state in which a system can persist for a certain period of time before transitioning to a new, more stable energy state.

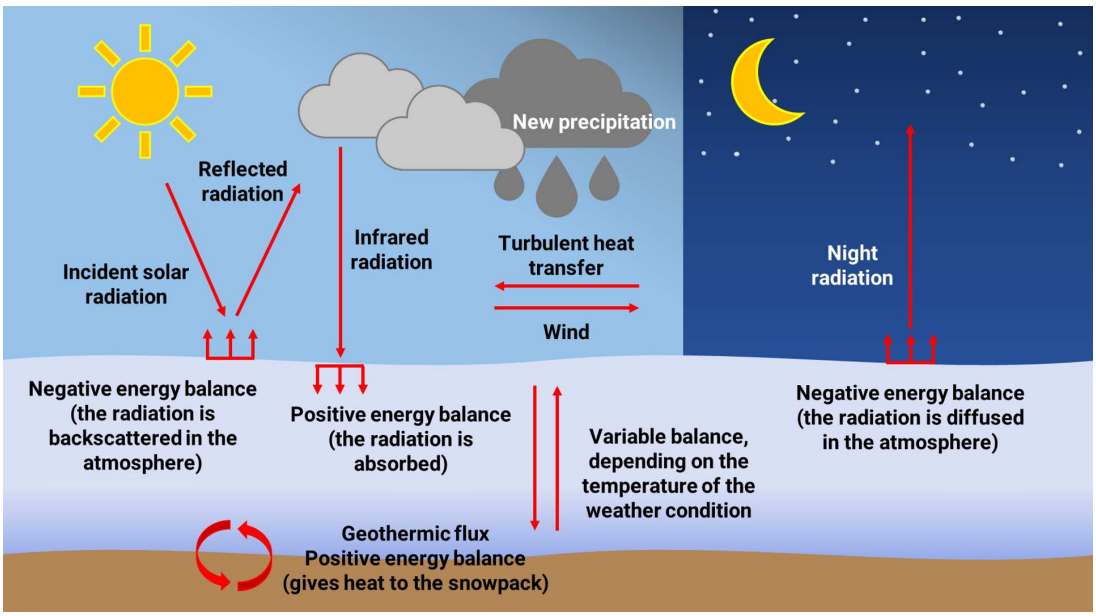

Figure 3.1: Factors influencing the snowpack - energy balance

Table 3.1: Precipitation particles class.

SUBCLASSES	CODE	DESCRIPTION
Columns	PPco ▭	Prismatic crystal, solid or hollow.
Needles	PPnd ⎯	Needle-like, approximately cylindrical.
Plates	PPpl ⊙	Plate-like, mostly hexagonal.
Stellars, dendrites	PPsd ✳	Six-fold star-like, planar or spatial.
Irregular crystals	PPir ◠	Clusters of very small crystals.
Graupel	PPgp ⛆	Heavily rimed particles, spherical, conical, hexagonal or irregular in shape.
Hail	PPhl ▲	Laminar internal structure, translucent or milky glazed surface.
Ice pellets	PPip △	Transparent, mostly small spheroids.
Rime	PPrm ∀	Irregular deposits or longer cones and needles pointing into the wind.

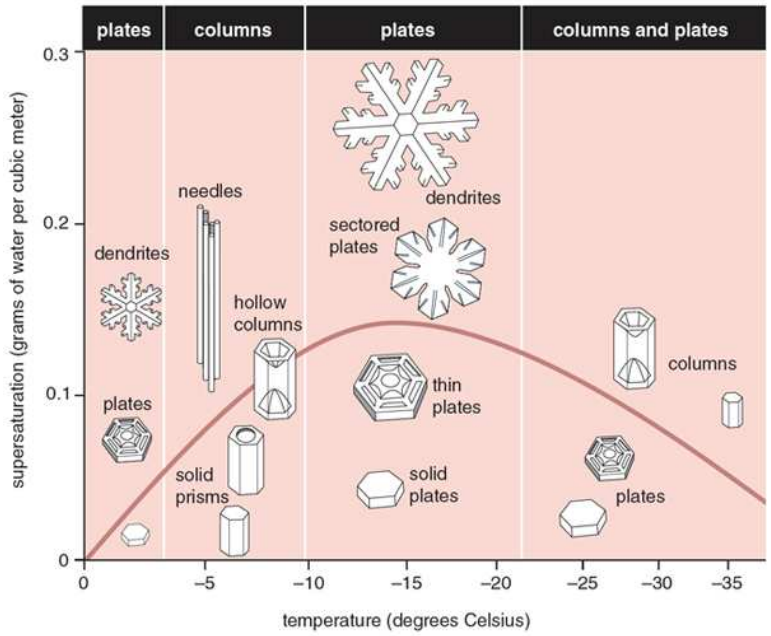

Figure 3.2: Structure of snow crystals, depending on the value temperature and supersaturation.

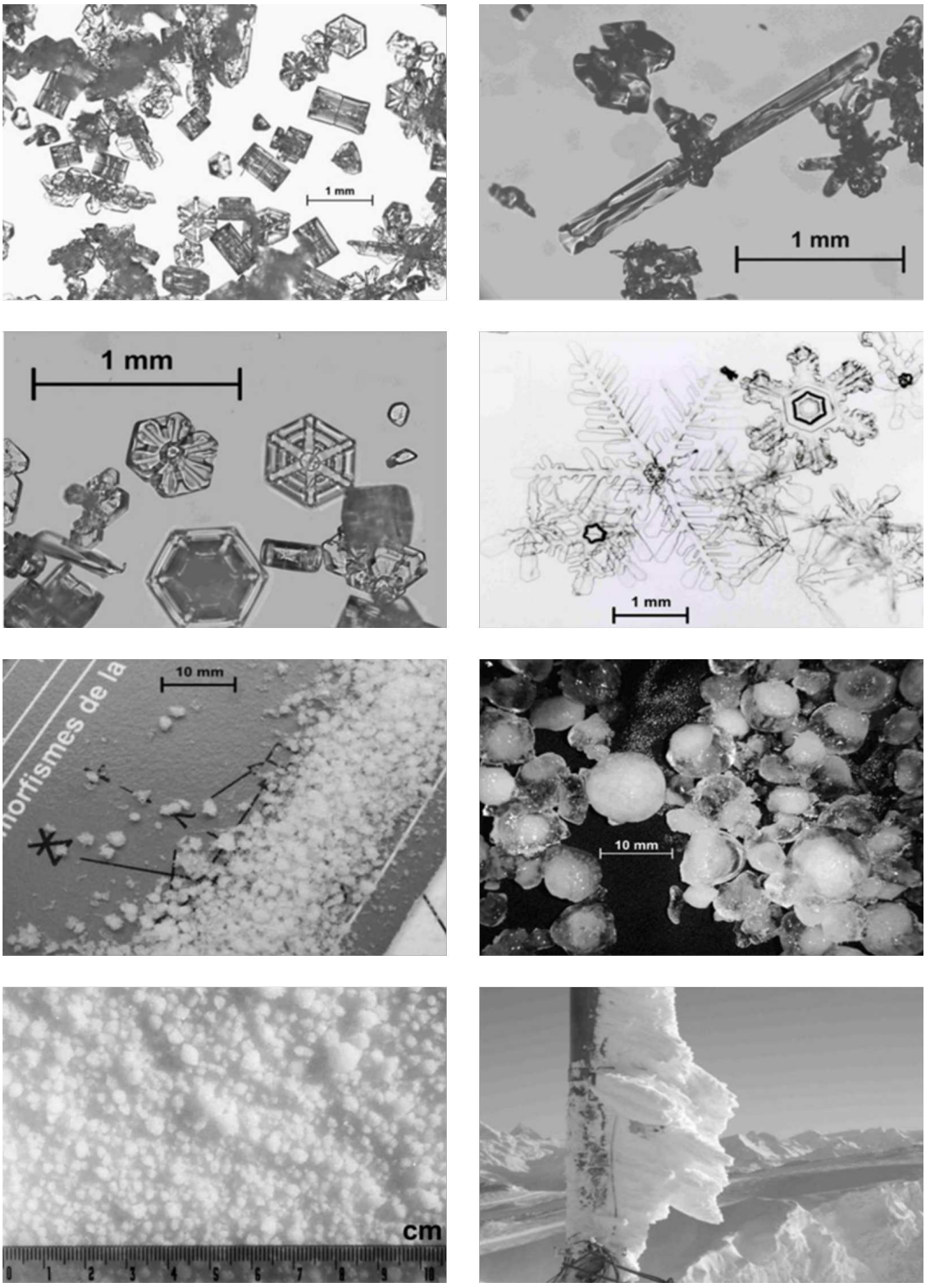

Figure 3.3: Precipitation Particles, from the top left: PPco, PPnd, PPpl, PPsd, PPgp, PPhl, PPip and PPrm. Credits: Kelly Elder, USDA Forest Service, Rocky Mountain Research Station, USA; Carles Garcia Selles, Predicció d'Allaus - Unitat de Riscos Geològics, Institut Geològic de Catalunya, Spain; JSSI–The Japanese Society of Snow and Ice, Japan; Jürg Schweizer, WSL Institute for Snow and Avalanche Research SLF, Switzerland.

quantity of air in the pores. The heat exchanges between the snowpack, soil, and atmosphere are highly significant, as visible in Fig. 3.1. The 90% of the solar radiation (short-wave in the visible and ultraviolet frequency range) impinging on the surface is reflected back in the atmosphere. In clear sky condition, most of the reflected power goes through the atmosphere toward the free space. In this case, only the surface receives heat and increases its temperature, while the rest of the snowpack remain at the same temperature. Instead, when it is cloudy, the reflected radiation enters in the cloud and, due to the interaction with other particles, it is scattered back again toward the Earth. While in the cloud, it changes its frequency, becoming a long-wave radiation in the infrared frequency range, and it is able to penetrate into the entire snowpack and warm it up.
In addition to having a mechanical force, the rain can fall on the snowpack and warm it up. The liquid water freezes when in touch with the frozen grain of the snowpack. This solidification releases latent heat, which is absorbed by the snowpack, increasing its temperature.
Even if it is not its principal effect, the wind can warm up (e.g. with the Föhn) or cool down the snowpack through turbulent processes. The thermal effects are very fast and important with respect to other factors.
The snowpack receives heat also from the soil through the geothermal flux, which goes through the snowpack and is transmitted to the atmosphere. During night time and in clear sky condition, the energy balance is negative and the temperature of the snowpack decreases. This flux is the reason why the soil is always at 0°C, if not frozen or covered by a permafrost layer.
The distribution of the temperatures in the vertical profile is due to the thermal exchange within the snowpack and in relation with the atmosphere and the ground. Within the snowpack, this occurs through thermal conduction of the ice and liquid phases, as well as through the exchange of latent heat during processes of evaporation and sublimation.
This change in temperature produces a metamorphism in the snowpack during time [60]–[63]. It is important to introduce the temperature gradient, defined as the difference in temperature between two points at different depth, expressed in °C/m or °C/cm (see Fig. 3.4):

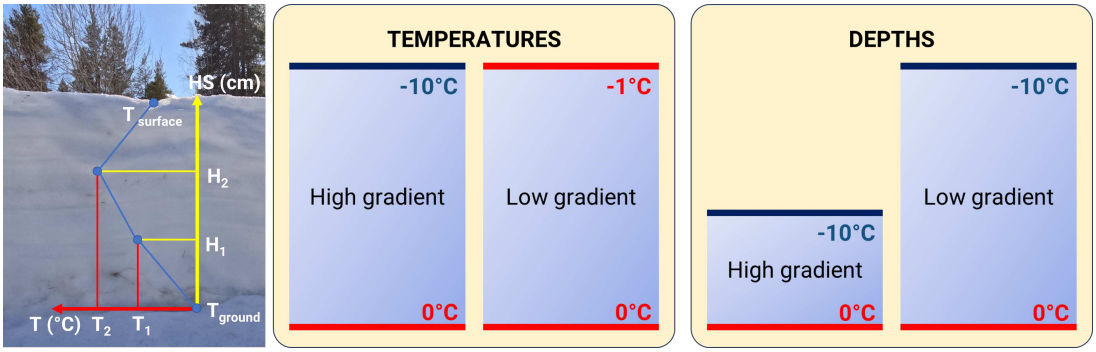

Figure 3.4: Visual explanation of the temperature gradient and effect of the temperature and of the height on the behavior of GT.

$$GT = \frac{T_2 - T_1}{H_2 - H_1} \tag{3.1}$$

This value not only depends on the temperature, but also on the depth of the snowpack. In general, there exists three different types of gradient:

- Low gradient: small temperature variation up to 0.05°C/cm, destructive metamorphism:
- Medium gradient: temperature variation ranging from 0.05 to 0.2°C/cm, slow or slight kinetic growth of crystals during destructive metamorphism;
- High gradient: temperature variation exceeding 0.2°C/cm, constructive metamorphism with strong kinetic growth of crystals.

Moreover, there exists an isotherm condition, where the gradient is close to 0°C/cm. This means that the entire snowpack has the same temperature, which has to be equal to 0°C. This condition brings to the melting of the snowpack, and usually occur in spring or during long warm periods.

Low gradient metamorphism

The temperature difference within the snowpack is relatively small. The vapor tension on the surface of the snow crystal, which is the pressure exerted by the vapor phase of water when it reaches equilibrium with its solid ice phase at a specific temperature, is not uniform. This lack of uniformity is due to the crystal's geometry, specifically the presence of concave and convex areas. When sublimation begins, molecules migrate from the sharp areas to the concave areas to stabilize an energetic equilibrium. This process simplifies the crystal's shape, causing it to become more rounded, and reducing its diameter (Fig. 3.5).

In the first steps, the snowpack is unstable. Once granular snow is formed, contact zones (known as necks) are created within the pores between the grains[3] through the process of deposition/sintering, which involves the fusion or welding

[3]The term "snow crystal" refers to an individual ice crystal with a specific symmetrical hexagonal shape and intricate patterns, while "snow grain" refers to small irregular fragments or particles of compacted snow or ice without distinct symmetrical characteristics.

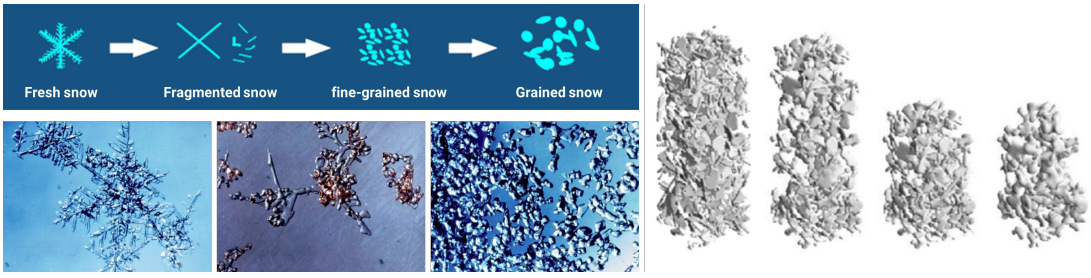

Figure 3.5: Low gradient metamorphism. Courtesy: AINEVA - Trento - Italy.

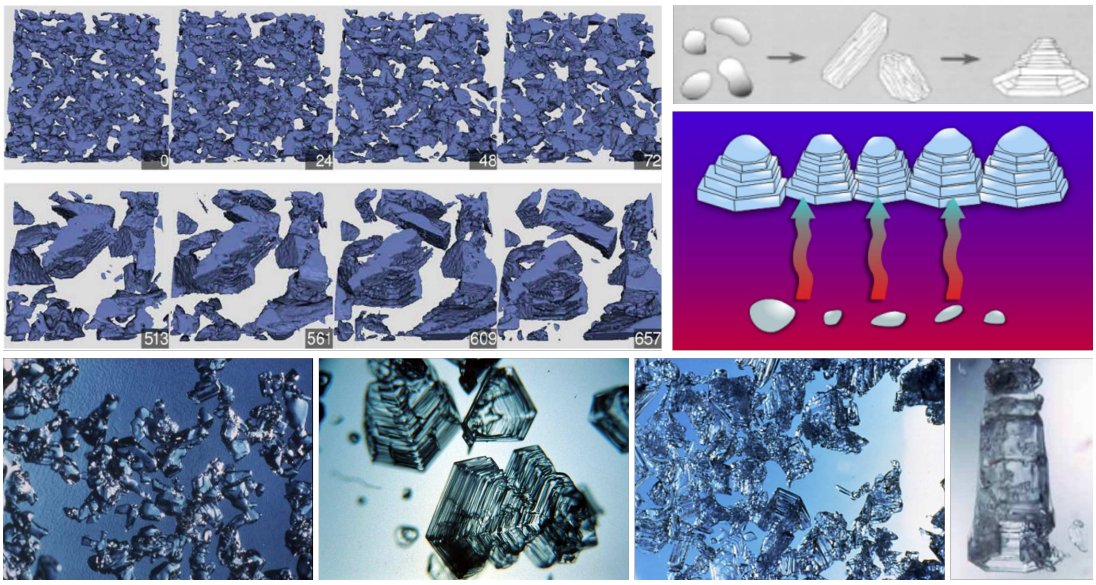

Figure 3.6: Medium to high gradient metamorphism. Courtesy: AINEVA - Trento - Italy.

of different grains together. In this process, there is a rapid settling: the snow compacts due to the reduction of pores between the crystals.

Medium/high gradient metamorphism

If the temperature gradient exceeds 0.5 - 0.6°C/cm, the crystals in the warmer regions of the snowpack undergo a process where they lose molecules. These molecules then transform into water vapor through sublimation, rise through the pores, and subsequently re-freeze on the surface of the colder crystals. The crystals in the upper layers grow thanks to the crystals in the lower layers and takes the forms of faceted crystals with big dimensions (3 - 4 mm of diameter).

The output of this constructive transformation are crystals with an hexagonal geometry, formed by flat faces with edges of 120° between one face and the other. They are striated, transparent, white-grayish, and glisten in the sun. This can only occur in dry low-density snow, meaning with high porosity. If this process continues, these crystals continue to grow in an organized manner and can become very large ($\sim$ centimeters). These crystals often form a fragile layer. Sometimes, they develop elongated shapes that allow the formation of a thermal bridge, enabling one cup-like structure to develop on top of another, like in the bottom-right of Fig. 3.6. This continuous growth disrupts the horizontal bonds while the vertical bonds remain relatively weak.

Isotherm

When the entire snowpack is isotherm, which means that the temperatures are close to its melting point, the snow is humid or wet. It becomes gray-

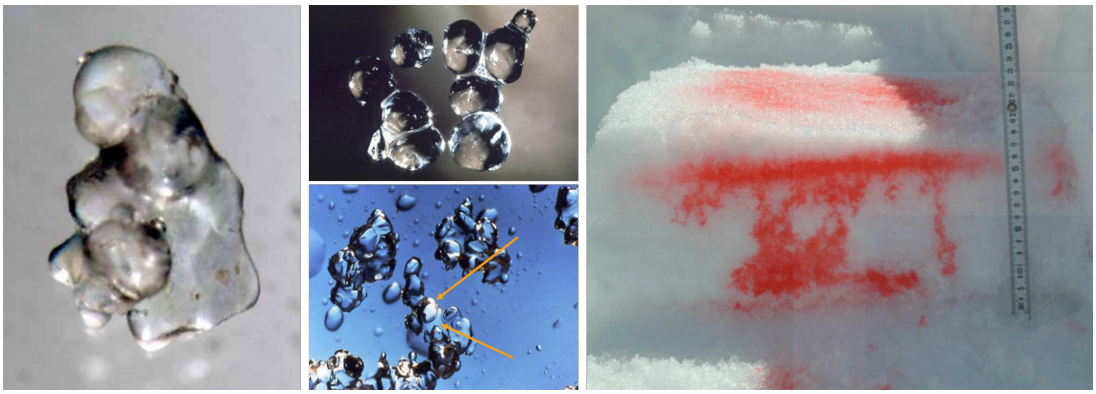

Figure 3.7: Isotherm condition. Formation of melted forms and percolating pattern of liquid water within the snowpack. Courtesy: AINEVA - Trento - Italy.

ish/translucent, with large grains, and a transparent film of water covers and connects the grains, as in the visual representation in Fig. 3.7. This liquid water will freeze during the cold nights, bonding the poly-crystalline aggregates with the water. Often, large melt-freeze crusts can form, which are stable and load-bearing in the early morning hours but tend to break during the warmer hours of the day. When the melting process is intense, very large particles form, causing the snowpack to drip. Even after a fresh snowfall, with high air temperatures, the transition is direct from precipitation crystals to fine rounded grains, and quickly to melted forms. If multiple melting and refreezing cycles occur, an irregular aggregate is formed, where it becomes challenging to distinguish individual ice grains. Everything is bonded by re-frozen liquid water.

The amount of water present in the pores can vary. If the LWC is greater than 3%, the snow is considered wet, and the water moves through capillarity, generating decent cohesion. In the initial stages of melting, the water does not percolate uniformly within the snowpack but follows preferential channels with greater porosity (layers or columns), as visible in the right figure of Fig. 3.7. However, if flowing liquid water is observed, the snow is described as very wet or saturated. The excess water has a lubricating effect: it breaks bonds and lubricates the surface of the grains, creating very dense avalanches (with snowpack density > 500 kg/m^3). Melting and refreezing cycles typically occur in spring and warm winter periods when the temperatures reach positive levels. Cold and clear nights, warm and sunny days, rainfall, steep slopes exposed to the sun, and high-density snow are also required.

Other metamorphism: wind and sun

In addition to traditional metamorphic processes, wind and sun have a significant influence on the structure and characteristics of a snowpack. Wind, specifically, plays a crucial role in a process called wind sintering. This rapid process involves fragmenting, eroding, transporting, and depositing snow, leading to the rounding

Figure 3.8: Wind sintering creating sastrugi on the left; Firnspiegel on the right. Courtesy: Atsuhiro Muto - National Snow and Ice Data Center, AINEVA - Trento - Italy.

of snow grains. The mechanical pressure exerted by the wind facilitates the bonding of snow crystals, known as sintering, resulting in the formation of wind slabs with highly compacted surfaces. Furthermore, prolonged periods of strong wind can have a profound impact on the snow surface, resulting in the formation of pronounced and durable roughness known as sastrugi (Fig. 3.8, on the left). These wind-eroded features give the snow surface a distinct rugged appearance, indicating the forceful interaction between the wind and the snowpack.
During melting, the direct sunlight radiation acts on the first millimeters on the snowpack and forms a thin and lucid layer of frozen vapour, called "*firnspiegel*" (Fig. 3.8, on the right). The surface is smooth and there's often an empty layer between the crust on the surface and the snowpack underneath. The *firnspiegel* exhibits extremely low resistance. If the crust is covered, the new layer will have difficulty bonding to the crust, creating a potential sliding plane for avalanches. The distribution of crusts is non-uniform as it depends on molecular and localized interactions within the snowpack.

3.2 Dry snow monitoring

When there is no liquid water present within a snowpack, it is referred to as dry snow. Dry snow can exhibit either a light and powdery texture or feature dense layers and depth hoars. It forms under cold temperatures and low humidity conditions. Through the type of metamorphism it undergoes, it plays a crucial role in snowpack formation, providing (or not) stability and cohesion. Understanding the characteristics and dynamics of dry snow is essential in various fields, including snow science, avalanche forecasting, and hydrology. Dry snow is made of ice crystals with a very high density of 917 kg/m^3, expressed with the symbol ρ_{ds} in kg/m^3. When it falls on the ground, it accumulates creating air pockets between the crystals. The porosity of the medium decreases its density. Depending on the snow condition, it can assume different values of density: freshly fallen snow

Table 3.2: Typical dry snow densities. The values comes from a general knowledge and are intended to give the perception of the different types of snow grains and their compositions.

Type of snow	**Density** ρ_{ds}
Fresh snow	30 - 150 kg/m^3
Wind-packed fresh snow	150 - 300 kg/m^3
Rounded-grain snow	250 - 450 kg/m^3
Depth hoar	150 - 350 kg/m^3

has a very low density of about 100 kg/m^3 on average, which increases with time thanks to the snow packing of the layers reaching values of 300 kg/m^3. Metamorphisms, other wind deposits, or application of loads can further increase this value up to 450 kg/m^3. Higher densities refers to extremely compact dry snowpacks, for example in presence of ice crust due to the melting-refreeze process, or with liquid water inside the pores (wet snow, see Sec. 3.3). The typical density ranges are summarized in the table above (Tab. 3.2), and are derived from a collective understanding within the scientific community, based on theoretical studies and field validations.

The density is a crucial parameter in describing the snowpack, especially when examining it with electromagnetic waves. In the microwave domain, the density of a dry snowpack remains constant across frequencies and it is directly linked to the real part of the dielectric constant (as discussed in Ch. 2). This correlation is expressed by the equation [64]:

$$\varepsilon' = 1 + 1.83 \cdot 10^{-3} \rho_{ds[kg/m^3]} \tag{3.2}$$

In a normal range of density for Alpine dry snow, starting from 30 kg/m^3 for fresh snow, up to 450 kg/m^3, the value of ε' vary from 1.0549 up to 1.8235, respectively. It is important to highlight that this model is valid only for dry snow with such densities in the microwave domain, and it is not applicable under different conditions, such as ice or wet snow, or in other part of the spectrum. Since the imaginary part of the dielectric constant is negligible, it is possible to approximate the velocity of the EM wave in the snow through the Eq. 3.3:

$$v = c/\sqrt{\varepsilon'} \tag{3.3}$$

where c is the speed of light in the vacuum, equal to $3 \cdot 10^8$ m/s. Merging together Eq. 3.2 and Eq. 3.3, an expression for the density, directly linked with the wave speed in the medium, is found:

$$\rho_{ds} \sim 546 \cdot (c^2/v^2 - 1) \tag{3.4}$$

where ρ_{ds} is expressed in kg/m^3 and c and v in m/s. Finally, the SWE is computed as follow:

$$SWE = D \cdot \frac{\rho_{ds}}{\rho_w} \tag{3.5}$$

where D id the snow depth and ρ_w is the water density of 1000 kg/m^3.
In order to investigate these quantities, the radar instrument introduced in the previous chapter is an useful tool and thanks to its portability, it could be brought in any snowy location. For dry snow, the depth of the snowpack and its dielectric constant is computed. In the next section, measurement campaigns in Alpine sites will be discussed and the results obtained using the Snowave radar will be presented.

3.2.1 Dry Snow Campaigns

During the winter seasons of 2022 and 2023, a series of field measurements were carried out, in the framework of the Agenzia Spaziale Italiana - Italian Space Agency (ASI) project "CRIOSAR: Applicazioni SAR multifrequenza alla criosfera"[4] collaborating with other Italian colleagues and institutions . The Snowave radar system was employed in each campaign and compared against manual analyses conducted in the same spot. Each measurement site exhibited distinct characteristics in terms of snow depth and density, necessitating the use of various frequency bands. In 2022, due to limited snow conditions in the Alpine area, the campaigns were concentrated between February and March, as well as for the unique date of 2023:

- Torgnon, Valle d'Aosta, Italy, 15/02/2022
- Cheneil, Valle d'Aosta, Italy, 01/03/2022
- Lazaun, South Tyrol, Italy, 15/03/2022
- Cime Bianche, Valle d'Aosta, Italy, 06/03/2023

The campaigns are presented below, and for each of them the setup was as in Sec. 2.1 with $s_1 = 0.3$ m and $s_2 = 0.7$ m. These distances are the results of previous studies, in order to find the best trade off between the resolution of the system and its physical dimension. Theoretically, the first receiver should stay very close to the transmitter, ideally in the same position as in a monostatic configuration, while the second should be posed at an infinite distance. However, in the practical case, this configuration is not possible to achieve. The first receiver is placed at 30 cm from the transmitter, leaving space for the antenna itself (the biggest one is roughly 17 cm), while the second receiver is placed at

[4]grant agreement n. ASIN.2021-12-U.0.

70 cm. This last value is chosen taking into account the length of the coaxial cables. Moreover, in the original setup the antennas were screwed on a track in order to completely fix the position. Indeed, this bar was 1 m in length, imposed constraints on the distances between the radiators. This configuration was tested several times, working well in both the physical and analytical way. In the setup used for the field campaigns reported in this thesis, this tack was suppressed, but the antennas still kept the same distances.
Once collecting the measurements, they need to be analyzed. The process flow for dry snow is straightforward and it relies only on the time-domain signal received after propagation. After combining the traces from the first and second receivers, a combination of the peaks is identified, and Eq. 2.7 and Eq. 2.8 are applied to those values. The number of measurements was variable, depending on the snow and weather condition[5]. As mentioned, certain results can lead to nonphysical scenarios, such as negative snow depth or extreme values of the dielectric constant, either less than 1 or significantly greater. Nonetheless, thanks to the sweep speed of the instrument and its ease of portability, a substantial number of measurements can be acquired in a matter of minutes, considerably reducing the possible issues.
After collecting and analyzing the radar traces, a comparison between the results and the same parameters taken with a manual analysis is done. It is important

[5]As visible from the picture of Lazaun, doing measurements in the field means that sometimes could happen to work in a harsh climate, with extremely cold temperatures, wind or precipitations. This is a problem not only for the operator, but also for the instruments, which are more sensible to the drop of temperature o to the direct exposition to water.

Figure 3.9: Locations of the dry snow measurements campaigns. From the top-left, the sites of Torgnon (15/02/2022) and Cheneil (01/03/2022); on the bottom, the site of Lazaun (15/03/2022) and Cime Bianche (06/03/2023) from the left.

to highlight that the aim of this work is not to investigate the precise features of a specific site, but instead to evaluate the performance of the radar system several times in different conditions, checked against ground truth observations.

Torgnon, Valle d'Aosta

The first dry snow campaign took place in Torgnon, Valtournanche, Valle d'Aosta (45°50'39"N, 7°34'41"E) in collaboration with the University of Milano-Bicocca (UNIMIB). The site was located at an altitude of approximately 2100 m above sea level (a.s.l.). The site of Torgnon, property of ARPA - Valle d'Aosta, is equipped with various instruments for weather monitoring and to reach it an hiking of roughly 2 hours was needed. The snow condition was scarce but still sufficient to allow several measurements. The measurements taken in the field were done with Snowave radar in S and C band, 2 - 3.5 GHz and 5.5 - 8 GHz, respectively, together with a manual analysis, in order to have a comparison for the post processing results. The measures were taken several times in a small space, in order to average possibly inaccuracy due to terrain, local ice layers or presence of buried bush. Nine measurements were taken in S band in 5 different positions; in C band, 4 measures have been taken in 4 different positions. For these measurements, the snow thickness was enough to allow the use of horn antennas connected to the waveguides in order to increase the directivity. It's worth noting that some of the measures have to be discarded, because they returned nonphysical results by applying the Snowave equations. Nevertheless, using a GPR-like analysis on the single trace, thus supposing the velocity of the wave and therefore its ε', these data can return valuable results, even if they are based on *in-situ* observations. Without any clue on the density and, consequently, on the dielectric constant, the results of the single trace would suffer from significant ambiguity.
The results of the available radar traces and their average, compared with the ground truth, are shown in Fig. 3.10, depicting also the standard deviation of the set of results, while the averages of each band are reported in Tab. 3.3. A total depth of 50 cm was measured with a snow probe. Density samples were taken for each layer with a cylindrical cutter and a scale to weight the sample, returning a bulky density of 298.333 kg/m^3, equivalent to an average ε' of 1.546. From there, the SWE was computed (149.2 mm).

Cheneil, Valle d'Aosta

The second test was conducted in the Valtournanche, near the village of Cheneil (45°51'49"N, 7°38'52"E) at the same altitude of the Torgnon site, i.e. 2100 m a.s.l. This site was of easy access, reachable in only 15 minutes walking. The snow was dry at that moment, but it was clear that it underwent to a strong metamorphism due to high gradient. The measurements were taken several times in the same area, 6 in C band (with horn) and 6 in X band (8 - 12 GHz). The results of the available radar traces are presented in Fig. 3.11, and the average of

the entire dataset is compared to the manual analysis, for what concern depth, density and SWE. In Tab. 3.4, the average results are divided per each band. The manual analysis retrieved values of temperature, always below 0°C, density and hardness. The total depth was 70 cm, with a bulky density of 243.61 kg/m^3, corresponding to a ε' of 1.446. The SWE has a value of 170.53 mm.

Lazaun, South Tyrol

The last site of 2022 was situated in South Tyrol, specifically in the area of Lazaun (46°44'58"N, 10°45'32"E) at an elevation of 2500 meters above sea level. This campaign was carried out together with the colleagues of the Institute of Earth Observation - Eurac Reserach, a research institute of Bolzano, South Tyrol. The site was easily reachable with a lift, since it is close to the ski resort Alpin Arena Schnals Senales. The snow depth was greater than the previous times, and the constructive metamorphism was not so distinct. Measurements were done in three bands: 7 measures in C band; 7 in X band; 7 in S band. Unfortunately, the C band measurements have been compromised, probably due to a wrong calibration of the system[6]. The mean results of the available radar traces are shown in Tab. 3.5, divided per each band, while the complete dataset is depicted in Fig. 3.12 and its average is compared to the ground truth. Indeed, the manual analysis shows a total depth of 1.04 m measured with a snow probe, with a density of 308.9 kg/m^3 ($\varepsilon' = 1.565$ using Eq. 3.2) and a SWE of 321.26 mm (Eq. 3.5).

Cime Bianche, Valle d'Aosta

During the winter of 2023, unusually high temperatures caused rapid melting of the scarce snow cover as soon as it accumulated. Consequently, identifying accessible and safe locations with a moderate amount of dry snow was a challenge. The approach chosen was to venture to higher altitudes at most one week after a fresh snowfall. Fortunately, temperatures dropped at the beginning of March, and a suitable spot with dry snow was identified at the Cime Bianche location (45°55'17"N, 7°41'35"E) in Valtournanche, Valle d'Aosta, at approximately 3100 meters a.s.l. The site was easily reachable with the lifts, since it is close to ski resort Cervino Ski Paradise. The location was carefully chosen in a flat area, very close to the terminus of the Ventina glacier, buried below the snow cover, but the variability of the amount of snow and its conditions was very high. The snow depth was high, and the constructive metamorphism was highly visible in the bottom layers close to the ground. An ice crust below the surface makes difficult digging the pit for the manual analysis. Measurements were done in S, C and X band, 5 measurements each. The results are shown in Fig. 3.13, reporting the single measurement's depth, density and SWE and the total average tested

[6]In this campaign and in few others, the VNA's software related to the calibration creates some problems, making mandatory to use a normalization of the radar trace instead, and therefore being more inaccurate and delicate.

against the ground truth. Tab. 3.6 shows the average results divided per each band. The manual analysis shows a total depth of 88 cm, with a density of 308.9 kg/m^3 ($\varepsilon' = 1.565$) and a SWE of 321.26 mm.

Table 3.3: Average results for the Torgnon site for each frequency band. D is expressed in m, ρ_{ds} in kg/m^3, SWE is in mm.

Band	D	ε'	ρ_{ds}	SWE
S	0.513	1.568	310.4	155.8
C	0.541	1.253	138.4	78.0

Table 3.4: Average results for the Cheneil site for each frequency band. D is expressed in m, ρ_{ds} in kg/m^3, SWE is in mm.

Band	D	ε'	ρ_{ds}	SWE
C	0.707	1.287	156.5	110.5
X	0.707	1.507	277.2	195.7

Table 3.5: Average results for the Lazaun site for each frequency band. D is expressed in m, ρ_{ds} in kg/m^3, SWE is in mm.

Band	D	ε'	ρ_{ds}	SWE
S	1.042	1.668	365.0	380.4
X	1.071	1.594	324.5	346.3

Table 3.6: Average results for the Cime Bianche site for each frequency band. D is expressed in m, ρ_{ds} in kg/m^3, SWE is in mm.

Band	D	ε'	ρ_{ds}	SWE
S	0.813	1.484	264.5	215.1
C	0.784	1.709	387.5	303.8
X	0.692	1.422	230.5	159.6

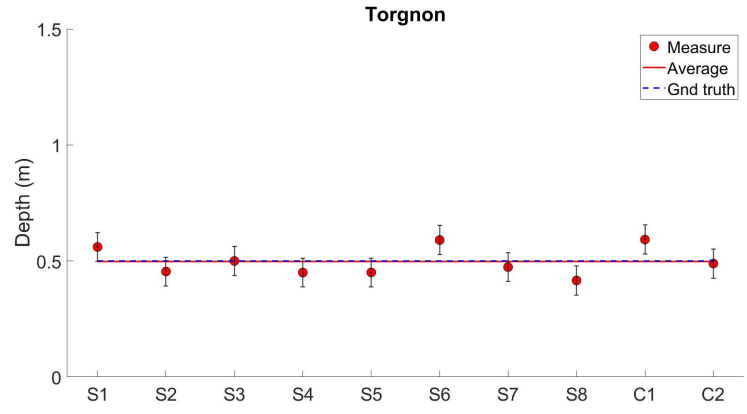

(a)

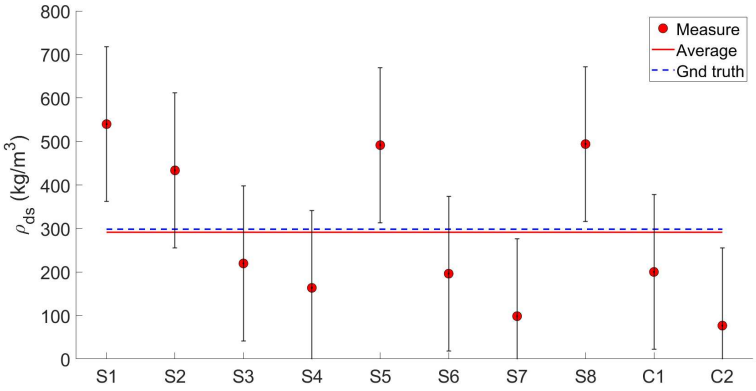

(b)

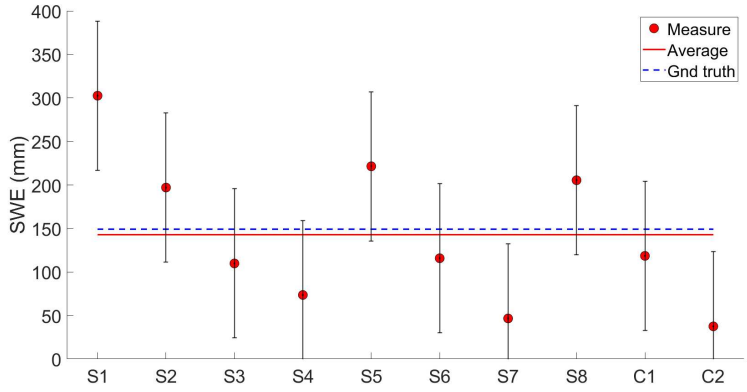

(c)

Figure 3.10: Results of the dry snow measurements campaigns for the site of Torgnon: first graph is for the depth, the second is for the density and the third for the SWE. In each graph, the red dots are the single measurement, combined with the computed standard deviation. The red continuous line is the mean, while the blue dashed line is the ground truth.

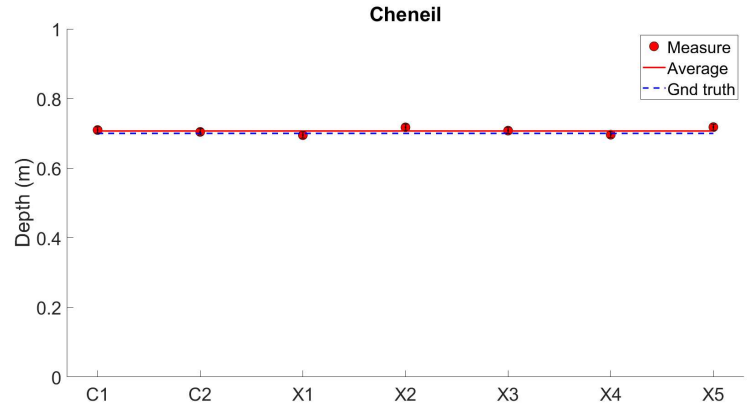

(a)

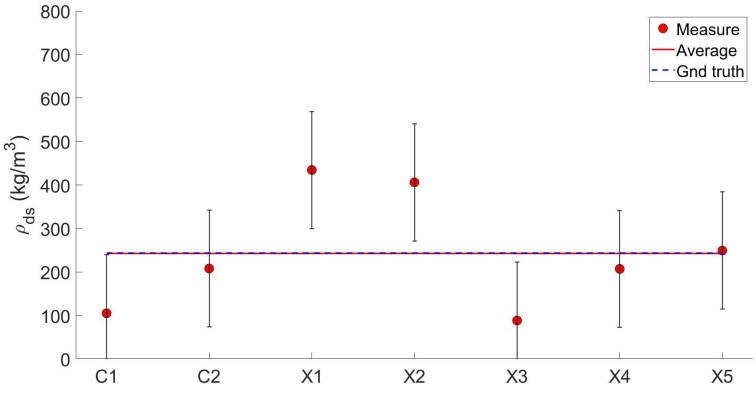

(b)

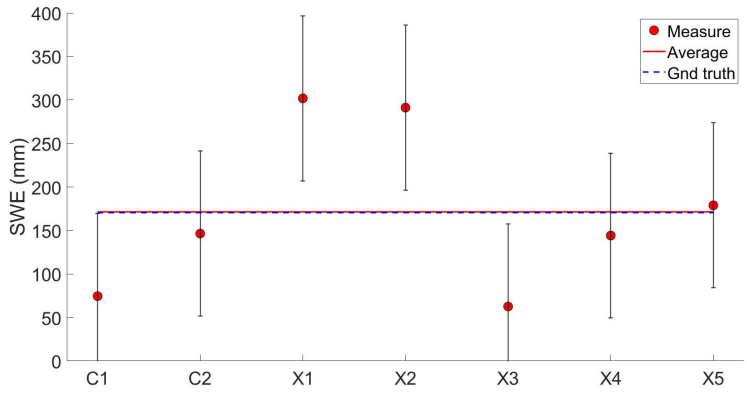

(c)

Figure 3.11: Results of the dry snow measurements campaigns for the site of Cheneil: first graph is for the depth, the second is for the density and the third for the SWE. In each graph, the red dots are the single measurement, combined with the computed standard deviation. The red continuous line is the mean, while the blue dashed line is the ground truth.

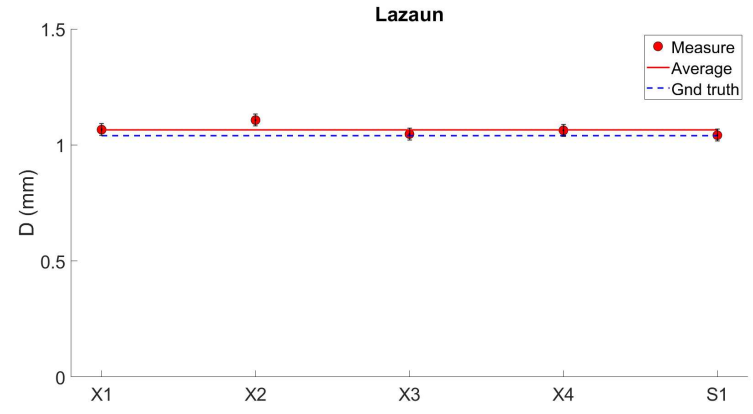

(a)

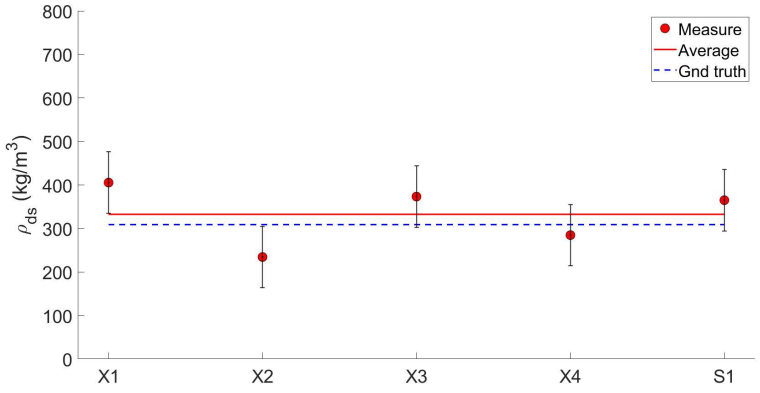

(b)

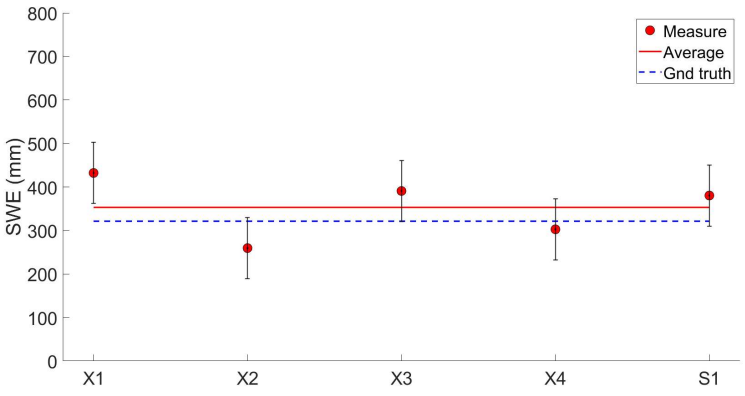

(c)

Figure 3.12: Results of the dry snow measurements campaigns for the site of Lazaun: first graph is for the depth, the second is for the density and the third for the SWE. In each graph, the red dots are the single measurement, combined with the computed standard deviation. The red continuous line is the mean, while the blue dashed line is the ground truth.

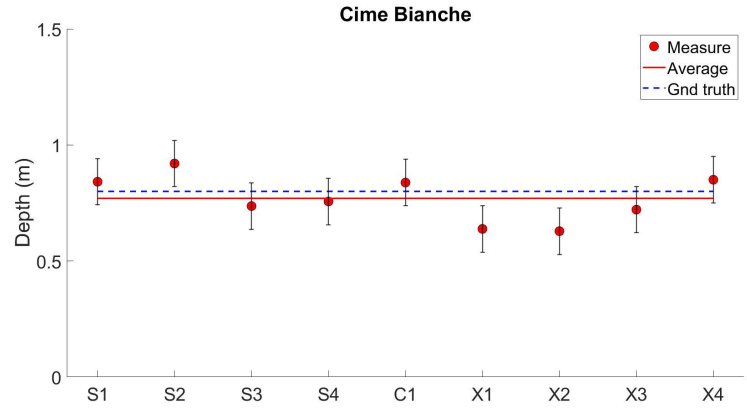

(a)

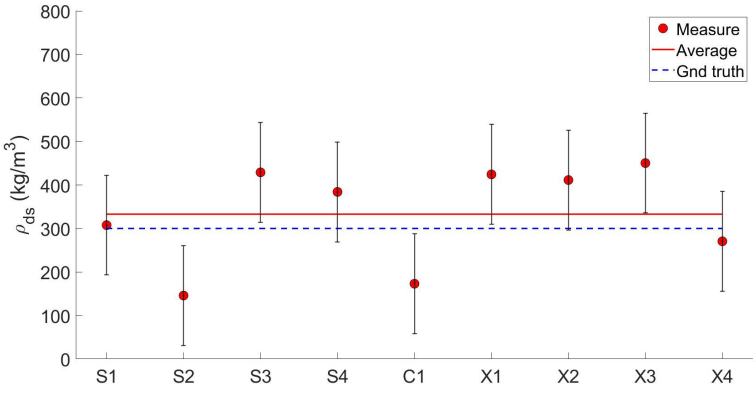

(b)

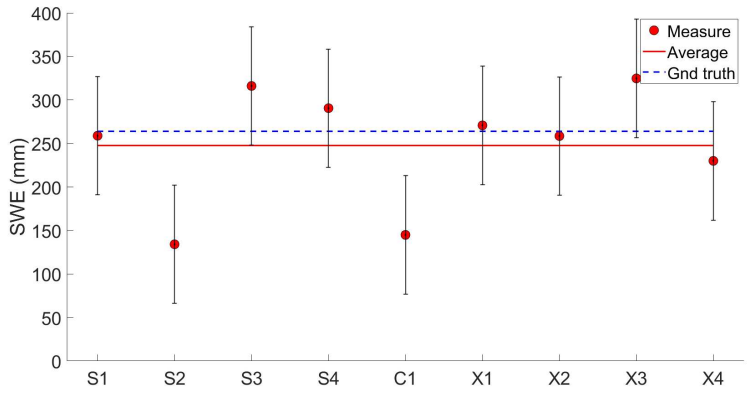

(c)

Figure 3.13: Results of the dry snow measurements campaigns for the site of Cime Bianche: first graph is for the depth, the second is for the density and the third for the SWE. In each graph, the red dots are the single measurement, combined with the computed standard deviation. The red continuous line is the mean, while the blue dashed line is the ground truth.

Conclusion on the dry snow results

All the sites experienced a moderate snowpack, ranging from 50 cm to approximately 1m of height. The radar measurements in the first graph of each site demonstrate that Snowave is highly accurate in computing snow depth, particularly when considering the total average. In fact, the averages of the measurements and the ground truth exhibit a strong agreement, with a very low standard deviations σ, represented with black vertical lines ($\pm\sigma$ with respect to the sample), especially for the sites of Cheneil and Lazaun. The snow densities are determined by applying the Eq. 3.2 to Eq. 2.8, directly computed from the radar echo and represented in the second graph of each site. While the mean density values closely match the ground truth, it's important to consider the relatively high standard deviations. This variation may be attributed to the fact that the value resulting from Eq. 2.8 represents an equivalent ε_r for the entire medium, taking into account different layers, such as melted surface, air bubbles e.g. due to buried bushed, or ice crusts. The same concept is applied to the SWE in the third graph of each site, which exhibits a good matching in average values, but an high σ still persists, directly coming from the relative density value. The high standard deviation, mostly for what concern the density and the SWE, is related to the computation of the ε' from the radar traces. Indeed, a small variation of that parameter, even if it lays in the dry-snow range, can bring to huge differences in density and SWE, due to the non-linear relationship between ε' and the density itself. To soften this problem, a multitude of measurements is taken in the field campaigns to average the results and return accurate quantities. The total average values are compared in Tab. 3.7, where the errors between the average and the ground truth are explicated. Moreover, a visual insight of the results compared to the ground truth is shown in Fig. 3.14, where the depth is expressed in m, ρ_{ds} in g/cm^3 and the SWE in m.
It's noteworthy that different bands can produce results with a different accuracy: the X-band signal is particularly sensitive to variations in ε' and, consequently, to the snow layers. Each interface generates a back-scattered signal recorded by the radar receiver, creating several peaks in the time-domain trace. Thus, identifying the bottom interface between snow and soil can be challenging and may lead to erroneous results. Therefore, each measurement must be visually inspected by an operator when using the X band configuration. Nevertheless, probably for this reason, the X band provides the more accurate results in terms of depth, density and SWE, with a percentage of errors of 7.4%, 34.5% and 27.2% respectively. The C band and the S band are slightly less accurate, especially when computing the density and the SWE. For the C band, a lot of radar samples were discarded due to problems during the campaigns or scarce resolution, wrong positioning, use -or not- of the horn antennas.
The different bands used in the tests help to overcome limitations due to snowpack's conditions, thus being always able to penetrate it to the bottom and record meaningful traces. Merging all the measurements together can bring to very accurate results, averaging local discrepancies.

Table 3.7: Summary of results for dry snow campaigns (R) compared to the ground truth (M): depth, density, and SWE. The error (E) of the measurement with respect to the manual analysis is represented the percentage.

	D (m)			ρ_{ds} (kg/m^3)			SWE (mm)		
Torgnon	0.50	0.52	4.0%	298.3	285.8	4.0%	149.2	144.7	3.0%
Cheneil	0.70	0.71	1.4%	243.6	242.7	0.4%	170.5	171.5	0.5%
Lazaun	1.04	1.07	2.9%	308.9	332.6	7.8%	321.3	353.1	9.9%
Cime B.	0.88	0.77	3.8%	300.0	332.9	11.0%	264.0	247.6	6.4%
	M	R	E	M	R	E	M	R	E

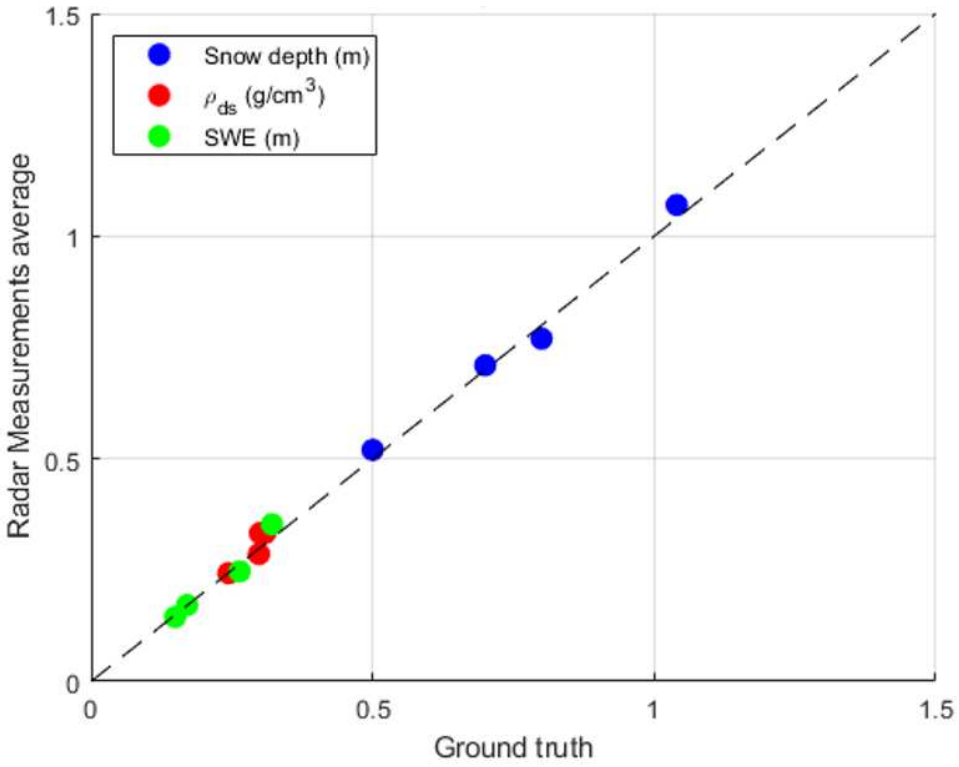

Figure 3.14: Summary of results for dry snow campaigns compared to the ground truth: depth, density, and SWE. Graphic interpretation.

3.3 Wet snow monitoring

When the content of liquid water LWC is different from zero, the snow's moisture increases, causing it to become wet. This transformation often occurs during spring and warm periods in winter when snow starts to melt, enveloping the grains in liquid water (refer to Fig. 3.15). This process results in rounded edges, the breaking of direct bonds, and the formation of large, rounded grains and poly-crystalline aggregates, which include ice grains and frozen water.
The quantity of LWC defines the effect of the water on the snowpack [65][66]. Up to $\sim 8\%$ of LWC, the humidity increases in the snowpack but it is still not visible. The grains are glued together by water molecules inside the menisci and the air is still present within the pores between the snow grains. This range of LWC is referred to as the "*pendular regime*". The "*funicular regime*", on the other hand, occurs when LWC exceeds $\sim 13\%$. At this point, water fills the gaps and creates a continuous water matrix between the grains. Air is still present in form of isolated bubbles. Between these two regimes, there exists a transition zone where the snowpack undergoes changes in its water distribution. The characteristics of this transition zone depend significantly on the snowpack's metamorphic stage and on the air conditions, such as temperature and humidity. Wet snow has different EM behavior with respect to dry snow. Water is a lossy medium which attenuates the EM signal of a radar system. The imaginary part of the dielectric permittivity ε'' becomes relevant and its value depends on the quantity of water in liquid form. Also the expression of the real part of the permittivity changes its expression, depending not only on the dry snow density, but also on the liquid water content. Moreover, for wet snow the frequency comes back to play a role. The new equations are shown in Eq. 3.6 [64].

$$\begin{aligned}
\varepsilon' &= 1 + A + B + C \cdot \frac{1}{1 + (f/f_0)^2} \\
\varepsilon'' &= C \cdot \frac{f/f_0}{1 + (f/f_0)^2} \\
A &= 1.83 \cdot 10^{-3} \rho_{ds[kg/m^3]} \\
B &= 0.02 \cdot LWC_{[\%]}^{1.015} \\
C &= 0.073 \cdot LWC_{[\%]}^{1.31}
\end{aligned} \tag{3.6}$$

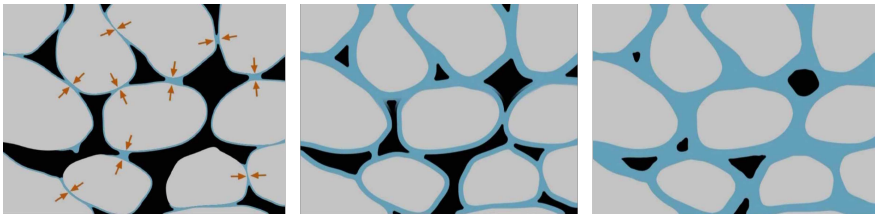

Figure 3.15: Grain after the destructive metamorphism (melting). Courtesy: AINEVA - Trento - Italy.

In these equation, ρ_{ds} is the dry snow density, measured in kg/m^3, f is the working frequency in GHz, f_0 is the relaxation frequency[7] whose value is around 9.07 GHz, and LWC is measured in volume percentage. Even if the imaginary part of the dielectric constant is different from zero, for values lower than 1/10, it results much lower than ε' and it can be neglected, making Eq. 3.3 a valid approximation even for wet snow condition [67]. Actually, up to few GHz, the value of ε'' is not always lower than 1/10. However, it was proved that it is possible to stretch a bit this constrain, and apply the same approximation even for values slightly greater than 0.1, without any big effect on the resulting velocity. For wet snow, the density (ρ_s) of the entire snowpack cannot be directly derived from the relative permittivity. Nevertheless, it can be computed using the following relationship (Eq. 3.7):

$$\rho_s = \rho_{ds} \cdot (1 - LWC/100) + \rho_w \cdot LWC/100 \tag{3.7}$$

which is a combination of the dry snow density, i.e. the density due to ice crystals and air, and the water density, equals to 1000 kg/m^3, depending on the percentage of liquid water within the snowpack.
As mentioned before, the electromagnetic signal penetrating into the snowpack is attenuated, depending on the dielectric losses. This translates into the approximation of the dissipation factor α_w, which also depends on the working frequency:

$$\alpha_w \sim \frac{\pi f \varepsilon''}{c\sqrt{\varepsilon'}} \tag{3.8}$$

Therefore, after computing the dielectric permittivity from the Snowave equation (Eq. 2.8), it is possible to derive the value of ε'' from the equation above.
The effect of the attenuation on the radar response can be visualized with the radar equation, comparing the power collected at the receiving hands P_1 and P_2 with the transmitted one P_t, as in the equations below:

$$\begin{aligned} P_1 &= P_t \cdot \frac{G_1^2 \lambda^2 S_1}{(4\pi)^3 d_1^4 L_1} \\ P_2 &= P_t \cdot \frac{G_2^2 \lambda^2 S_2}{(4\pi)^3 d_2^4 L_2} \end{aligned} \tag{3.9}$$

In these expressions, P_t is the power emitted by the transmitting antenna, G is the gain of the antenna, λ is the wavelength of the signal in the medium (the snow in this case), S is the Radar Cross Section (RCS) at the bottom of the snowpack, d is the propagation distance of the EM signal from the transmitter

[7]The relaxation frequency is a property of materials that indicates the characteristic frequency at which dielectric relaxation occurs. Dielectric relaxation refers to a material's ability to restore its polarization after being subjected to an electric or magnetic field. In the field of materials physics, the relaxation frequency represents the speed at which this restoration process takes place.

to the receiver and L is the loss value due to the dissipation factor α_w along the path. The index (1 or 2) refers to the path between the transmitter tx and the first rx_1 or the second receiver rx_2, respectively. To directly involve the dissipation factor, L can be written as follow:

$$\begin{aligned} L_1 &= e^{2d_1\alpha_w} \\ L_2 &= e^{2d_2\alpha_w} \end{aligned} \tag{3.10}$$

These formulas approximate a wave propagating inside a medium and, therefore, don't take into account the effect on the interfaces, such as reflections, scattering, diffusion and so on. Even without these effects, the approximation works well for this purpose. Since the radiated power is not always easy to estimate[8], a differential approach results to be more robust, eliminating the problem of the transmitting power:

$$\frac{P_1}{P_2} = \frac{G_1^2 S_1 d_2^4 L_2}{G_2^2 S_2 d_1^4 L_1} = (d_2/d_1)^4 \cdot e^{2(d_2-d_1)\alpha_w} \tag{3.11}$$

In this expression, it is possible to approximate the gains involved in the two propagation paths of the same value, as well as for the RCS. Since the system is made in order to offer two almost-equal experiences, the differences in view angle and footprint are so small to be neglected[9].
Once computing the attenuation coefficient α_w and retrieving the value of ε'', the liquid water content LWC and the density ρ_{ds} can be finally computed through Eq. 3.6 and Eq. 3.4.

3.3.1 Wet Snow Campaigns

To test Snowave in wet snow environment, some field campaigns have been conducted in the last years (Fig. 3.16) in the framework of the ASI's project CRIOSAR. Snowave was used together with a manual analysis always done in a representative area, in order to serve as a ground truth for the radar results. The bands used in these tests did not include the X band, as its high frequency range allowed an high attenuation of the signal while penetrating and, in most of the cases, no power arrives at the receiving hand. Depending on the site and on the weather conditions, four tests were carried out in different periods:

- Lazaun, South Tyrol, Italy, 26/05/2022
- Gran San Bernardo, Italy/Switzerland, 06/06/2022
- Riale, Val Formazza, Italy, 03/03/2023
- Gran San Bernardo, Italy/Switzerland, 16/06/2023

[8]The value can change due to environmental conditions, such as the temperature or the humidity, or can be affected by the cross-talk between the radiators or by the coupling between the antennas and the snow.

[9]In other works of our group, these small differences have been considered. See e.g. [6].

Figure 3.16: Locations of the wet snow measurements campaigns. From the top-left, the sites of Lazaun (26/05/2022) and Gran San Bernardo (06/06/2022); on the bottom, the site of Riale (03/03/2023) and Gran San Bernardo again (16/06/2023) from the left.

Lazaun, South Tyrol

The site of Lazaun was already explored for a dry snow campaign in 2022, as discussed in the previous section and, also in this case, the collaboration with Eurac Research was fundamental. The wet snow campaign has been conducted at the end of May 2022 showing an extremely thin snowpack (only 39 cm, compared with the 1 m snowpack measured in the same are during March, same year). At that point of the spring season, close to the end of the melting season, the snowpack contained a significant amount of liquid water, especially in the upper layers due to high temperatures melting the surface. However, a considerable portion of this liquid water had already run off, leaving proper puddles on the soil and causing water to flow towards the bottom of the valley. The density of the snowpack was greater than 600 kg/m^3 and its equivalent dielectric constant was calculated to be 2.117. The measurements were done only in S band, since it was the only one working with such a great water content. An attempt with the C band was done, but no signal was received back. Among the 12 measures in S band, only 6 of them were usable to produce the results. These were retrieved using the Snowave equations (Eq. 2.7 and Eq. 2.8) and then following the concept flow introduced before. Therefore, values of depth, ε', ε'', α_w and LWC are found and shown in Tab. 3.8. A comparison between the radar values and the manual-retrieved parameters is proposed. For these latter, some of them are directly measured in the field, while the others are derived with equations (marked with and asterisk * in the table). The depth was measured with a snow

Table 3.8: Results for the Lazaun site for wet snow analysis. D is expressed in m, α_w in -/m, LWC in %

Parameter	Radar	Manual
D (m)	0.35	0.39
ε'	2.135	2.82*
ε''	0.3842	0.3454*
α_w (-/m)	7.57	5.92*
LWC (%)	9.40	8.70

probe, while the LWC was deduced using a Snow Sensor by the Swiss Federal Institute for Forest, Snow and Landscape Research (WSL)-Federal Institute for Snow and Avalanche Research (SLF).

Gran San Bernardo, Italy/Switzerland 2022

In June 2022, a second wet snow campaign was conducted in the Gran San Bernardo area, situated at the border between Italy and Switzerland (45°52'9"N, 7°10'21"E). Almost all the snow had melted, leaving only remnants in concave areas of the site, where the measurements were done. The snow thickness was extremely variable, requiring manual sampling with a snow probe for each measurement. The snowpack, being at the end of the melting season, had already release most part of its water component through channels and flows directly into the soil. Therefore, the remaining LWC within the snowpack was minimal. The water release process compacts the snowpack, leading to an increase in its density.

The campaign has been done merging together Snowave investigations with a manual analysis. For the Snowave acquisitions, the S-band was used and 16 measurements were done. An attempt with the C-band radiators was done, but it was soon discarded due to the inability of that band to penetrate into such dense snowpack. Half of the measurements were discarded, since they produced un-physical results. The other 50% of the dataset has been used to produce the following results. In Fig. 3.17, a comparison between the snow thickness measured for each sample with the snow probe and the depth retrieved from the radar trace is presented. The accuracy of those values is ∼80% on average: the thinner snowpacks show a more difficult detection of the relative peaks in the radar trace with respect to the thicker ones. This is due to the fact that the S_{21} parameter takes into account also the power coming from the direct path between the transmitter and the receivers, especially the first one which is placed at a

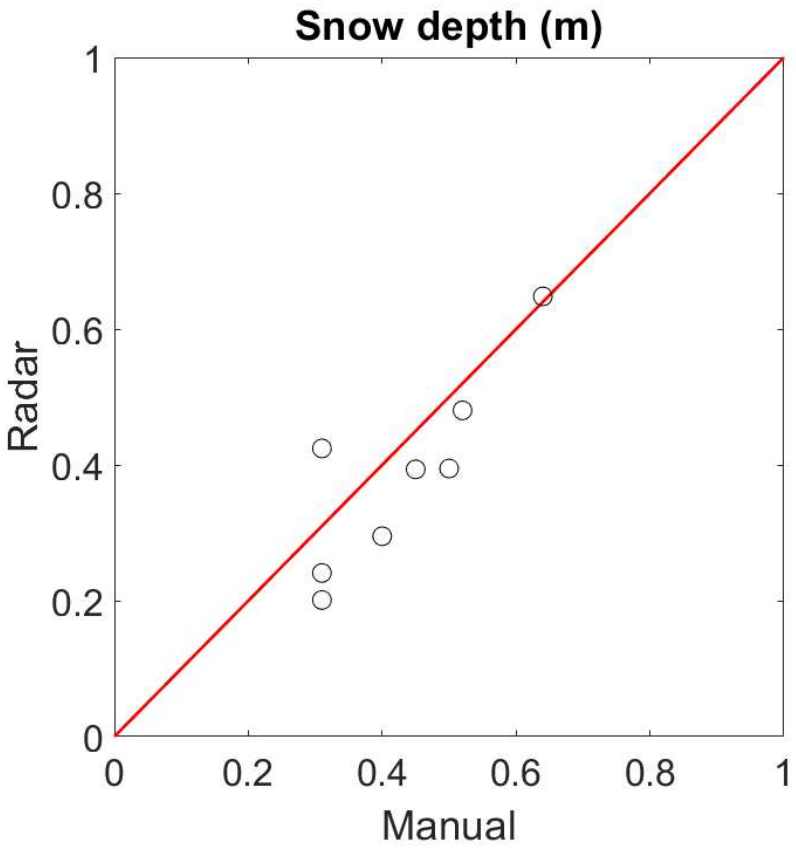

Figure 3.17: Comparison of the snow depth parameter measured with the snow probe and with Snowave for the site of Gran San Bernardo (2022).

distance of 30 cm. Therefore, when the signal is transformed in time domain, the peak relative to the cross-talk and the one relative to the interface may sum up together, being very difficult to discriminate the two components. Nevertheless, the retrieved values of ε' (from Eq. 2.8) were all in line with each other, showing an average of 2.6305 and a standard deviation of 0.3172. The average LWC, approximately 4.4%, attenuates the signal penetrating the snowpack at a rate of 21.73 dB/m. At the end, also the density was calculated, returning a value of 590 kg/m^3 on average, compared with the 570 kg/m^3 from the snow pit. In general, the results were in line with what expected and well matching the environmental condition of the site in that day. It can be noted that the majority of the results concerning the depth is underestimated, and therefore laying beneath the red bisector in the graph. This effect can be attributed to a thin layer of liquid water at the bottom of the snowpack, due to a previous percolation. This effect was also found in other campaigns, such as the one in the same site in 2023 and the extensively test in Finland (Sec. 3.3.2).

Riale, Val Formazza

At the beginning of the spring season 2023, a first field test were carried out at the Riale site, Piedmont (46°25'14"N, 8°25'7"E) on Friday, 03/03/2023, in collaboration with UNIMIB. The measurements were taken on a clear-sky day without any cloud cover, and the weather was not windy. In the morning, the temperature was low, few degree positive, probably following an above 0°C night. Indeed, the snowpack was still frozen in the first hours of the day. However, as the sun rose, the temperature increased, causing the top layer of the snowpack to melt. At the time of the manual observation, around 12:30 PM, the air temperature was +6.3°C. The snowpack exhibited a fine granular texture typical of the final stage of the destructive metamorphism process with weak gradients. The snowpack was thin, only 30 cm of snow, creating ambiguities on the radar traces, as it becomes hard to distinguish between the backscattering peak and the cross-talk between the antennas. Moreover, the unhomogeneous distribution of snow, both for what concern depth and density, makes the work more difficult. The measurements were conducted in the C-band (5.5 – 8 GHz), either with and without a horn, and in the S-band (2 – 3.5 GHz), always without horns. The total number of measurements was 49, some of which were not usable, divided as follow:

- The first set of measurements started at 10:45 AM using C-band antennas with horns. The results were very poor, making it impossible to obtain a proper interpretation of the data using the Snowave approach. One possible reason for the impossibility to retrieve results could be that the horns were too directive, making impossible the communication between the two sides of the system. Nevertheless, the first receiver was able to act like a GPR,

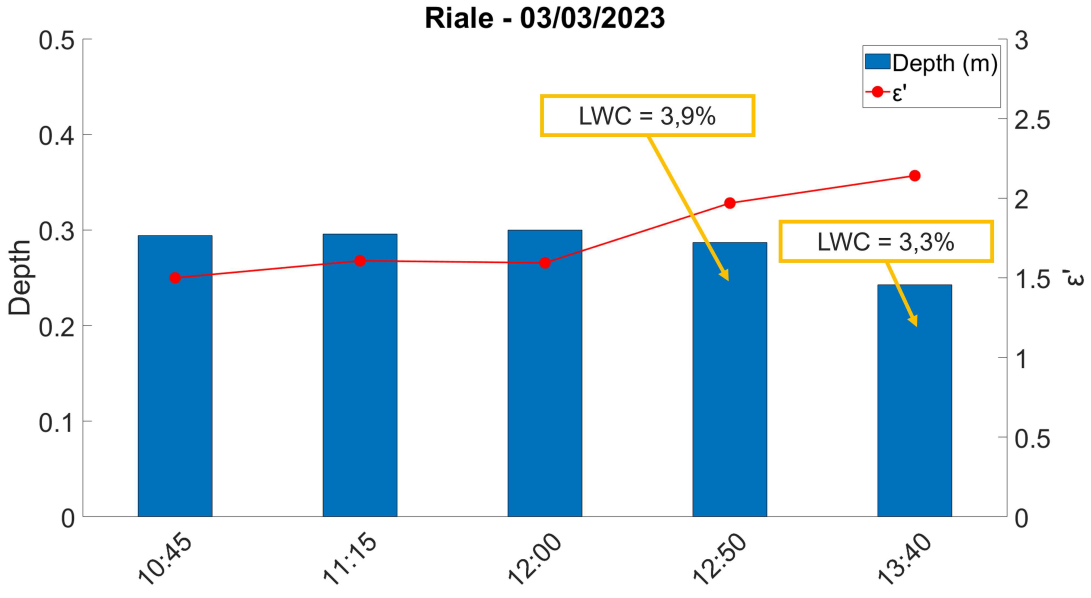

Figure 3.18: Wet snow results for the site of Riale.

and thus, assuming a reasonable value of ε' equals to 1.5 (dense snow, typical of melting-refreeze cycle, whose value was decided based on the dry snow density measured with the SLF Snow Sensor of 237 kg/m^3), it could have been possible to measure the snowpack thickness, resulting to be 29.41 cm. This result proves the limitation of the GPR, highlighting the impossibility of retrieving an accurate result without external information. The second receiver, instead, was not able to detect the power coming from the propagation within the medium, and thus it collected only noise. No valuable data were available.

- A second set of measurements was carried out 30 minutes later, at 11.15 AM. C band was used again, but the horns were removed, helping the reflected wave to be detected from both the receivers. Indeed the Snowave principle has been applied to this dataset successfully. The depth was estimated to be 29.58 cm, with a dielectric constant of 1.607. Therefore, the snowpack was still dry at this stage.

- A third cycle of measures started at 12:00 PM. The C band configuration was substituted by the S band, less affected by the attenuation in case of liquid water, which will be used from now on. Indeed, the analysis of the radar signatures highlights a snow depth of 30.02 cm, with a dielectric constant of 1.594. In the 45 minutes between this measurement and the previous one, the snow condition stay stable, showing the same behavior.

- The fourth set has been done at 12:50 PM, and the snow condition slightly changed. Indeed, Snowave highlights an higher dielectric constant ($\varepsilon' = 1.969$) in a 28.72 cm deep snowpack. Also few percentage points of liquid water were detected, specifically a value of $LWC = 3.9\%$.

- The last measurement was taken at 1:40 PM. In this case, the depth was underestimated by Snowave, showing a thickness of 24.27 cm. Therefore the ε' was overestimated at a value of 2.141, but still in line with what expected. The LWC remains stable around 3.3 point percentage.

From the manual investigation, the snow depth was of 30 cm, perfectly in line with the results found with Snowave. The dry snow density measured at 10.30 AM, before starting the radar campaign, shows a value of 237 kg/m^3. A second measurement was done at 11.20 AM, only on the surface, showing a density of 540 kg/m^3 ($\varepsilon' = 1.99$), not in line with the Snowave result at the same time. This could be probably due to the thin water film formed on the surface, detected by the SLF Snow Sensor. but not enough to change the internal features of the snowpack and weight on the bulky observation of the entire one. From investigation on the surface, the SLF Snow Sensor also detected LWC greater than 0 starting from 11.30 AM. The value were low ($\sim 3\%$) and highly variable, but they can still be used as an indication for the radar results, which are in line with it, especially for what concern the last two datasets.
This campaign was different from the others. Indeed it was a first experiment

to study the capability of the radar of investigating slightly different conditions during the melting-refreeze cycle, with a daily observation of the changes. This type observation will be better discussed later in Sec. 3.3.2, with a more extensive campaign, investigating the entire melting cycle of a polar snowpack.

Gran San Bernardo, Italy/Switzerland 2023

Gran San Bernardo, the same site of the second wet snow campaign, was visited again one year later, in June 2023. Also in this case, the melting process was at the end, leaving patches of snow only in certain areas. The snowpack can be described by a big variability, either in coverage, depth and LWC. Indeed, in the few covered areas, the thickness of the snowpack varied considerably. For this set of measurements, the local variation of the single measure was minimal, in order to have closer values. Even in this case, manual snowpack thickness samples were taken for each measure using a snow probe, complementing the radar analysis conducted with Snowave. By looking at the manual analysis, also the variation of LWC along the vertical profile was not homogeneous, sampled with the SLF Snow Sensor for each layer and then averaged. Indeed, even if the entire snowpack retains some water, the upper layers were more exposed to the warm sun rays

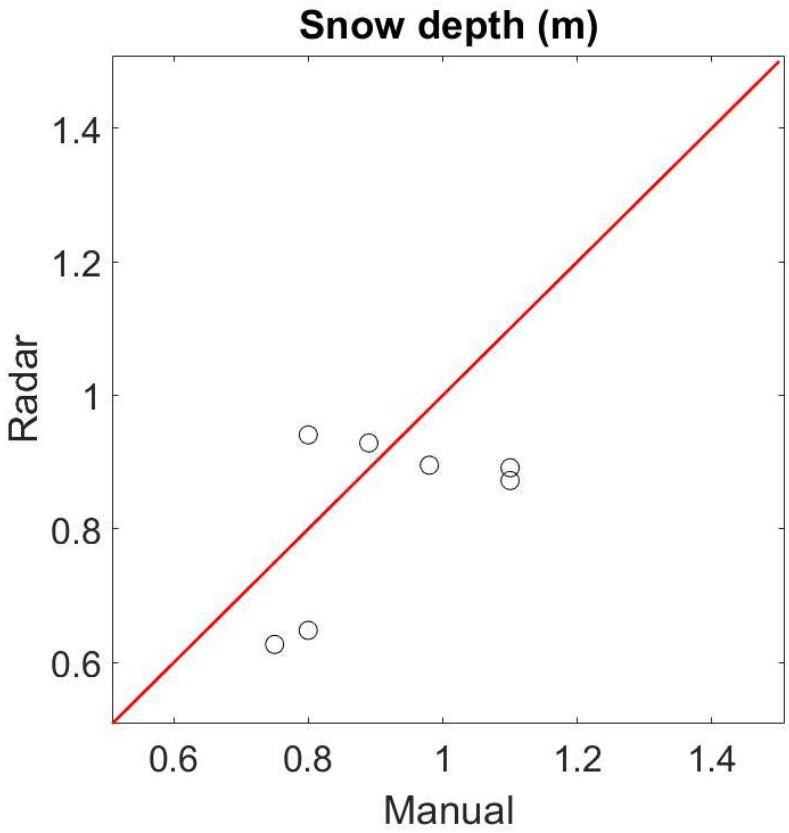

Figure 3.19: Comparison of the snow depth parameter measured with the snow probe and with Snowave for the site of Gran San Bernardo (2023).

and a water film formed on the surface ($\sim$ 12% on the surface, $\sim$ 8% in the snowpack). As well as for the other sites, Snowave investigation was followed by a manual analysis. The radar was used in L-band and S-band configuration, acquiring a lot of measurements. Unfortunately, only 1/3 of them were usable[10]. The probed snow thickness (for each measurement) and the radar-retrieved snow depth were compared and depicted in the parity plot in Fig. 3.19. The accuracy of those results is around 85% on average. Even in this case, the depth of the snowpack results to be lower than the manual analysis, except for two dots. As for other sites, this could be due to a water film (not homogeneous, different for each measurement) stored on the interface between the snowpack and the soil, making the impinging wave to reflects on it, missing some centimeters to the soil. The dielectric constant ε' assumed a value of 2.98 on average, which is very high. This can be due to the same water on the surface, which increased its bulky value. LWC assumed values between 6% and 12%, with an average of 8.23%, as for the manual analysis. The value of LWC, higher with respect to the value of 2022, can explain the greater dispersion of the results in Fig. 3.19. In this campaign, the snowpack was so full of water, thus dense, that the spring scale used in the manual density investigation went out of scale, and therefore no density information can be measured and thus compared.

3.3.2 Arctic Measurements

In order to have a complete overview of the behavior of a snowpack under the process of melting, an extensive field campaign took place in April 2023 in Arctic environment. Indeed, the polar station of Sodankylä-Tähtelä (Finnish Meteorological Istitute - Ilmatieteen laitos (FMI) Arctic Research Center (ARC)), in Finland (67°22'01"N, 26°39'04"E), hosts this measurement campaign for 15 days[11], in which part of the melting process occurred. Indeed, Fig. 3.20 visually represents the temperature fluctuations. These data are taken each hour by a weather station (blue curve) managed by the FMI, placed in the proximity of the measurements site. The red dots, instead, represents the temperature detected at the moment of the manual analysis in the field. In agreement with the temperature fluctuation, the daily melting-refreeze cycle started during the initial days of the campaign. Following this initial period, the temperature remained above 0°C even during the nighttime hours. Towards the end of the campaign, a drop in temperature occurred, leading to the freezing of the water. The snowpack at the beginning of the campaign was very dense and compact but still dry, with an height of about 70 cm. The positive temperatures of the following days increased the moisture in the snowpack, decreasing its thickness as it melts and compacts. Indeed, the thickness reduced by half at the end of the campaign. During those

[10]Ratio like this are predictable in wet campaigns. For this reason, several measurements are done in the same area.

[11]The research leading to the results during the Arctic campaign has receives Transnational Access from the European Union's Horizon 2020 project INTERACT, under grant agreement No. 871120.

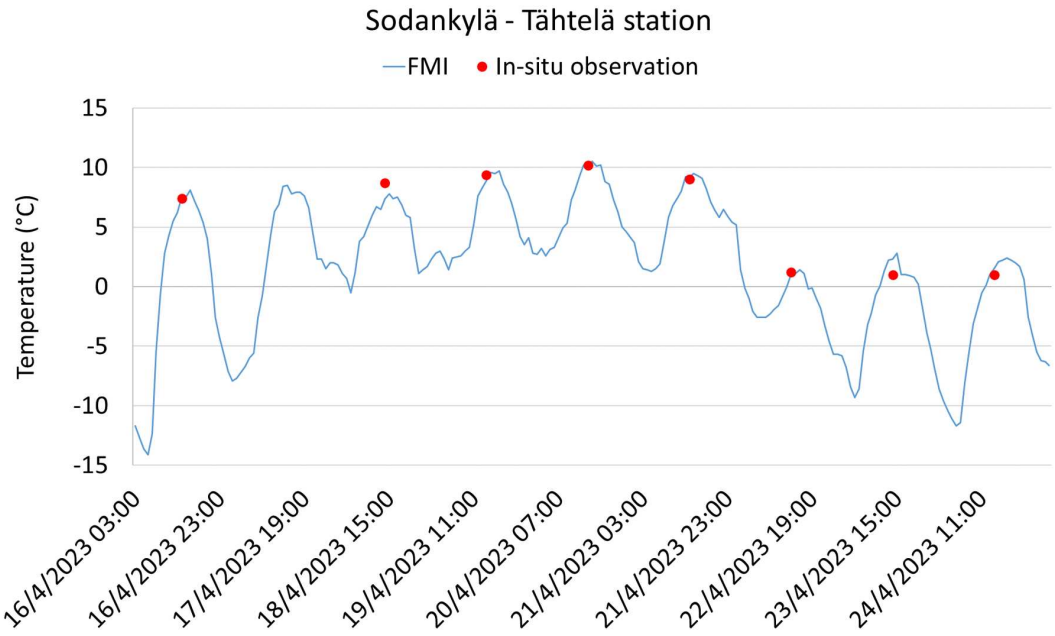

Figure 3.20: Temperature fluctuation during the 15-days campaign at the Sodankylä-Tähtelä station. The blue curve represents the air temperature measured hourly by a weather station from the FMI. The red dots are *in-situ* observations, measured during the snowpits.

days, the water formed on the surface and, at a certain level, it percolate inside the snowpack creating vertical channels. At the end, several centimeters of liquid water was stored on the bottom.
During this period, measurements were done in a flat and huge snow-covered instrumented site of about 1000 m^2 of extension, where other researches were conducted at the same time. Snowave radar measurements were complemented by manual investigations. The measurements, conducted once or twice a day, were done using L band (1 - 2 GHz) and C band (5.5 - 8 GHz) frequency bands. The instrument was placed on the snowpack surface and multiple measurements were taken in slightly different positions (within an area of about 1 m^2), to account for propagation inaccuracies due to terrain variations and surface roughness. Day by day, the location of the measurement (both by radar and manual) changed inside the instrumented site, in order to accommodate other type of measurements in the field. However, the snowpack is assumed to be homogeneous inside that area. After each set of measurements, a snow pit analysis was performed, including temperature, depth, and density measurements. Temperature readings confirmed the presence of water, with trends validated by comparisons between *in-situ* measurements and official records from the FMI (Fig. 3.20). LWC percentage was estimated using a capacitive sensor from SLF, the SLF Snow Sensor, specifically when visible inside the snowpack. The measure with SLF Snow Sensor was done layer by layer and then averaged in order to find the bulky LWC to compare with the LWC of the entire snowpack found with the radar.

The radar data resulting from the campaign are illustrated in Fig. 3.21 and compared with the ground truth measurements, obtained via a snow probe (Fig. 3.21a) from what concern the depth, and with the SLF Snow Sensor in terms of LWC (Fig. 3.21b). In the initial phase of the campaign (up to April 18), the snowpack depth closely matched the ground truth data, thanks also to the low LWC, which values are in the order of the pendular regime. Here, water molecules migrated between the menisci of the snow grains, leaving air gaps. Although a thin film of water formed on the snowpack's surface, proper channels did not develop at this stage. The quantity of water aligned with temperature trends until then. No manual investigations have been taken, since the water content was so low to not be detected by the SLF sensor. Positive daytime temperatures led to surface melting, yet the snowpack retained its thermal state due to cold nights near or below 0°C. From April 18, rising temperatures, even at night, increased LWC, reducing snowpack depth. Around April 20, LWC peaked as water percolated, forming vertical channels (in line with the funicular regime) and accumulating on the ground, sometimes several centimeters deep. This led to increased radar reflection at the snow-water interface, limiting penetration to the ground. Consequently, the Snowave-retrieved snow depth curve indicated lower values compared to the ground truth data, primarily due to this water layer on the ground. As the campaign progressed, the LWC detected by the radar decreased as water drained, releasing the snowpack from excess water. With decreasing temperatures at the end of the campaign, the liquid water froze overnight, reappearing as a surface film during the warmest hours of the day.

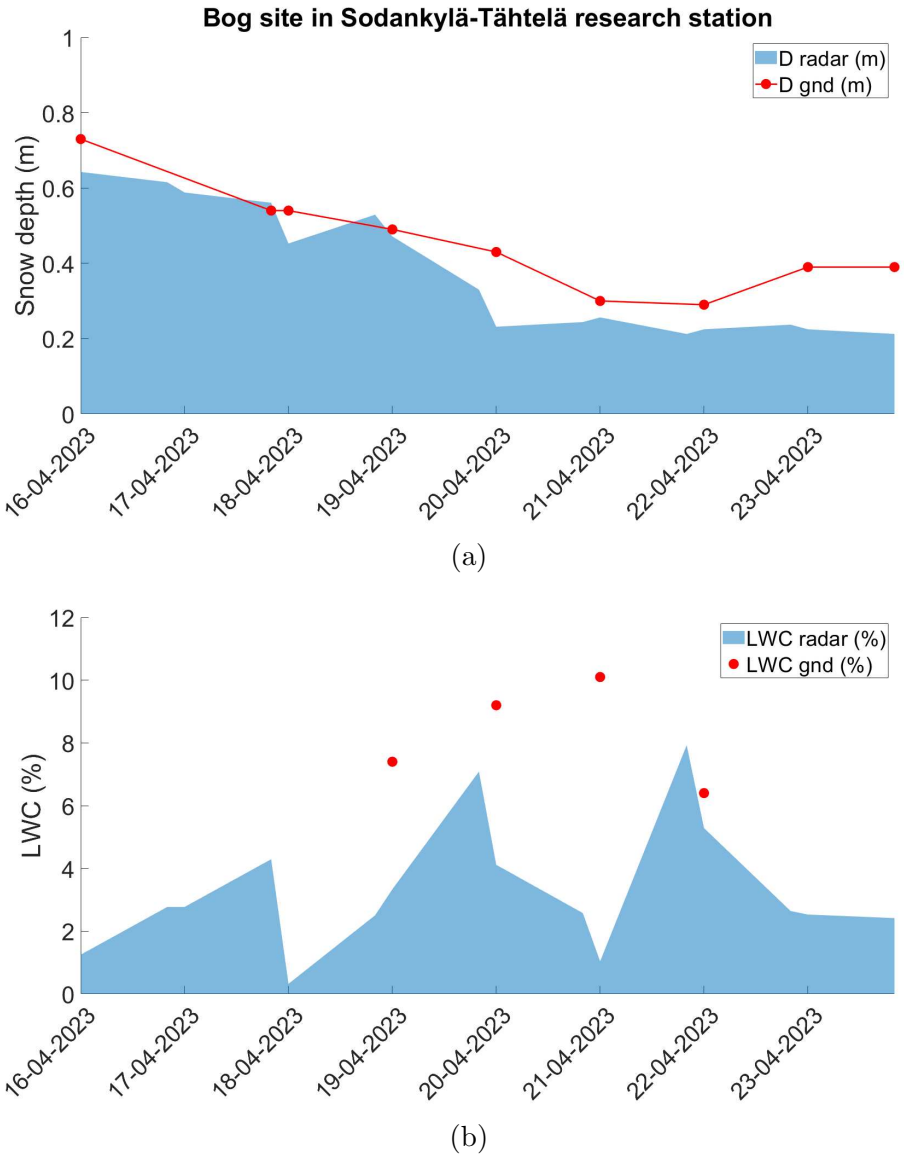

Figure 3.21: Results of the Arctic campaign: (a) snow depth, (b) LWC.

Chapter 4

Glacier monitoring

Glaciers are large masses of ice that form and move slowly on the Earth's surface. They develop when snow accumulates over many years, and subsequent pressures compress and transform it into ice. Glaciers play a significant role in shaping the surrounding landscape, contributing to the formation of glacial valleys, fjords, and other geological features. Moreover, glaciers serve as important indicators of climate variations, as their size can be influenced by changes in temperatures and precipitation. Therefore, monitoring the behavior of such natural bodies is fundamental. In this chapter, some attempts will be presented by means of the radar system Snowave.

4.1 Ice and glaciers

Glaciers have had a significant impact on the natural history of our planet. They have been present on Earth for millions of years as they primarily formed during glacial eras, i.e. geological periods characterized by very low temperatures leading to the formation and expansion of massive ice masses. Earth has gone through several glacial and interglacial periods over millions of years, during which glaciers formed and retreated in response to climatic variations. In the Alps, the most recent glaciation is known as the Last Glacial Maximum (LGM) and can be dated approximately 30000 to 19000 years ago [68]–[70]. Most of the features of the landscapes visible nowadays can be attributed to this period, even in regions relatively far from the Alps. This is the prove of the great extension of the glaciers and it can help to trace back the movements of the ice sheets, as they leave rock debris and model the bedrock while retreating [71]. As well as the landscapes, also the air trapped inside a glacier can bring information about the past. Indeed, it comes in the form of bubbles, containing different gases (including CO_2) which are investigated by the scientists to have an insight on the past atmospheric and climate conditions over millions of years [72]–[74]. Even nowadays, the study of glaciers is directly related to the climate, especially regarding the topic of global warming. Indeed, with the actual rising trend of temperatures, glaciers tend to melt and retreat very quickly. As much the temperature and the freezing level increase, even for long periods, glaciers melt and

the water can act in different ways: it can create actual rivers flowing down to the valley, or be stored in endoglacial lakes, acting as a sliding surface for the glacier itself. Therefore, the risk of collapse of ice may be very high, endangering people, constructions and human activities. Moreover, glaciers are the most precious resource of fresh water [75][76], and the fast melting due to warming temperatures can affect everyday activities, industries, agriculture, electricity, and other important services for the population. In summary, glaciers have played a crucial role in our planet's natural history and continue to do so. Therefore, in order to understand the composition of ice, to monitor the risk of collapse and to predict what will happen in the future, monitor the glaciers present on the Earth nowadays is fundamental.

4.2 Glaciers Formation and Metamorphosis

A glacier is an extended and moving mass of ice derived from transformation of snow. Indeed, it is formed from snow falling and accumulating over a long period of time, usually from 10 years for Alpine glaciers, up to 100 years in polar regions such as Antarctica, in which the snow layers undergo a process of metamorphosis [77]–[79] (Fig. 4.1). From the first days after the snowfall, the snow goes through the first step of metamorphosis, where the ice crystals, in the form of snowflakes, lose their elongated arms. The molecules melt from the sharp areas and refreeze in the concave areas close to the center of the crystal, becoming round and granular. This process continues for some time, increasing the density of the snowpack and making it more compact. After roughly one year, the snow has turned into firn, an intermediate stage before becoming blue ice. Firn is a very compact layered medium with a high density ($\sim$ 400 - 830 kg/m^3), whose value is determined by the time of formation, the metamorphosis it underwent, and the pressure applied by the layers above. Fig. 4.2 shows a vertical profile of a firn wall on Weissmiesgletscher, Switzerland. The layering is visible and the snowfall history can be traced back over a long period of time. At this stage, air pockets are small but still connected to each other. Under increasing pressure, firn grains melt and solidify into a dense mass of crystalline glacial ice, with a constant density of 917 kg/m^3. This occurs as the frozen molecules

Figure 4.1: Snow metamorphosis: from snowfalls to ice through the time.

Figure 4.2: Prominent layering in the firn is visible in the wall of a large crevasse on Weissmiesgletscher, Switzerland. Photo J. Alean.

bind together, immobilized and unable to move freely. Air can be present in form of air bubbles, not connected to each other.
One of the key features of glaciers is their slow movement, which gives rise to distinctive formations such as crevasses and seracs. This movement is influenced by the mass balance of the glacier, representing the difference between the snow accumulated (from snowfalls, rime ice, avalanches or re-freezing of glacier meltwater) and the ice lost (due to melting, sublimation, calving and wind erosion). When a glacier gains more mass than it loses, the weight of the accumulated snow in the upper area pushes the glacier's terminus downhill, causing it to move faster. On the other hand, if the ice losses are greater than the snow accumulation, the glacier moves more slowly downhill under the force of gravity. This slower movement might give the impression of glacial retreat, but in reality glaciers always move only downhill. These slow movements, driven by the delicate balance of mass gained and lost, significantly shape the landscape over time. Glaciers can carve out valleys and fjords as they advance, while during periods of retreat, they leave behind new landforms. However, the current trend of global climate change is leading to widespread glacial retreat and loss of mass, impacting freshwater resources and contributing to rising sea levels. Therefore, understanding the behavior of glaciers is crucial in studying and mitigating the effects of climate change.

4.3 Monitoring Techniques

To completely understand a glacier, several parameters have to be investigated, and thus different techniques need to be used. To monitor the movement, dimension and extension of a glacier, photogrammetry and optical satellite imagery are often used [80][81]; the albedo, i.e. the capability of the surface to reflect the solar radiation, useful to understand its thermal behavior and the contribution that it can give to increase the air temperature, also rely on the use of terrestrial photos [82]; manual analysis are still used to understand the layering of the glacier and to investigate the history, for example by extracting ice core samples by drilling the glacier itself [83]; one very important parameter is the depth, changing its value according to the snow and weather condition of the site, and it is usually done using GPR systems [84]–[88]. However, GPRs show an important limitation [89]: in order to retrieve the information about the depth of the glacier, the velocity of the penetrating wave into the medium has to be imposed. Even if the possible variation of the wave velocity[1] into the ice is relatively small (from $1.7039 \cdot 10^8$ m/s to $1.7617 \cdot 10^8$ m/s), it does not take into account the presence of the firn on top of the glacier, in which the wave is faster, which can be very thick and can completely change the computation of the depth; even the presence of water is not detectable, and possible risks cannot be predicted. When investigating thick mediums, reaching depths of tens of meters with a relatively high dielectric constant, radar instruments require robust and big equipment. Indeed, the choice of a low frequency, ideally within the tens or hundreds of MHz range, is needed, ensuring a long wavelength. This allows radar signals to penetrate deeply into the glacier, reaching its bedrock. However, low frequency leads to large antennas[2] and, consequently, heavy equipment. To transport this equipment, especially when it is required to operate in remote and challenging glacial terrains, external aids such as helicopters are often employed. Once operative on the glacier, moving a bulky instrument on the glacier surface to observe different positions is not always trivial. Different strategies can be employed: in some cases, specialized sliding carts equipped with the radar are used; in other cases, stationary measurements are taken from specific points on the glacier surface.
Another distinction can be made based on the size of the glacier: for glaciers whose extension is small, and thus the area to be covered is limited, ground based systems, Global Navigation Satellite System (GNSS) or Remotely Piloted Aircraft System (RPAS) are normally used [90]; to investigate larger areas but loosing in resolution, satellite are employed. Depending on the feature to be investigated, the system carried on board on these platforms can be different, like explained before.

[1] linked to the real part of the dielectric constant trough the Eq. 3.3, which can assume values between 2.9 and 3.1 for ice.

[2] The physical dimensions of the antennas are directly proportional to the wavelength. As the wavelength decreases with higher frequencies, low-frequency radar demands significantly larger antennas.

4.4 Glacier Monitoring Campaigns

Among the ground based radar systems, Snowave, thanks to its portability and light and small profile, can be employed too. With its dual-receiver system, Snowave can not only compute the depth of a glacier, but also measure the velocity of the wave into it, without any external aids. This allows also to investigate the presence of water inside the glacier, since it acts to increase the value of the dielectric constant. As for snow monitoring, Snowave can retrieve D and ε' knowing the ToF of the two signals recorded by the two receivers. With these information, also the density can be computed, applying a slight modification on the formula used for dry snow [91]–[94]:

$$\varepsilon' = (1 + 0.845\rho)^2 \tag{4.1}$$

where ε' is the dielectric constant computed with Eq. 2.8 and ρ is the ice density. Also the amount of water inside the glacier can be computed, using a simple proportion and approximating the value of the dry ice, without the presence of water:

$$\varepsilon'_{ice} \cdot [(D - x)/D] + \varepsilon'_{H_2O} \cdot x = \varepsilon' \tag{4.2}$$

where D, computed with Eq. 2.7 is the depth of the glacier, ε'_{ice} is the dielectric constant of the ice without the presence of water (usually between 2.9 and 3.1, in this work supposed to be equal to 3.1), ε'_{H_2O} is dielectric constant of water equal to 80, and x represents the amount of water inside the snowpack, expressed as a length. From the comparison between D and x, it is possible to compute the percentage of water inside a snowpack with a depth of D.
To conquer these results, it is really important to set the physical and computational parameters of the system in the right way. First of all, the separation between the first and the second receiver must be bigger than for snow monitoring[3]: the wave has to propagate for a longer distance, and a small difference between the two baselines[4] bring to very similar results in terms of ToFs. Also, the resolution of the VNA needs to be adapted, in order to be able to detect even a small variation between the two radar traces. This can be corrected in part also *a posteriori*, utilizing a zero-padding algorithm.
Also the radiators are different, and in this case the UHF PIFA are used (see Ch. 2). These antennas work with a central frequency of 300 MHz and very narrow Bandwidth (BW), in the order of some MHz. In order to limitate the dimension of the antennas, these are designed to be not highly directive. Due to this feature, most of the power dissipates outside the theoretical path of the wave. To increase the chance to reach the bedrock and to reflect back up to the receivers, an amplifier (see Fig. 2.7) is connected at the transmitting hand.

Two field campaigns have been conducted in the Italian Alps during autumn 2021 and summer 2023 in o,rder to test the system (Fig. 4.3), in collabora-

[3]generally $s_1 = 30$ cm and $s_2 = 70$ cm.
[4]i.e. the distance between tx and rx_1 and tx and rx_2.

(a) (b)

Figure 4.3: Picture of the two glacier campaigns: (a) Cherillon glacier, 27/10/2021; (b) Colle del Gigante, 13/07/2023.

tion with the team of Fondazione Montagna Sicura - Fondation Montagne Sûre working on glaciological risks :

1. Cherillon glacier, Valle d'Aosta, 21/10/2021 [95]

2. Colle del Gigante glacier, Valle d'Aosta, 13/07/2023

In this specific context, a comparative analysis was undertaken using data acquired from conventional GPR systems in conjunction with the measurements obtained through Snowave. The datasets utilized in this comparison, coming from prior researches, are based on continuous measurements carried out along transects on the glacier surfaces. These measurements presuppose a velocity within the medium, specifically $1.7{\cdot}10^8$ m/s, equivalent to a dielectric constant of 3.1.

Cherillon Glacier

In Autumn 2021, an experimental campaign was conducted in the Italian Alps to assess Snowave performance. The study site was the Cherillon glacier (45°57'47"N, 7°37'23"E), a small glacier situated in Valtournanche, Valle d'Aosta, at an altitude of approximately 2900 meters above sea level. Figure 4.4a illustrates the glacier area, highlighting the specific location of the measurements. In the enlarged view (Figure 4.4b), the transects from prior investigations are depicted as colored lines, and are used as referent measurements for the comparison of the results obtained from the Snowave system. Indeed, Snowave measurements were conducted at the intersection of these three transects, increasing the reference traces for the comparison. The GPR traces, depicting the three transects, are illustrated in Figure 4.5a, with vertical lines indicating the intersection with Snowave. In all three radargrams, observed interfaces were found approximately 6 meters and 31 meters below the surface. The first one represents the interface between firn and blue ice. It is worth to note that this interface line exhibits non-uniformity and varies across locations, even within the same transect. The

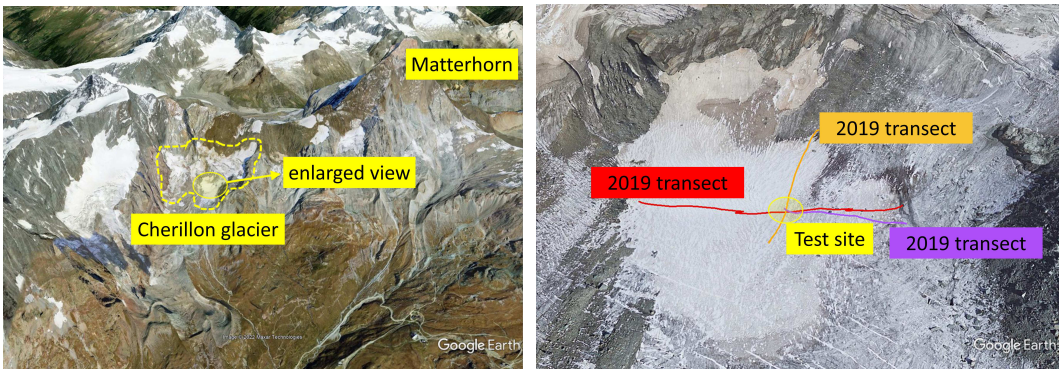

(a) (b)

Figure 4.4: Cherillon test site, Google Earth views: (a) map of the valley; (b) enlarged view. The red, orange, and purple lines are three GPR traces from 2019. The test site for Snowave was in the intersection of these three lines (yellow circle).

second interface corresponds to the bedrock. Although visually intuitive, this representation lacks precision and allows room for potential errors. Nevertheless, an interval of time where the bedrock can be placed is found: the bedrock is expected to be between 300 ns and 400 ns, which corresponds to a range between 25.5 m and 34 m supposing a velocity into the medium of $1.7{\cdot}10^8$ m/s (equivalent to $\varepsilon' = 3.1$).

During the Snowave campaign, multiple sets of baselines were tested. Ideally, the optimal configuration would involve placing the first receiver in close proximity to the transmitter and the second receiver at a considerable distance, approaching infinity in theory. However, practical constraints, such as mechanical limitations and power budget considerations, prevent achieving this ideal setup. As a compromise, the first receiver was positioned at a distance of 30 cm from the transmitter (s_1), while the second receiver was placed at 1 meter (s_2) away. With this baseline and high a number of points, the temporal resolution of the system was sufficient to detect the right peak corresponding to the bedrock, even if weak. Indeed, Fig. 4.5b shows the radar traces in time domain recorded by the first and by the second receiver relative to this setup. In the enlarged view, the interval of time where the bedrock was supposed to be is considered. The two circles corresponds to the time-samples identifying the two reflections from the bottom. The values are $T_1 = 343.42$ ns for the first couple of antennas and $T_2 = 343.3$ ns for the second. These numbers were used to feed Eq. 2.7 and Eq. 2.8, returning values of $D = 27.9$ m and $\varepsilon' = 3.395$, corresponding to a velocity in the medium of $v = 1.628 \cdot 10^8$ m/s. In terms of depth, the variation of a few meters can be attributed to several factors. Firstly, the reference data were obtained in 2019, and considering the ongoing climate trends, it's possible that the glacier has retreated since then. Additionally, the test was conducted at the end of the warmest season, suggesting that some of the snow accumulated on the glacier melted during the summer, and no fresh snowfall occurred before

the measurement. As mentioned earlier, the typical dielectric constant value should range between 2.9 and 3.1. However, the observed value falls outside this range. One potential explanation could be the presence of liquid water within the glacier. By calculating this value using Eq. 4.2, assuming a reference value of $\varepsilon' = 3.1$[5], a rough estimate for the height of the equivalent water column x can be derived. This estimation indicates a height of 10.72 cm, corresponding to

[5]The assumed value corresponds to the upper limit of the range, chosen to get closer to the ε' of the water.

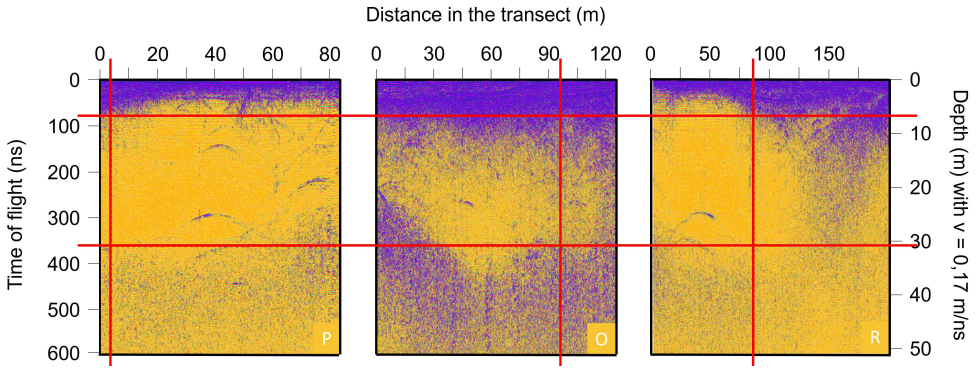

(a)

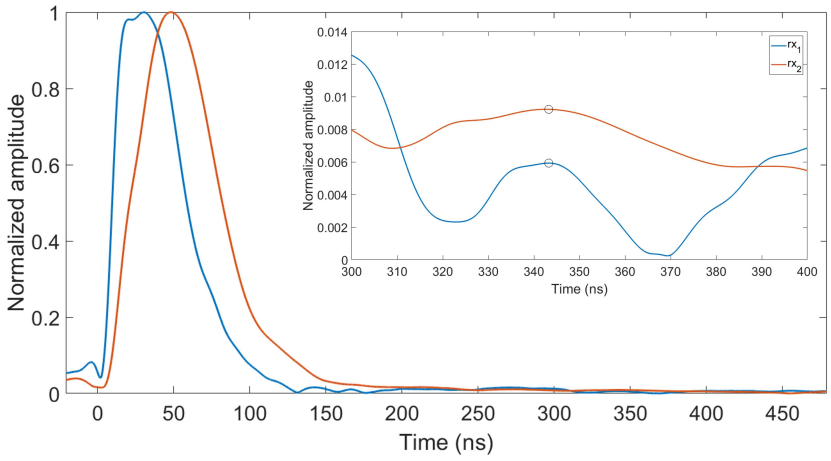

(b)

Figure 4.5: (a) GPR traces from 2019 of the three transects: the first one (P) is relative to the purple transect, the second (O) is the orange line and the third (R) is the red line; (b) Snowave radar traces for $s_1 = 0.3$ m and $s_2 = 1$ m. In the enlarged view, the peaks relative to the bedrock are shown. This plot represents the radar traces as collected by the receivers. No correction factors for the distance are applied here, as happens for normal GPR instead. For these geometries, it is important to highlight that the first peaks (before 100 ns) are relative to the interface between the firn and the ice and it is normal that most of the power returns back from there. Therefore, the actual peaks to investigate needs to be carefully detected by zooming the plot.

a percentage of LWC of approximately 0.38%. The presence of a little amount of water within the glacier raises concerns about potential ice avalanches, particularly if it accumulates near the bedrock, creating a slippery surface for the ice. However, it's also possible that this water resulted from the elevated temperatures during those days, melting the surface and possibly percolating into the first meters of snow/firn.

Colle del Gigante

The second field campaign was made at the Giant glacier on the Colle del Gigante (*Col du Géant* in French, *Giant Pass* in English), one of the highest pass in Europe at 3370 m a.s.l. and it is located on the Mont Blanc massif on the border between Italy and France (Fig. 4.6a). During this campaign, three different points with three different thicknesses were investigated, as shown in Fig. 4.6b:

1. Site 1: 35 m depth
2. Site 2: 40 m depth
3. Site 3: 50 m depth

These values come from a previous investigation done with standard GPR form 2009 done by Professor Alberto Godio from the Politecnico di Torino. It has to be considered that the depth of the glacier may be reduced after so much years.
Unfortunately, during these measurements something went wrong. A mechanical problem related to the power input of the radiators occurs at the beginning of the campaign, even if it was not visible in the field. Due to this problem, the antennas were not frequency matched anymore (not completely, at least), therefore reducing the useful information detected by the receivers. Indeed, the power recorded was mainly related to the reflection in the first layers of the firn,

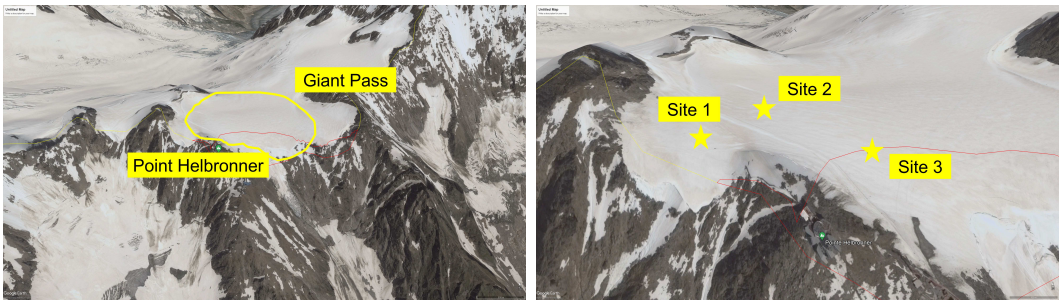

(a) (b)

Figure 4.6: Test site: (a) view of the Mont Blanc massif, in yellow is highlighted the area of the measurements, while the red line is the contended boarder between Italy and France.; (b) is an enlarged view of Colle del Gigante and the three test sites are represented with the stars.

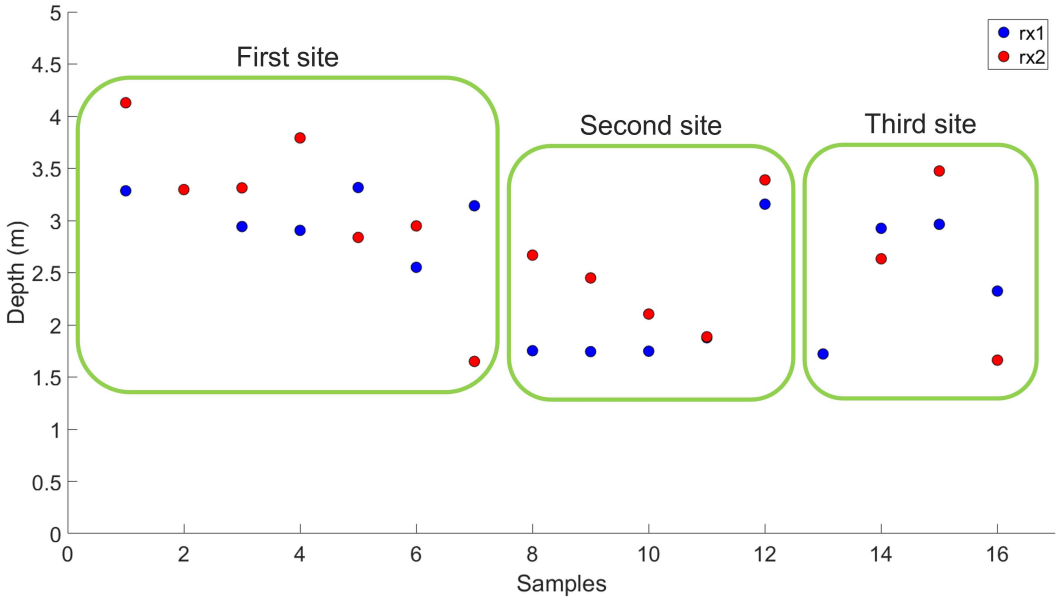

Figure 4.7: Firn investigation in Colle del Gigante using Snowave as a standard GPR. v = $1.7{\cdot}10^8$ m/s

while no important information were collected from the bedrock. Moreover, the Snowave configuration did not have success in this case. Standard GPR analysis with a single receiver was applied in this case instead, assuming the velocity of the wave into the medium as $v = 1.7 \cdot 10^8$ m/s. The highest peak in time domain are, as expected, from the first meters of snow above the glacier. In Fig. 4.7, the results relative to this investigation are shown: the blue dots are relative to the data acquired with the first receiver, while the red dots are relative to the second one. In this case, the first receiver was placed either at 0.3 m or 0.7 m, while the second was at 1, 1.5 or 2 m from the transmitter. However, the distances plotted in the graphs represent D, in the direction perpendicular to the terrain. As visible, the first site exhibits a deeper layer of snow/firn on top of the glacier, with an average value of 3.085 m. The second site, placed on a steeper area, shows an average depth of firn of 2.029 m, while it increase again up to 2.695 m in the third site, located on a lower (in altitude, with respect to the first site) and flatter area.
Other peaks in the time domain radar traces are not highlighted at this moment. Further analysis, at least with a single receiver method, will continue in order to check if information about the bedrock are presents in the data.

Chapter 5

Above the Ground Configuration

Until now, Snowave radar system has been limited by its on-the-surface deployment. This approach posed certain constraints. Firstly, the selection of monitoring sites was meticulous due to human operator presence, ensuring safety and minimizing avalanche risks. Additionally, the observations were restricted to specific points. Elevating the system at an AtG level offers a solution, enabling the monitoring of larger areas and facilitating the creation of comprehensive snow coverage maps. This elevation can be achieved through fixed platforms or mobile options like drones or small aircraft. However, this configuration introduces challenges. Surface roughness, for instance, causes back-scattering deviation, influencing the received power at the receiver. This can be helpful for configuration looking at not-nadir angle, since some of the power can be re-routed toward the receiver, but it can also deviate the signal toward tilted directions for nadir-looking systems, reducing the signal returning back to the radar. In the following section, a model which takes into account the surface roughness effect will be introduced and satellite data from various sites were used as a benchmark. However, this work can also act in the opposite direction, validating the satellite data. In a subsequent section will expose tests conducted using both an UWB radar and the Snowave system in elevated configurations.

5.1 Surface Roughness

The surface of snow, apparently uniform and homogeneous, hides an extraordinary complexity. Despite being a topic rarely addressed by the scientific research community, one of the fundamental aspects is its surface roughness, which influences a wide range of phenomena, from interaction with sunlight to the absorption and scattering of electromagnetic radiations. The snow's surface is never flat, it always have a certain degree of roughness. This surface pattern can be attributed to various factors, such as wind effects erasing snow on one area and transporting and accumulating it in another one, or it can occur during the melting process [96]. As the melting begins, the height of the roughness becomes relevant and and holes and grooves are formed. This has an effect on the EM behavior, as visible in Fig. 5.1. The pictures show the different types

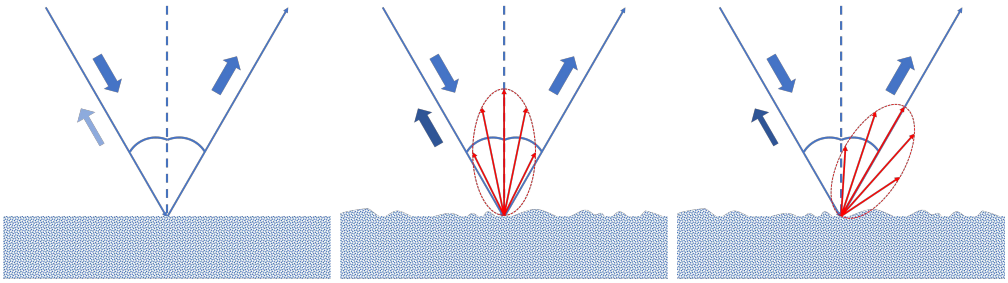

(a) (b) (c)

Figure 5.1: Effect of the surface roughness on the electromagnetic wave. (a) Mirror reflection: the energy bounces away from the sensor. This happens with smooth reflecting surface. In theory, no radiation hit the sensor, that means no data for the measurement in a monostatic configuration; (b) Isotropic reflection: relevant amount of energy is scattered toward the sensor, so we can do the measurement also in a monostatic configuration. It happens when the reflecting surface is rough. Ideally, there is the same amount of energy in every direction; (c) Mixed-behavior reflection: in the real world, we would have a mix of these two types of reflection.

of reflection which can occur when observing a surface with an EM source. If the surface is smooth, relatively to the wavelength λ of the signal used for the investigation, it will be reflected in the specular direction and minimal or no power will return back to the sensor if considering a monostatic configuration; if the surface is rough, relatively to the wavelength, the reflection will occur in different directions and a relevant part of the backscattering will return back to the emitter. The type of reflection can be determine with this fuzzy criteria: if $h < \lambda/(32 \cdot cos(\alpha))$ (Fraunhofer criteria applicable in the microwave region), where h is the height of the roughness and α is the angle of incidence of the EM wave, the surface is smooth; otherwise, it is rough. Therefore, the type of surface, and thus the type of reflection occurring, highly depend on the working frequency of the sensor, as the same surface can be either rough or smooth at the same time.

In spring, or during extended warm periods in winter, the surface of the snow rapidly changes, due to the physical and molecular transformation of the grains. The presence of liquid water may vary during this transformation, as the snowpack goes through the different melting phases (Fig. 5.2):

1. At the very beginning of the melting, the snowpack melts during the day and refreezes during the night. The grains on the surface absorb heat from the surrounding environment and start melting, creating a moist layer on the surface (LWC greater but close to 0%), digging small holes too. This phase is characterized by the snow transitioning from a solid to a slushy consistency and it is referred as "moistening phase".

2. In the second stage, called "ripening phase", the value of LWC increases

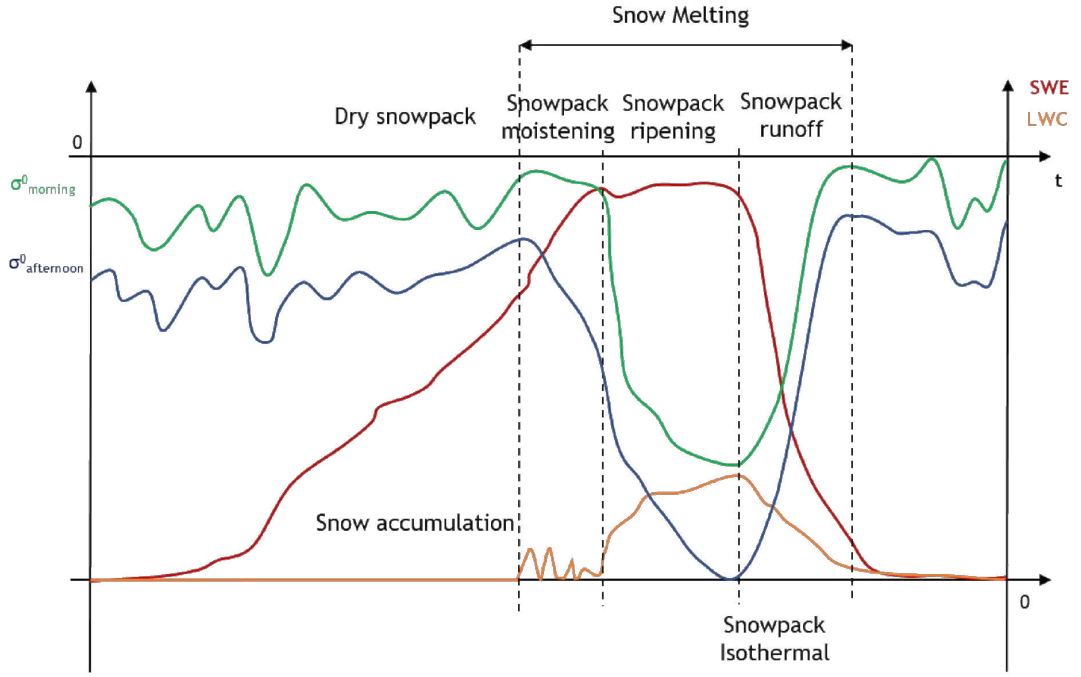

Figure 5.2: Schematic representation of the evolution of the backscattering coefficient compared with LWC and SWE evolution. The three melting phases are identified: moistening, ripening and runoff.

reaching its maximum. The snowpack becomes saturated, and the wetting front starts penetrating into the snowpack, which gradually becomes isotherm.

3. Finally, no additional liquid water can be retained by the snowpack and it is released as runoff [97]. The snowpack gets thinner until only liquid water is remained. The LWC decreases gradually as the water flows away from the snowpack.

The variations in LWC and SWE impacts the backscattering coefficient: during the moistening phase, backscattering remains high in the morning when the snowpack is still frozen from the cold night, decreasing in the afternoon after experiencing the warmest hours of the day; during the ripening phase, when the snowpack is still thick and the LWC continuously increases, the backscattering rapidly decreases, reaching its minimum at the end of this stage; During the runoff phase, backscattering starts to increase again as the snowpack loses water, becomes thinner, until it disappears. These changes in the backscattering coefficient can be used to understand the different melting phases. Experimental validations have been done using satellite data in [98], [99] and [100]. There, Sentinel-1 C-band SAR data were used to test an analytical model returning the value of the backscattering coefficient as the interaction of three different contributes: the scattering at the air-snow interface, the scattering at the snow-ground interface and the volumetric scattering inside the snowpack. Working

in C-band, the signal returning back after the interaction with dry snow ($LWC = 0$) is mainly due to the ground under the snowpack. When the snow is wet, instead, the signal is attenuated and, in some cases[1], it is note able to reach the ground. There, the superficial and volumetric scattering rules the backscattering. In the final stages, the rise in backscattering can be attributed to various factors, including a reduction in LWC, a decrease in snowpack depth, and (for satellite acquisitions with lateral geometries such as Sentinel-1) an increase in surface roughness. This phenomenon enables the snow-ground interface to once again influence the backscattering. In general, the backscattering can be characterized by its amplitude, depending on the features of the snowpack, and the direction of the various components, depending, mainly, on the surface roughness. For this reason, both contributes were used to develop a new EM model made of two different parts:

1. an analytical model which takes into account the bulky parameters of the snowpack, returning the backscattering coefficient when a microwave signal is impinging on the surface with a tilted angle;

2. a full-wave simulation which only consider the backscattering from the uneven surface.

Putting these two contributes together in a mixed model, an overall picture of the situation is found[2].

5.1.1 Analytical model

The first part of the model is related to an analytical studies which takes into account the features of the snowpack. As seen in Fig. 5.3, the snowpack is divided in a finite number of layers. Each layer has its own height, density and LWC, from which it is possible to derive ε' and ε'' using Eq. 3.6. The stratification of the medium should emulate the metamorphosis of the snowpack during the melting. On the bottom of the snowpack, the soil is represented with a semi-infinite plane with a very high dielectric constant, ideally Perfect Electric Conductor (PEC), in order to reflect all the power that reaches its surface. Indeed, the model considers a plane wave obliquely[3] impinging on the flat surface of the snowpack and propagating inside of it. Each interface creates a partial reflection of the wave in the specular direction, summed up in the value of the reflection coefficient Γ, whose perpendicular and parallel components are calculated through the following analytical equations:

[1] With the combination of thick snowpack and high LWC

[2] This work has been carried out in collaboration with Carlo Marin, a researcher at the Institute for Earth Observation - Eurac Research.

[3] A previous analytical model working with normal incidence is shown in [100].

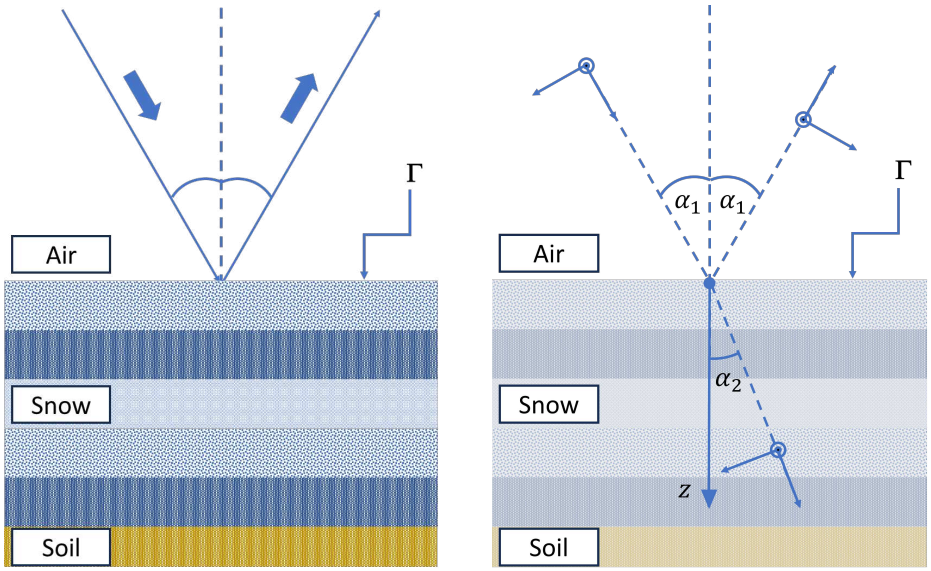

(a) (b)

Figure 5.3: Visual representation of the problems solved with the analytical method: (a) shows the situation addressed in the model, while (b) consider the transmission and reflection problem with oblique incidence.

$$\Gamma_{\perp} = \frac{a_{11}\eta_2 cos\alpha_1 - a_{12} cos\alpha_1 cos\alpha_2 + a_{21}\eta_1\eta_2 - a_{22}\eta_1 cos\alpha_2}{a_{11}\eta_2 cos\alpha_2 - a_{12} cos\alpha_1 cos\alpha_2 - a_{21}\eta_1\eta_2 + a_{22}\eta_1 cos\alpha_2}$$
$$\Gamma_{\parallel} = \frac{-a_{11}\eta_2 cos\alpha_2 - a_{12} + a_{21}\eta_1\eta_2 cos\alpha_1 cos\alpha_2 + a_{22}\eta_1 cos\alpha_1}{a_{11}\eta_2 cos\alpha_2 + a_{12} + a_{21}\eta_1\eta_2 cos\alpha_1 cos\alpha_2 + a_{22}\eta_1 cos\alpha_1} \tag{5.1}$$

In these equations, η_1 and η_2 are the characteristic impedances of the first and last medium in which the propagation occurs; α_1 and α_2 are the angles of incidence on the first interface and the angle of refraction after the last interface, respectively. $a_{i,j}$, where i, j are the subscripts[4], are the transmission parameters included in the transmission matrix, as in Eq. 5.2.

$$[\mathbf{a}] = \begin{bmatrix} a_{11} & a_{12} \\ a_{21} & a_{22} \end{bmatrix}$$

$$\begin{aligned} a_{11} &= a_{22} = cos(k_L d \cdot cos(\alpha_L)) \\ a_{12} &= -j\eta_L \frac{sin(k_L d \cdot cos(\alpha_L))}{cos(\alpha_L)} \\ a_{21} &= -\frac{j}{\eta_L} sin(kdcos(\alpha_L))cos(\alpha_L) \end{aligned} \tag{5.2}$$

[4] 1 is related to the medium emitting the EM wave, while 2 is related to the last layer where the last interaction occurs, also for the other parameters in the equation

η_L and k_L are the characteristic impedance and the wave vector of the layer L, respectively, computed in 5.3. Moreover, d is the thickness of the layer L and α_L is the transmission angle in that layer derived by the Snell's law.

$$\begin{aligned} tg\delta_L &= \frac{\varepsilon''}{\varepsilon'} \\ n_L &= \sqrt{\varepsilon' \cdot exp^{-i \cdot tg\delta_L}} \\ \eta_L &= \frac{\eta_0}{n_L} \\ k_L &= 2\pi f \cdot \sqrt{\varepsilon_0 \mu_0 \varepsilon'} \cdot exp^{-i \cdot tg\delta_L} \end{aligned} \tag{5.3}$$

where $tg\delta_L$ is the loss tangent of the layer and n_L is its refraction index. The matrices coming out from these values are computed for each layer and multiplied together in order to find the overall transmission matrix for the stratified medium (Eq. 5.4).

$$[\mathbf{a}] = [\mathbf{a}^{(1)}][\mathbf{a}^{(2)}]...[\mathbf{a}^{(N)}] \tag{5.4}$$

The expression of the parameters of this last matrix are those included in Eq. 5.1. After computing $\Gamma_{\parallel}$ and $\Gamma_{\perp}$ for some simulated snowpacks, it was noted that the results was very similar. Therefore, for the other investigations, the $\Gamma_{\parallel}$ was arbitrary chosen.

5.1.2 Full-wave simulation

The other part of the model is related to the effect of the surface roughness at the air-snow interface on the EM backscattering signal. The problem has been

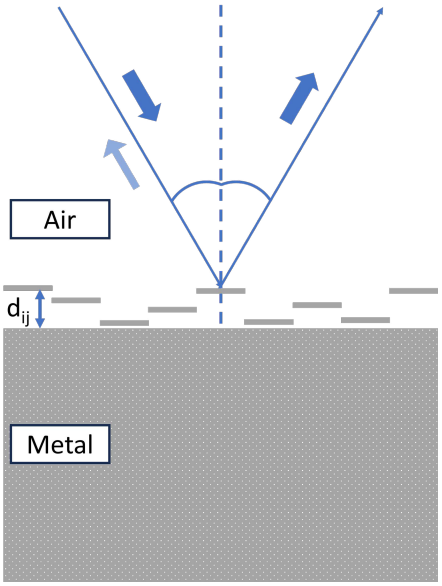

Figure 5.4: Schematic representation of the problem of the surface roughness solved with an EM simulation.

studied using a full-wave simulator environment (Ansys HFSS) and a visual representation of the model is available in Fig. 5.4. There, a 2D surface is used to replicate the rough interface between the air and the snowpack. The finite plane is made of a grid of NxM independent squared tiles with a surface of λ^2. The tiles are made of PEC and create a perfect reflective plane for the impinging wave, preventing it to penetrate underneath (this part is already computed by the first part of the model). Each tile is independent and it exhibits a random vertical displacement, different from the one of the other tiles. This is referred as d_{ij} in the picture, where i and j are the index of the tile in the grid, with $i = 1, ..., N$ and $j = 1, ..., M$, and the value of the displacement is random but limited in an interval, ruled by the root mean square (Root Mean Square (RMS)) of the height. When $d_{ij} = 0$, the surface is completely flat, and the reflection occurs only in the specular direction. As soon as the roughness appears and the displacement becomes different from 0, a portion of the reflected power is backscattered toward the monostatic direction[5]. Since the increasing value of backscattering power (monostatic direction) is really small and could be difficult to read, the decreasing of the reflected power (bistatic direction) is considered instead. Indeed, it is assumed on statistical grounds that the decrease of power in the bistatic direction is proportional to an increase of the backscattered echo along the monostatic one. For our purposes, the components along all the other directions are considered negligible. In this model, the incidence of the wave occurs with different angles, from 25° to 45° with steps of 5°, in order to take into account several configuration of real satellites. Even if some of them can operate with either lower or higher angle of view, the range of the model was limited by the computational time, but still considering most of the practical cases. Three different frequency are considered, relative to the operating bands of three satellites using for snow observation:

- 1.2 GHz as for SAOCOM (SAtélite Argentino de Observación COn Microondas), which uses a polarimetric L-band SAR with an observation angle between 18°and 50°. It serves for Earth Observation (EO) and for disaster monitoring;

- 5 GHz as for Sentienel-1, whose SAR is working in C-band, looking at the Earth surface with angles between 20°and 46°. It provides data at high and medium resolutions for land, coastal zones and ice observations;

- 9.6 GHz as for COSMO-SkyMed, equipped with a SAR in X-band, with an incidence angle of 20°to 60°. It is used for EO, both civil and military.

The full-wave simulations were done for each frequency and viewing angle. Moreover, for each simulation, the height of the surface roughness changes within different ranges. This surface roughness was introduced as a random variable, and a statistical analysis were done. The RCS in the specular direction was

[5]It is supposed that in the case of flat target, the reflection occurs in the bistatic direction only.

detected, taking into account the random variation of the surface. For each frequency and incidence angle, a curve of RCS was found, depending on the value of RMS. It has been noticed that these curves act linearly up to a certain value of RMS, and therefore the linear equations have been found. In Fig. 5.5, these lines are represented for each band and angle. On the background, also the linear range of application is highlighted. These lines represent the linear behavior of the bistatic RCS depending on the type of surface roughness expressed in terms of RMS. It is worth noting that the surface roughness has more effect on higher RMS, but also on higher frequency. Once the equations relative to the linear curves of bistatic RCS are found, and knowing the value of RMS to analyze, the computed value is normalized and then the inverse is done in order to find the monostatic component.
For example, for a frequency of 1.2 GHz and a incidence angle of 25°, the linear equation is related to the blue line in the first plot in Fig. 5.5. Including the value of RMS, in this example equals to 10 mm, the effect of the surface roughness on the bistatic RCS is found. After normalizing this value on the entire dataset, the inverse of this value is taken (i.e. the monostatic direction is considered). This value, is then multiplied to the percentage of reflected power computed with the first part of the model, in order to retrieve the total power backscattered in the monostatic direction. The complete model, after merging together the analytical study and the effect of the surface roughness, is called *mixed model*.

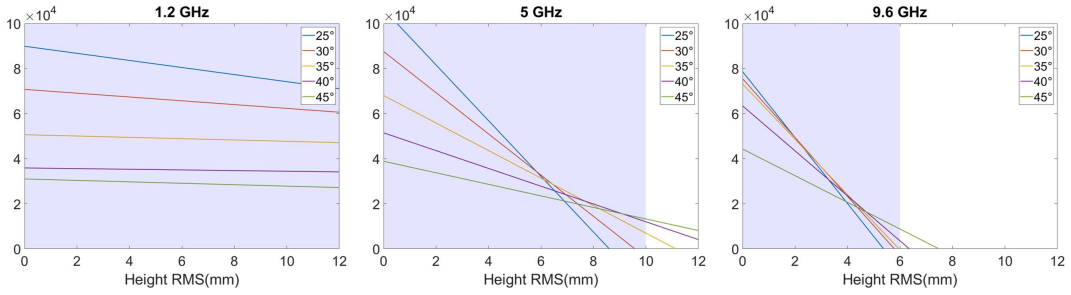

(a) (b) (c)

Figure 5.5: Linearization of the snow surface roughness effects for different frequencies and rms. The y-axis value is expressed in arbitrary unit.

5.1.3 Model validation on synthetic and real snowpacks

Several snowpacks, real or simulated, have been analyzed with this method. Here are presented the results relative to three real test sites:

- Malga Fadner (MF), South Tyrol, Italy;
- Torgnon (IT-Tor), Valle d'Aosta, Italy;
- Weissfluhjoch (WFJ), Graubünden, in Switzerland.

For all the sites, the observed data, taken from different manual or automatic weather stations, were used to feed a physically based one-dimensional model called SNOWPACK. SNOWPACK is developed by the WSL-SLF and takes into account several physical, thermal and mechanical inputs in order to perfectly simulate a real snowpack [101][102]. These data comprise the parameters needed for the first part of the mixed model, i.e. the snow depth, the density and the LWC. The height of the surface roughness is derivable too, and it used for the second part of the model. The model outputs are then compared with satellite data. Data from Sentinel-1 was utilized for the three sites. It is important to highlight that the absolute value of the backscattering is not considered in this work. The aim, indeed, is just to model the behavior of the backscattering through the melting season, and not to have an absolute value, which would take into account several other parameters.

Malga Fadner (MF)

Fig. 5.6 represents the ground truth relative to the time period between October 2017 and October 2018 with a sampling time of one day. The depth of the snow increases for the entire winter period and new snowfalls are detectable. The metamorphosis and compactation of the snowpack shows its evidence in the value of the density, which increases almost monotonically during the entire season. At the end of April, the snowpack starts to decrease in height, probably in agreement with an increasing trend of temperatures. This is proved by the presence of LWC and a strong increasing of the density. This trend continues until the complete vanishing of the snowpack. In local points, e.g. at the beginning of the snow season and at the end of the summer, the snow depth and the LWC increase for only some days, probably due to isolated snowfalls, before returning in a no-snow condition.

The first part of the model was fed with the equivalent 1-layer ground truth data depicted in the figure below. After following the procedure described in a previous section, the percentage of reflected power for different angles of incidence is computed and it is visible in the graphs in Fig. 5.7. Investigations in the three frequency bands were done, even if the only available satellite dataset was in C-band. In the L-band, with a central frequency of 1.2 GHz, the reflected power accurately models the behavior of the snowpack. The melting process is clearly visible and, even with large amount of water, the signal still returns back after the propagation. Even the local snowfalls are detected. In the C-band, with a central frequency of 5 GHz, the attenuation of the water strongly affects the EM signal. Indeed, as soon as the LWC becomes greater than 0, the signal reflected power decreases down to values close to 0. Still the beginning of the melting season is detectable, and some supposition about the phase can be done. In the X-band (9.6 GHz of central frequency), the situation is even worse. A little amount of LWC kills the signal, and the following melting phases are difficult to highlight.
The second part of the model takes into account also the surface roughness,

statistically expressed as the RMS of the entire surface, calculated through the SNOWPACK model with the aid of the ground observed data. In this case, the surface roughness has been computed only for the restricted period during the melting season, i.e. from march to may, and it is represented by the monotonic green curve in Fig. 5.8. Once the contribute of the surface roughness is computed, it is combined with the analytical model results. Finally, only the desired frequency and incident angle outputs are taken into account, in order to have a precise comparison with the satellite data. Indeed, the SAR mounted on that satellite works in C-band, and the orbit used for the comparison has a viewing angle of 46°. The comparison is depicted in Fig. 5.8. The backscattering from satellite is well followed by the one of the analytical model. Even if the analysis of the bulky parameters is sufficient to model the backscattering for most of the time period, there are some points where the surface roughness helps to explain small differences. For example, at the beginning of April, when the melting starts, there's a gain of backscattering due to the initial presence of LWC. Then, before reaching the snowpack saturation, the satellite records a smoother rise of the backscattering with respect to the analytical signal. With the presence of the surface roughness, the normalized trend follows the satellite data. Therefore, modeling the backscattering behavior of a snow covered land is needed to detect the beginning of the melting phase and to identify its different phases.

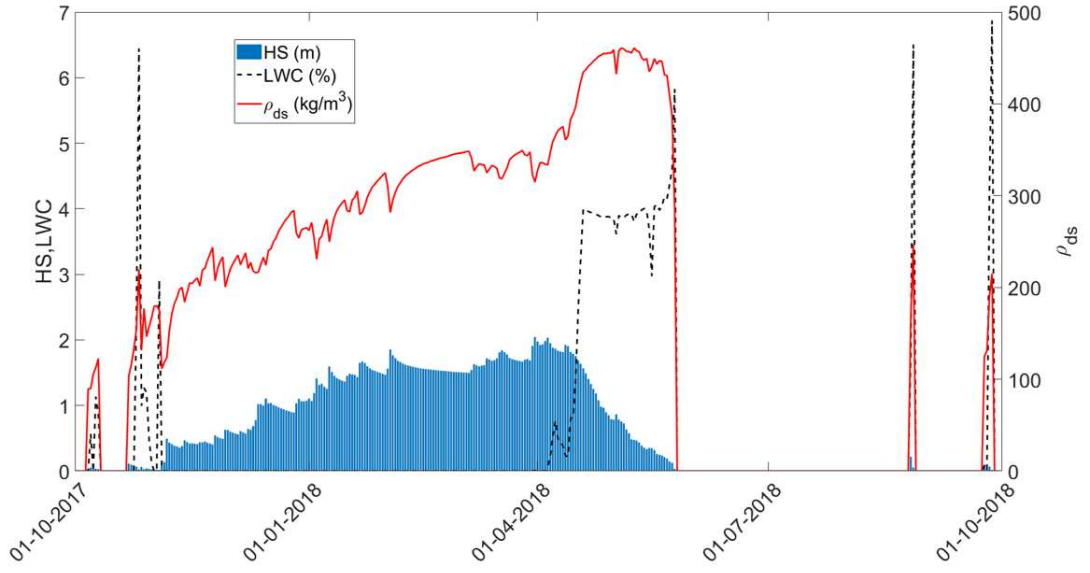

Figure 5.6: MF - ground truth data, snow season 2017/2018.

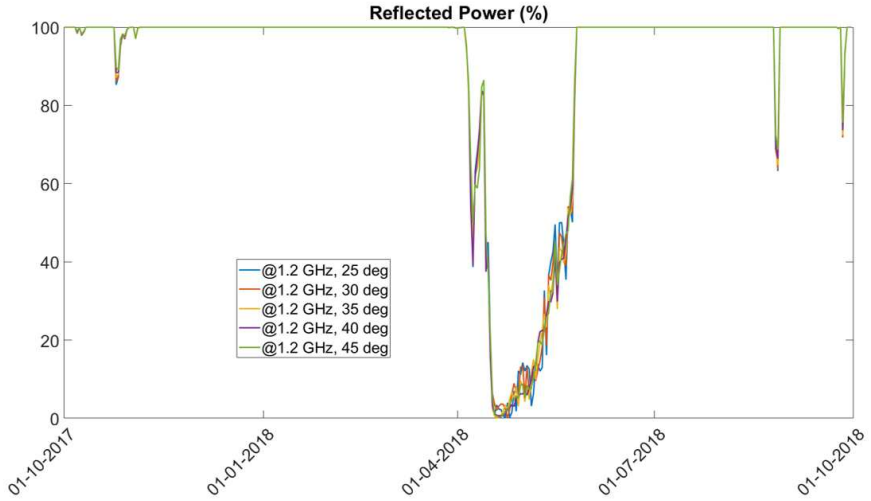

(a)

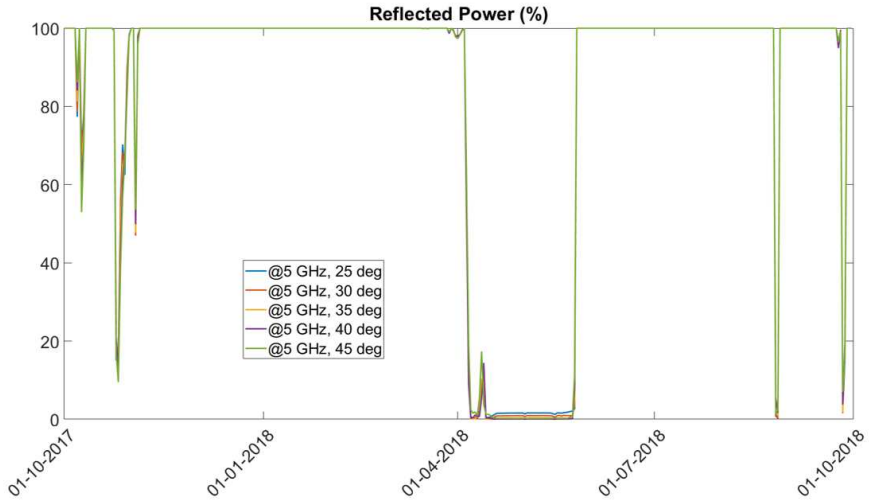

(b)

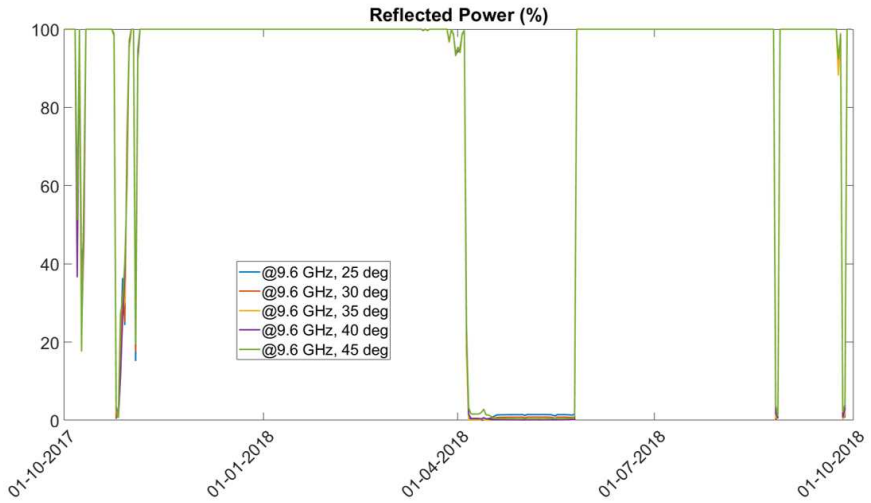

(c)

Figure 5.7: MF - output of the first part of the model. Reflected power in percentage for different incident angles in (a) L band, (b) C band and (c) X band.

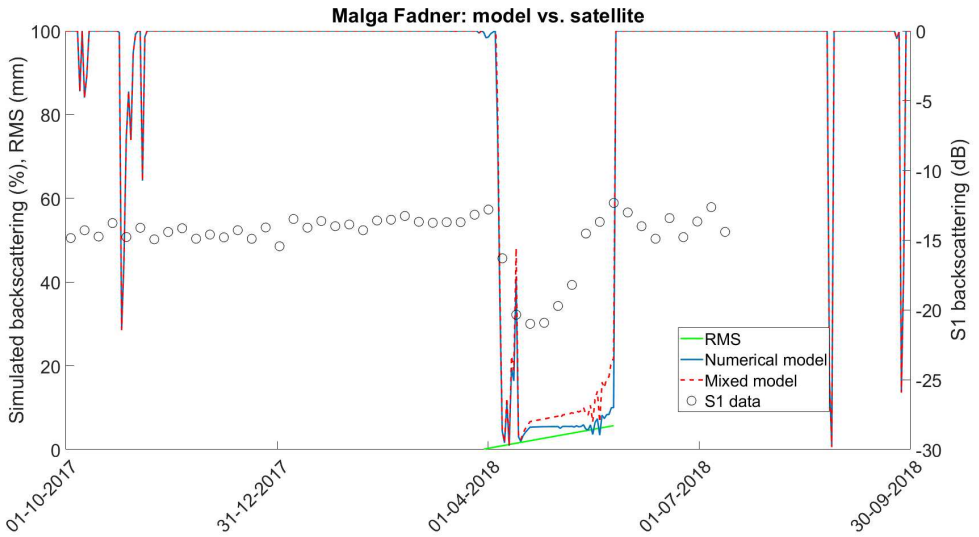

Figure 5.8: MF - comparison between the mixed model and the satellite backscattering data.

Torgnon (IT-Tor)

The second set of data is relative to IT-Tor site, located in Valle d'Aosta (IT) at 2160 m above sea level (45°50'39"N, 7°34'41"E). The site is equipped with a meteorological station with hourly observations of air temperature, snow surface temperature, relative humidity, precipitation, snow depth, incoming and outgoing longwave and shortwave radiation, wind velocity and direction, ground surface temperature and SWE. These data are used as inputs for the SNOWPACK model, retrieving information on depth, density and LWC. In this case, SNOWPACK model was fed with a large amount of observed data (2016 - 2021), and returns snow features divided into three different layers. However, the data relative to the snow surface roughness considers only the spring season 2018. The ground truth data outside this period, which are not import for the mixed-model analysis, are not displayed. The overall trend of the ground truth from 30/03 to 27/05 can be seen in Fig. 5.9. This time period coincides with the melting, from the beginning of the moistening, when the LWC is only few percentage points, to the end where the thickness of the snowpack is minimum.
In the representations of the outputs of the analytical model (Fig. 5.10), it's clearly visible that the attenuation is not so effective on the L band, with respect to the other two bands considered. However, to validate the model against real satellite data, the C-band needs to be considered (S1), with an incident angle of 35°, approximately.
The comparison between the model outputs and the satellite data are depicted in Fig. 5.11. The RMS is represented too. Unfortunately, since the time period is restricted, the quantity of available satellite data was scarce. Nevertheless, a general good agreement between the modeled backscattering and the one recorded by the satellite can be appreciate, especially at the beginning and at the end of the melting season. By looking at the graph, it can also be appreciated that the small variations in RMS are well followed by the red curve. Moreover, these local rising of the signal are confirmed by the points in the satellite trace, which exhibits an higher backscattering in correspondence of those peaks. In order to sense the transition between the phases, more data should have been considered.

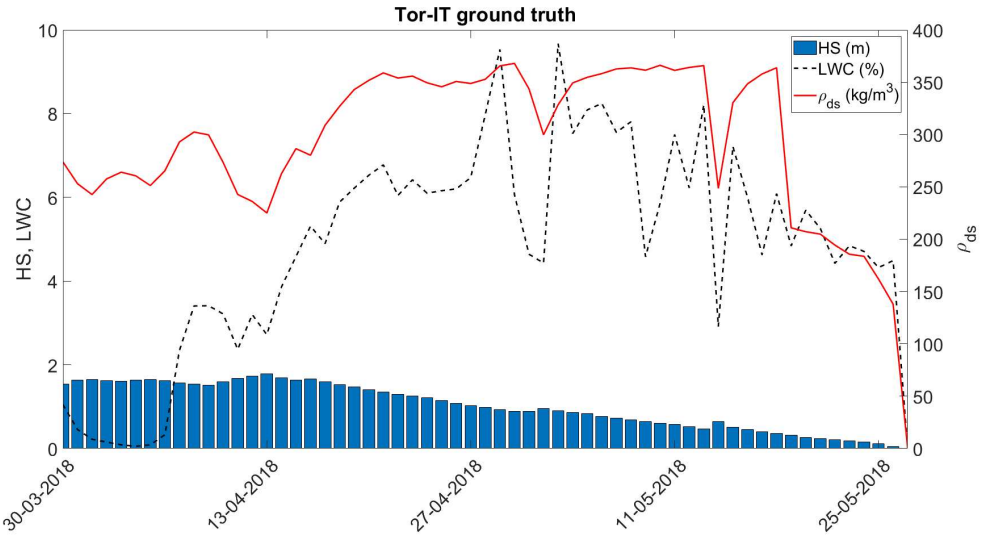

Figure 5.9: IT-Tor - Ground truth data, spring season 2018.

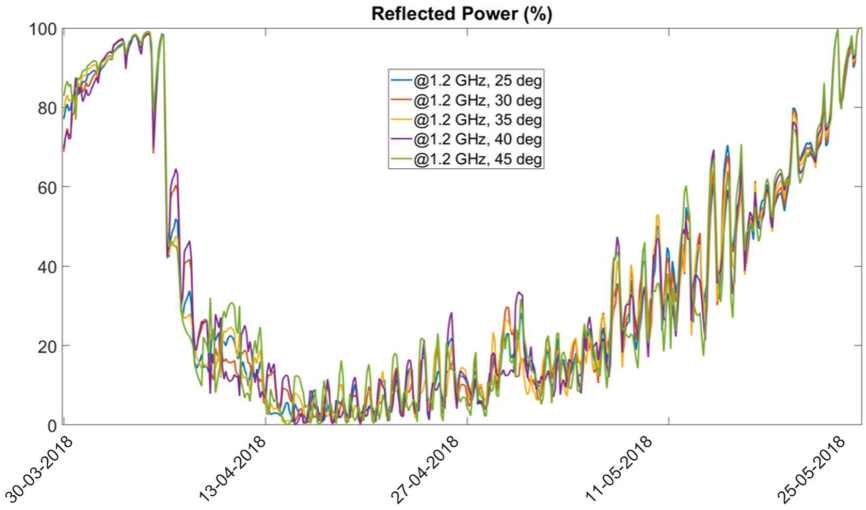

(a)

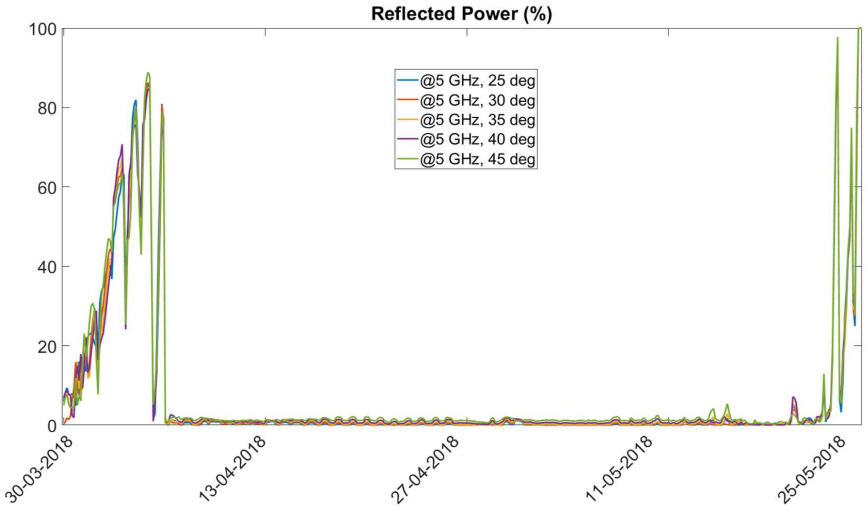

(b)

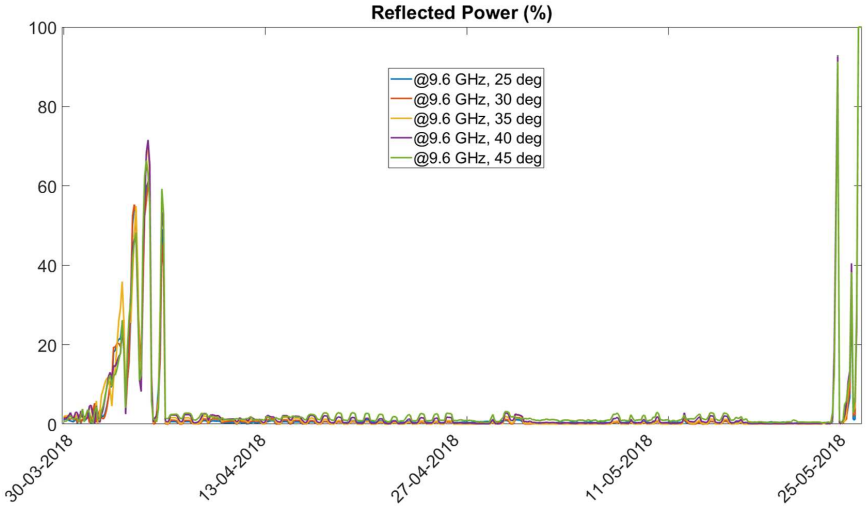

(c)

Figure 5.10: IT-Tor - output of the first part of the model. Reflected power in percentage for different incident angles in (a) L band, (b) C band and (c) X band.

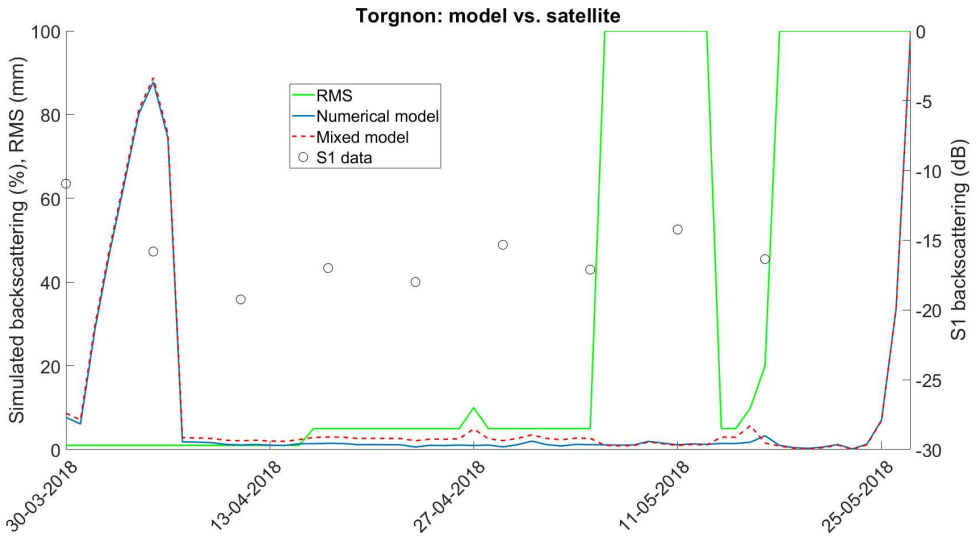

Figure 5.11: IT-Tor - comparison between the mixed model and the satellite backscattering data.

Weissfluhjoch (WFJ)

The site WFJ (46°49'47"N, 9°48'33"E) is located in Switzerland, close to Davos, at an altitude of 2536 m above sea level, and it operated by the WSL and SLF. Numerous sensors are present to record meteorological data and snow properties with a sampling time of one hour. The period of observation lasts from the first of October, 2021 to the first of October, 2022. The high altitude site of WFJ allows to identify the presence of snow for a longer period, with respect to the other sites. The huge amount of observations can identify changes in LWC and density even within the same day. For this reason, the graph 5.12 below showing the ground truth is very populated. LWC starts to be present at the beginning of March 2022, with probably melting-refreeze cycles occurring up to the end of March. After a short period of no-LWC, it increases again starting the real melting season. Even the density follows the same pattern.
For what concern the first part of the model, all the considered frequencies well identify the melting-refreezing cycle of March 2022, expressing the same trend with different sensibility to the attenuation of water, which never exceed the 6%. With higher values of LWC, instead, the C and X bands were unable to detect the small changes. Local snowfalls in September 2022 were detected as well.
The satellite used for the comparison is always S1, working in C band with an incident angle of 30°, approximately (Fig. 5.14). The backscattering agreed most of the time, even for small changes. However, in this case, the surface roughness contribute is not sufficient to clearly identify the melting phases of the snowpack. This can be probably due to the percentage of the backscattering as a result of the first part of the model: indeed, with respect to the other cases, the snowpack was deeper, more dense and more wet, which concurred to decrease the percentage of reflected power, as it was almost completely attenuated inside the snowpack. Therefore, even with high value of surface roughness, the multiplication between this and the reflected power would have been ineffective. This is proved also by the satellite signature, which has its minimum value around -25 dB and an average of $\sim$ -19 dB, lower with respect to the other cases, where the minimum value is roughly -21 dB and the average $\sim$ -12 dB.

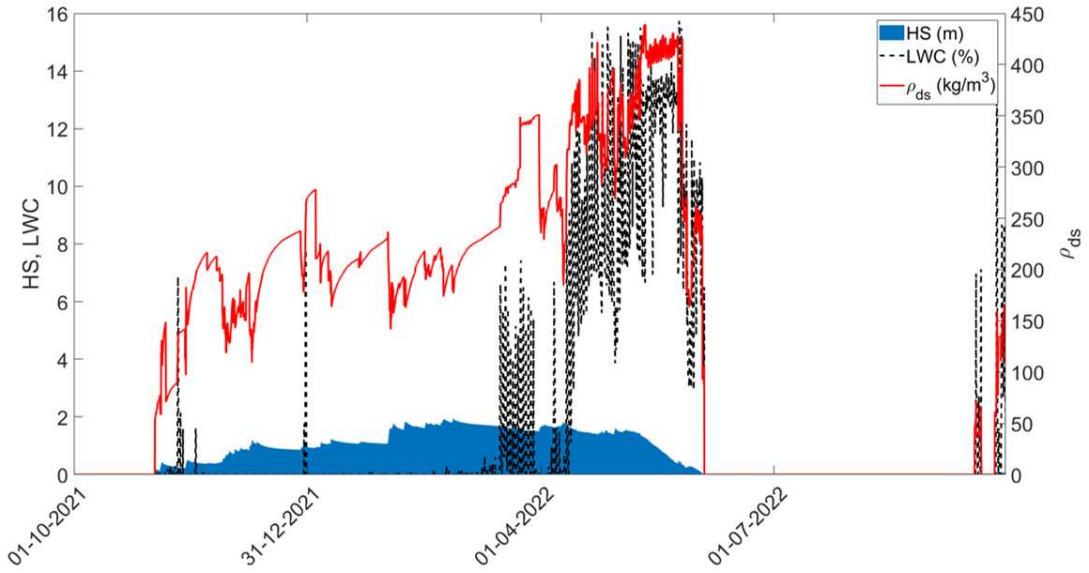

Figure 5.12: WFJ - ground truth data, 2021-2022.

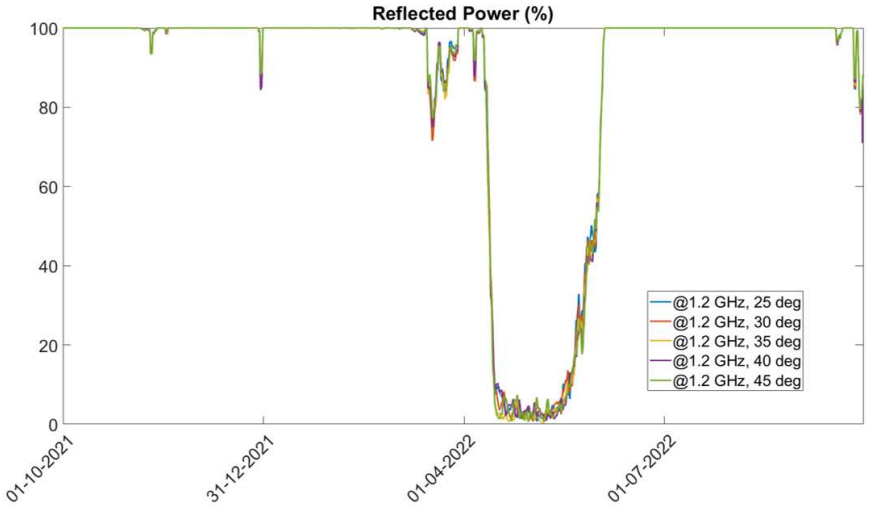

(a)

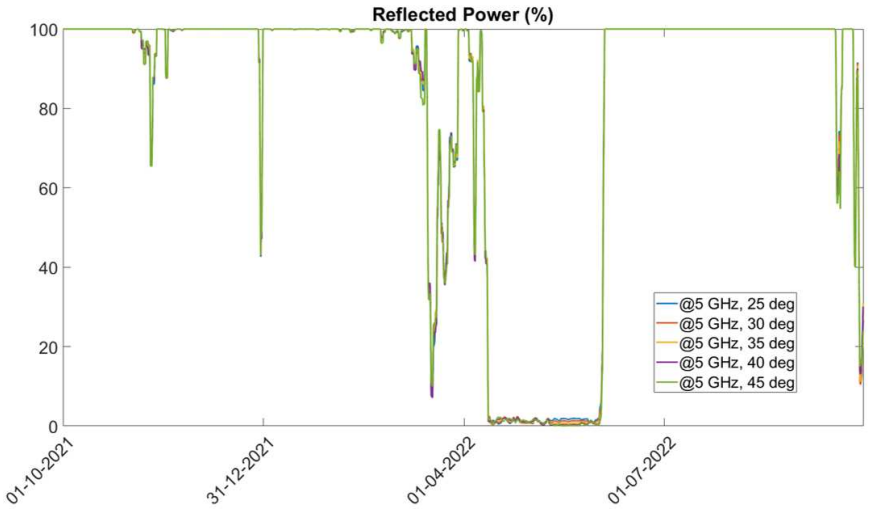

(b)

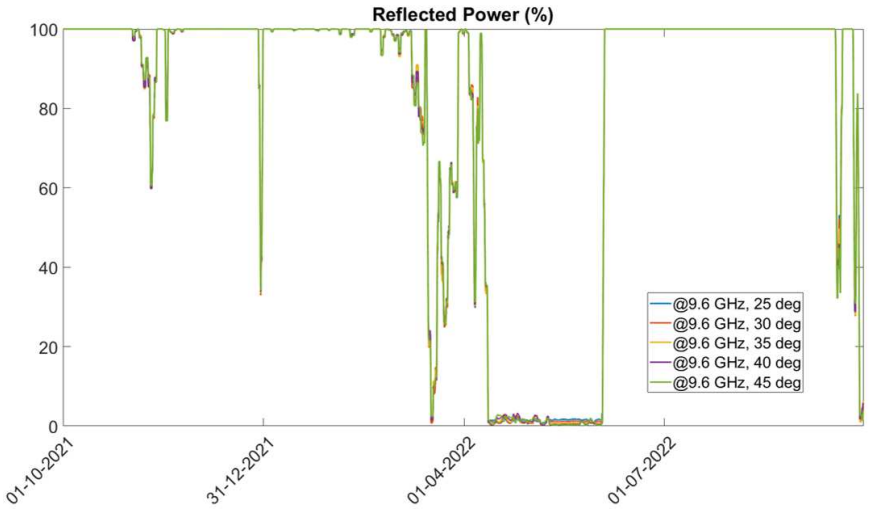

(c)

Figure 5.13: WFJ - output of the first part of the model. Reflected power in percentage for different incident angles in (a) L band, (b) C band and (c) X band.

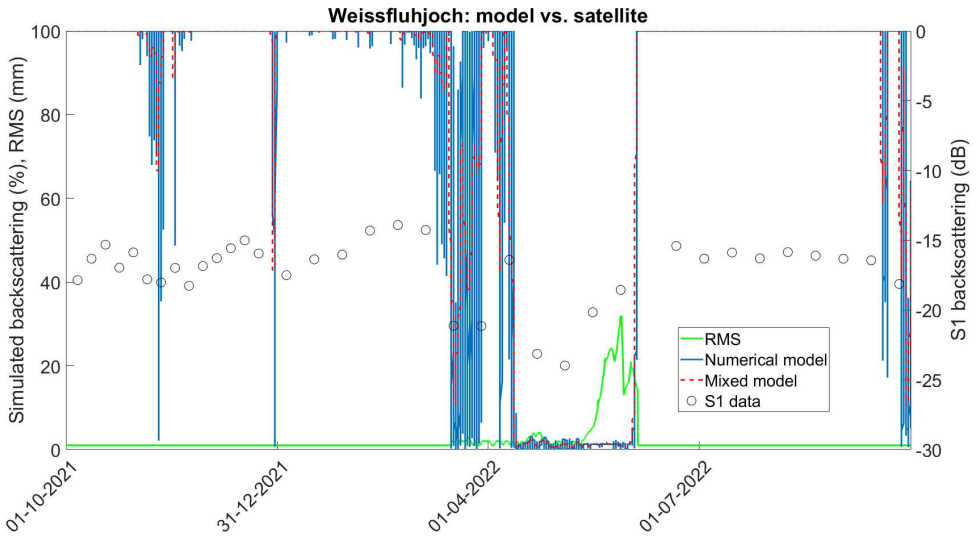

Figure 5.14: WFJ - comparison between the mixed model and the satellite backscattering data.

5.2 Ultra Wide Band Radar

In order to apply the AtG configuration, some laboratory and outdoor tests have been conducted with a commercial radar thanks to the collaboration with the nanoelectronic group of the University of Oslo[6]. These tests were made using a XeThru X4 low-power UWB radar SoC by Novelda, equipped with a X4M03 development kit, in order to access all the functionalities of the radar. The radar works with a central frequency in C or X band (7.29 GHz or 8.748 GHz, respectively) and the BW ot the transmitter can reach a value up to 1.5 GHz. This radar has been originally designed for human presence sensors, being able to detect all kind of movements in a room, either major or minor, but it can be applied to other fields. Indeed, it has been used for snow monitoring purposes in the past [103]–[107]. This radar was tested in an AtG configuration both indoor and outdoor. For the indoor test, two venues have been considered: a first test was done in a normal laboratory, without any controlled situation for what concern the external stimulus; instead, the second test was made in an anechoic chamber, in order to understand if the presence of the environment can affect the

[6]The work done at the University of Oslo was in the framework of the Erasmus+ Traineeship program.

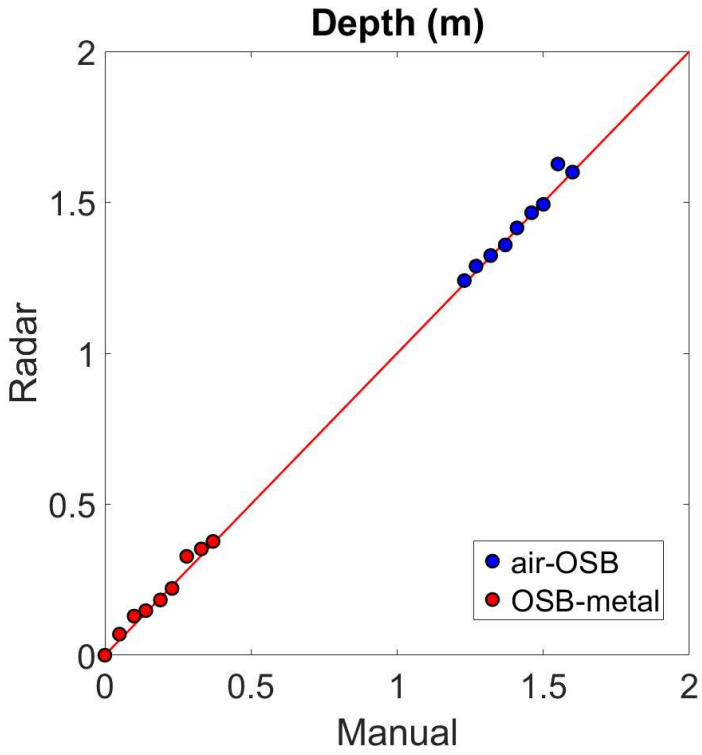

Figure 5.15: Results of the indoor test in a uncontrolled environment, ground truth compared with radar measurements. The blue dots refer to the interface between the air and the OSB panels, while the red dots refer to the interface between the OSB panels and the metal plane on the bottom.

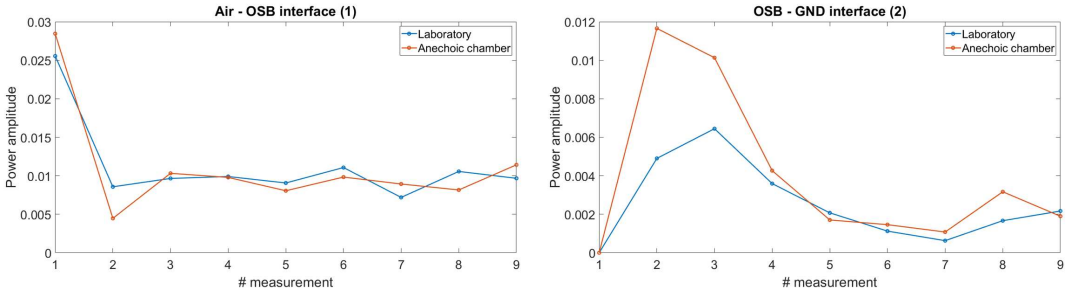

(a) (b)

Figure 5.16: Comparison of the amplitude of the signals during the measurements in laboratory and in the anechoic chamber.

measurements. To do the measures indoor, simulating the natural environment, Oriented Strand Board (OSB) panels were used. OSB, a type of engineered wood similar to particle board, closely resembles the electrical properties of wet snow, making it an excellent phantom material for indoor experiments, given its real dielectric constant ε' close to 2. However, this panels are not able to mimic the imaginary part. Each OSB panel has a thickness of approximately 1.5 mm, allowing the panels to be stacked creating different thicknesses of the phantom. Various thicknesses were tested in the laboratory using the UWB radar, and the results aligned well with the manual measurements, as shown in Fig. 5.15. The outcomes were generally realistic and precise, except for a minor inaccuracies. In some cases, the OSB layer was too thin to be distinguished from the ground, causing the responses of the two interfaces merged in the radar trace, making it challenging to differentiate the two peaks.

After confirming the radar's ability to detect two different interfaces within

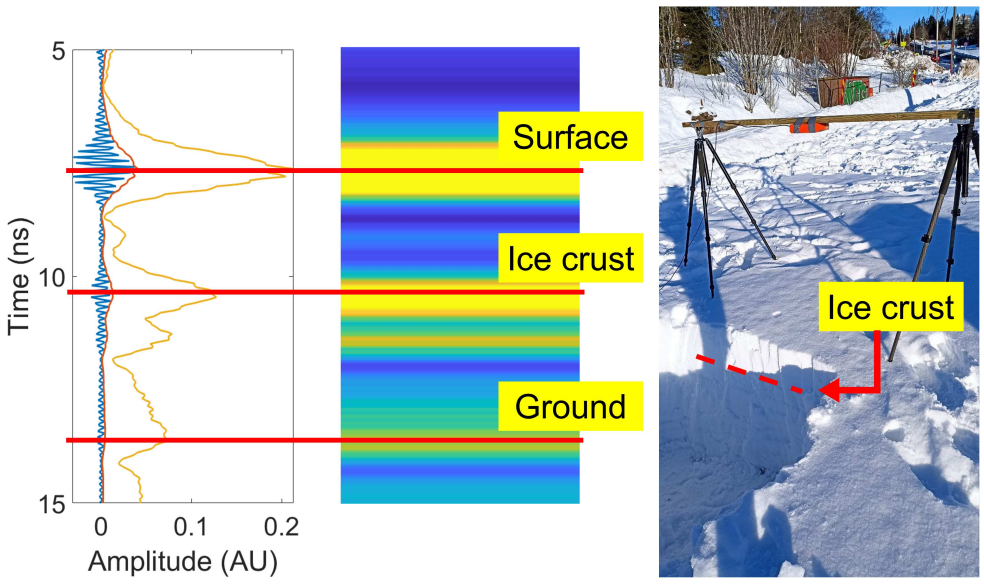

Figure 5.17: AtG configuration and results.

a medium, it was also tested in the anechoic chamber. This test was crucial to assess the environmental impact. If the environment significantly affected the power budget, measurements in real-world conditions, especially with wet snow, might be challenging. The power budget comparison results for both the air-OSB and OSB-GrouND (GND) interfaces are presented in Fig. 5.15. Clearly, the environment does not impact the measurements. Hence, the analysis outdoors can proceed without concerns about a possible power limitation.
The outdoor test took place in Tryvann (59°59'16"N, 10°39'58"E), a ski resort in Oslo, Norway in January 2023. The snowpack was completely dry with a thickness of roughly 90 cm. It shows a frozen layer 40 cm below the surface, as seen from Fig. 5.17. The radar was placed in an AtG configuration thanks to two tripods and a wood stick, and connected to a laptop to control the data acquisition. The acquisition was done looking at nadir. The results show the capability of the radar to identify not only the two interfaces of the snow surface and of the ground, but also the ice layer, roughly in between the other two peaks.

Chapter 6

Conclusions

In this chapter, a conclusive discussion about the results obtained in the previous sections is presented, highlighting the utility of this work in overcoming the limitations of other state-of-the-art instruments. The discussion then moves to the challenges that had to be faced during the study.

6.1 Summary and discussion

In this thesis, some methods and attempts to monitor different parts of the cryosphere have been discussed. In order to overcome and prevent problems related to hydrology, climate change, ski tourism and safety, it is important to have constantly monitored situation of the area to be considered, which could be a particular spot, a mountainside, a basin, or an entire region. The instruments employed nowadays are very powerful and of use all kind of technologies. In particular, radars are largely used for either satellite, aerial or terrestrial surveys and, among them, GPRs are the best solution. Indeed, GPRs retrieve values of depth and dielectric constant, which are used to represent snow and ice. These two parameters cannot be directly computed from GPR traces without using external instruments, hypothetical assumptions or complicated techniques, as the those results suffer of a strong ambiguity due to the architectural concept of the system. In order to solve this ambiguity and be independent from other sources, Snowave was introduces in previous works. Snowave is a dual-receiver radar architecture able to compute the depth and the dielectric constant of a medium, solving the ambiguity of a standard single-receiver radar and increasing the accuracy of the results. The parameters derived from the radar acquisitions, which exhaustively describe the medium, such as density, SWE and LWC, acquire a more precision too. Different medium have been observed during this work, and each of them requires an EM consideration relative to the frequency band to use to successfully acquire data. In particular, the observed environment are: i) dry snow ii) wet snow iii) glaciers.
For what concern dry snow, it is described as a medium with a relatively low density, between 30 kg/m^3 and 450 kg/m^3, thanks to its porosity. These values are directly linked to the real part of the dielectric constant ε', which can assumes

values between 1.05 and 1.82. No water in liquid form is present at this stage. In this condition, the snow can be modeled as a lossless dielectric medium (like the air), letting the microwave signal penetrate inside the medium. In this case, the frequency bands used for the investigations were the S, the C and the X. Several measurements campaign have been carried out to validate the architecture with this multispectral setup in the Italian Alps. Indeed, in the winter seasons 2021/2022 and 2022/2023, four different sites have been visited: Torgnon, Cheneil, Lazaun and Cime Bianche. Different bands were able to identify slightly different values of depth, density and SWE: the higher frequencies, thanks to their shorter wavelength, gain in accuracy and the results show smaller errors. In general, for all the sites, the snow depth was well identified with a high accuracy (more than 95% in every case) and the fluctuation of the results of each measurement was minimal. The density and the SWE show higher standard deviation, even due to the non linear computation used to calculate them. Nevertheless, the mean values of the results were, in every case, in good agreement with the manual analysis, showing an accuracy of 89% and 90%, respectively.
The following part of this work was focused on the monitoring of wet snow, which shows a more complicate physical and electromagnetic behavior, due to the presence of liquid water in it. Liquid water, indeed, has the strength to attenuate the signal based on the frequency used. In this case, not all the antennas were suitable for the measurements, and it was mandatory to carefully choose the correct range in order to have a trade-off between the resolution of the system and the attenuation of the signal. X band was not used in this case, while C band was used in some transitional phase (not too dry, not too wet). During the spring seasons of 2022 and 2023, despite the absence of significant snowfall and unusually high temperatures, some measurement campaigns were conducted to study this conditions: Lazaun, Gran San Bernardo, Riale and Gran San Bernardo (after one year). Additionally, in April 2023, a non Alpine site was visited. The Arctic site of Sodankylä host a 15-days campaign in order to evaluate the performance of Snowave during an entire melting cycle. In each campaign, Snowave and manual analysis were done. The analysis of the collected radar traces returns values of snow depth, and LWC in agreement with what measured with the manual analysis. The precision of these measurements can be well evaluate for what concern the snow depth, directly relatable to the in-field measurements done with a snow probe, while the LWC, the density and the other parameters cannot be precisely compared to the ground truth, since also the manual analysis and other instruments, like the Snow Sensor by SLF, are not precise. Fortunately, the climatic context of each measurement sufficiently describe the possible status of the snowpack. Each campaign shows an agreement with the manual analysis, either for instantaneous monitoring and for detecting the different LWC during the melting process. For what concern the polar campaign, the trend of the results follows the in-field manual measurements, and even the small differences are well justified. In general, the precision is not very high, but there is still to figure out how to carefully choose the perfect working frequency case by case.
Another new topic introduced in this thesis is glacier monitoring. Snowave was

employed in this context for the first time with a new setup. Glaciers are very deep bodies and reaching the bedrock can be challenging. Indeed, low frequency devices need to be employed. For this reason, custom-made antennas, inspired by the structure of the PIFA antennas, have been designed, simulated, produced and tested. Once checked the ability of these antennas to penetrate first firn and then ice, reaching distant bedrocks, the complete system has been tested in a field campaign. This first campaign demonstrated the great ability of the system to understand the glacier features. Indeed, the traces collected by the radar showed a very high peak at the beginning which can be related to a strong reflection from the firn and the ice of the glacier. Then, the magnitude of the signal rapidly decreased. However, it was possible to extract other peaks and to identify the reflection from the bedrock. The resulting depth was in good agreement with older data collected by a GPR. However, small differences in the two results were identified, possibly due to two factors: i) GPRs are based on the assumption of the velocity of the wave into the medium, while Snowave directly calculates it, taking into account how the medium itself is composed; ii) the climatic changes of the latest years bring the glacier to a faster melting, losing part of its mass. The value of the retrieved dielectric constant, instead, rise the doubt about a possible water content. Indeed, the higher values (with respect to the normal range for glaciers) can be justified by the presence of water along the vertical profile investigated. This can lead to very dangerous situations, not good for the glacier itself and for the environment around. In recent times, other observations by local agencies highlight the same problem, confirming what the radar already observed. However, this preliminary observations need to be certified by more exhaustive studies.

The last part of this thesis is focused on the modelization of the melting process in order to detect the different phases through the backscattering signal collected from above the ground radar sensors. The model developed can help to predict the behavior of the snow, and it is built upon two different parts: i) a first-order numerical simulation based on plane-wave oblique incidence on stratified media which takes into account the bulky physical parameters of the snowpack returning the reflection coefficient Γ at the air-snow interface in the specular direction; ii) a full-wave simulation to include the effect of the surface roughness on the oblique impinging wave. Once the two contributions are determined, they are summed up to derive the overall effect related to the mono-static backscattering for oblique incidence. To validate the model, it was tested against experimental data from different Alpine sites (Malga Fadner, Torgnon and Weissfluhjoch), where data from the satellite Sentinel-1, as well as in-situ data about the composition of the snowpack, were available for the winter season 2017/18. All these tests returns reasonable results, showing a good agreement with what expected and with respect to the real data from Sentinel-1.

6.2 Future developments

The research done in this thesis was an enhancement of an already existent radar system for snowpack monitoring. With this work, different new aspects have been considered and tested, discovering new potential applications. However, there are some open questions which needs to be taken into account in order to further improve the system.
First of all, the multispectral setup may be simplified, introducing new UWB or reconfigurable antennas. While working in harsh and cold environment, performing operations such as switching antennas and connectors is challenging and it can lead to errors or lack of accuracy, while wasting time. Using only one type of radiators, instead, can simplify the operations to do in the field when a change in the frequency is needed. Moreover, since the system is portable, having only one set of antennas reduces space and weight, making possible to reach remote places without bringing bulky equipment. In this direction, having a dedicated board for the signal manipulation can further help, avoiding the use of the VNA, big and heavy. A well-defined software and a front-end interface would further increase the usability, in order to let any operator to use it.
A few things needs to be clarified, especially for what concern wet snow and glaciers. Other campaigns or indoor tests would help to describe the electrical behavior of those bodies, which in turn can help to tune the setup.
All these operations can lead to a complete system, ready to work without any kind of previous expertise. Once the system is completed, it can also be mounted on board of UAV, in order to increase the sensed area, and return precise parameters, usable in different sectors.

Bibliography

[1] T. Geldsetzer and J. B. Jamieson, "Estimating dry snow density from grain form and hand hardness," in *Proceedings of the 2000 International Snow Science Workshop (ISSW), October 1-6, Big Sky, Montana, USA*, 2020, pp. 121–127.

[2] F. Monti and J. Schweizer, "Deriving snow hardness from density and its application to the 1-d snow cover model snowpack," in *European Geosciences Union (EGU), Vienna, Austria, 22-27 April 2012.*, 2012.

[3] P. F. Espín-López and M. Pasian, "Determination of snow water equivalent for dry snowpacks using the multipath propagation of ground-based radars," *IEEE Geoscience and Remote Sensing Letters*, vol. 18, no. 2, pp. 276–280, 2021. DOI: 10.1109/LGRS.2020.2974546.

[4] M. Pasian, P. F. Espín-López, L. Silvestri, M. Barbolini, and F. Dell'Acqua, "Experimental validation of a dual-receiver radar architecture for snowpack monitoring," *International Journal of Microwave and Wireless Technologies*, vol. 12, no. 6, pp. 439–446, 2020. DOI: 10.1017/S1759078720000112.

[5] M. Lodigiani, L. Silvestri, R. Barella, *et al.*, "Multi-spectral analysis of dry alpine seasonal snowpack," in *2022 52nd European Microwave Conference (EuMC)*, 2022, pp. 76–79. DOI: 10.23919/EuMC54642.2022.9924395.

[6] P. F. Espín-López, M. Lodigiani, M. Barbolini, F. Dell'Acqua, L. Silvestri, and M. Pasian, "Proof-of-concept for a ground-based dual-receiver radar architecture to estimate snowpack parameters for wet snow," *IEEE Transactions on Geoscience and Remote Sensing*, vol. 60, pp. 1–9, 2022. DOI: 10.1109/TGRS.2021.3103834.

[7] M. Lodigiani, L. Silvestri, R. Barella, C. Marin, and M. Pasian, "Monitoring wet snow with a dual-receiver radar architecture: Preliminary experimental results," in *2023 17th European Conference on Antennas and Propagation (EuCAP)*, 2023, pp. 1–4. DOI: 10.23919/EuCAP57121.2023.10133469.

[8] S. Planton, "Annex iii: Glossary," *Climate change*, pp. 1447–1465, 2013.

[9] J. Key, *Integrated global observing strategy cryosphere theme report*, Nov. 2007.

[10] R. Barry and T. Y. Gan, *The Global Cryosphere: Past, Present and Future*. Cambridge University Press, 2011. DOI: 10.1017/CBO9780511977947.

[11] A. Ohmura, "Chapter 3 - snow and ice in the climate system," in *Snow and Ice-Related Hazards, Risks, and Disasters (Second Edition)*, ser. Hazards and Disasters Series, W. Haeberli and C. Whiteman, Eds., Second Edition, Elsevier, 2021, pp. 73–92. DOI: 10.1016/B978-0-12-817129-5.00011-1.

[12] G. Hornberger and T. C. Winter, "Snow and ice," in *Encyclopedia of Inland Waters*, G. E. Likens, Ed., Academic Press, 2009, p. 773. DOI: 10.1016/B978-012370626-3.00013-2.

[13] L. Stucchi, G. M. Bombelli, A. Bianchi, and D. Bocchiola, "Hydropower from the alpine cryosphere in the era of climate change: The case of the sabbione storage plant in italy," *Water*, vol. 11, no. 8, 2019. DOI: 10.3390/w11081599.

[14] T. Duratorre, G. M. Bombelli, G. Menduni, and D. Bocchiola, "Hydropower potential in the alps under climate change scenarios. the chavonne plant, val d'aosta," *Water*, vol. 12, no. 7, 2020. DOI: 10.3390/w12072011.

[15] L. Kai-Lu, C. Ren-Sheng, L. Guo-Hua, and Y. Yong, "Cryosphere water resources supply function and service in china," *Advances in Climate Change Research*, vol. 13, no. 3, pp. 408–420, 2022. DOI: https://doi.org/10.1016/j.accre.2022.03.004.

[16] A. Instanes, V. Kokorev, R. Janowicz, O. Bruland, K. Sand, and T. Prowse, "Changes to freshwater systems affecting arctic infrastructure and natural resources," *Journal of Geophysical Research: Biogeosciences*, vol. 121, no. 3, pp. 567–585, 2016. DOI: 10.1002/2015JG003125.

[17] Y. Qin, J. Abatzoglou, S. Siebert, *et al.*, "Agricultural risks from changing snowmelt," *Nature Climate Change*, vol. 10, May 2020. DOI: 10.1038/s41558-020-0746-8.

[18] J. Hardelin and J. Lankoski, "Climate change, water and agriculture: Challenges and adaptation strategies," *EuroChoices*, vol. 14, no. 2, pp. 10–15, 2015. DOI: 10.1111/1746-692X.12085.

[19] "The present status of snow-surveying and irrigation water-supply forecasting in the west," *Eos, Transactions American Geophysical Union*, vol. 18, no. 2, pp. 603–607, 1937. DOI: 10.1029/TR018i002p00603.

[20] P. Lemke, J. Ren, R. B. Alley, *et al.*, *Observations: Changes in snow, ice and frozen ground*, 2007.

[21] M. Zemp, M. Huss, E. Thibert, *et al.*, "Global glacier mass changes and their contributions to sea-level rise from 1961 to 2016," *Nature*, vol. 568, Apr. 2019. DOI: 10.1038/s41586-019-1071-0.

[22] L. S. Taylor, D. J. Quincey, M. W. Smith, C. A. Baumhoer, M. McMillan, and D. T. Mansell, "Remote sensing of the mountain cryosphere: Current capabilities and future opportunities for research," *Progress in Physical Geography: Earth and Environment*, vol. 45, no. 6, pp. 931–964, 2021. DOI: 10.1177/03091333211023690.

[23] L. Tsang, M. Durand, C. Derksen, *et al.*, "Review article: Global monitoring of snow water equivalent using high-frequency radar remote sensing," *The Cryosphere*, vol. 16, no. 9, pp. 3531–3573, 2022. DOI: 10.5194/tc-16-3531-2022.

[24] S. Thakur, E. Donini, F. Bovolo, and L. Bruzzone, "An approach to the assessment of detectability of subsurface targets in polar ice from satellite radar sounders," *IEEE Transactions on Geoscience and Remote Sensing*, vol. 60, pp. 1–21, 2022. DOI: 10.1109/TGRS.2021.3119047.

[25] H. Rott, S. Scheiblauer, J. Wuite, *et al.*, "Penetration of interferometric radar signals in antarctic snow," *The Cryosphere*, vol. 15, no. 9, pp. 4399–4419, 2021. DOI: 10.5194/tc-15-4399-2021.

[26] J. Eppler, B. Rabus, and P. Morse, "Snow water equivalent change mapping from slope-correlated synthetic aperture radar interferometry (insar) phase variations," *The Cryosphere*, vol. 16, no. 4, pp. 1497–1521, 2022. DOI: 10.5194/tc-16-1497-2022.

[27] D. Dyre Oliver, J. Mark A., M. Andrew R., *et al.*, "Ground-based radar interferometry for monitoring of landfast sea ice dynamics," *Cold Regions Science and Technology*, vol. 210, p. 103 779, 2023. DOI: 10.1016/j.coldregions.2023.103779.

[28] R. T. Tonboe, V. Nandan, J. Yackel, S. Kern, L. T. Pedersen, and J. Stroeve, "Simulated ka- and ku-band radar altimeter height and freeboard estimation on snow-covered arctic sea ice," *The Cryosphere*, vol. 15, no. 4, pp. 1811–1822, 2021. DOI: 10.5194/tc-15-1811-2021.

[29] R. L. Tilling, A. Ridout, and A. Shepherd, "Estimating arctic sea ice thickness and volume using cryosat-2 radar altimeter data," *Advances in Space Research*, vol. 62, no. 6, pp. 1203–1225, 2018. DOI: 10.1016/j.asr.2017.10.051.

[30] B. Rekioua, M. Davy, L. Ferro-Famil, and S. Tebaldini, "Snowpack permittivity profile retrieval from tomographic sar data," *Comptes Rendus Physique*, vol. 18, no. 1, pp. 57–65, 2017. DOI: https://doi.org/10.1016/j.crhy.2015.12.016.

[31] F. Banda, J. Dall, S. Tebaldini, and F. Rocca, "Tomographic sar analysis of subsurface ice structure in greenland: First results," in *2013 IEEE International Geoscience and Remote Sensing Symposium - IGARSS*, 2013, pp. 236–239. DOI: 10.1109/IGARSS.2013.6721135.

[32] F. Koch, P. Henkel, F. Appel, *et al.*, "Retrieval of snow water equivalent, liquid water content, and snow height of dry and wet snow by combining gps signal attenuation and time delay," *Water Resources Research*, vol. 55, no. 5, pp. 4465–4487, 2019. DOI: 10.1029/2018WR024431.

[33] A. Capelli, F. Koch, P. Henkel, *et al.*, "Gnss signal-based snow water equivalent determination for different snowpack conditions along a steep elevation gradient," *The Cryosphere*, vol. 16, no. 2, pp. 505–531, 2022. DOI: 10.5194/tc-16-505-2022.

[34] G. Hajnsek I. and Parrella, A. Marino, T. Eltoft, M. Necsoiu, L. Eriksson, and M. Watanabe, "Cryosphere applications," in *Polarimetric Synthetic Aperture Radar: Principles and Application*, Y.-L. Hajnsek I. and Desnos, Ed. Springer International Publishing, 2021, pp. 179–213. DOI: 10.1007/978-3-030-56504-6_4.

[35] N. Dematteis, G. Luzi, D. Giordan, F. Zucca, and P. Allasia, "Monitoring alpine glacier surface deformations with gb-sar," *Remote Sensing Letters*, vol. 8, pp. 947–956, Oct. 2017. DOI: 10.1080/2150704X.2017.1335905.

[36] M. Pasian, M. Barbolini, F. Dell'Acqua, P. F. Espín-López, and L. Silvestri, "Snowpack monitoring using a dual-receiver radar architecture," *IEEE Transactions on Geoscience and Remote Sensing*, vol. 57, no. 2, pp. 1195–1204, 2019. DOI: 10.1109/TGRS.2018.2865180.

[37] P. F. Espin-Lopez, M. Pasian, M. Barbolini, and F. Dell'Acqua, "Snow cover monitoring using microwave radars: Dielectric characterization, fabrication, and testing of a synthetic snowpack," in *IGARSS 2018 - 2018 IEEE International Geoscience and Remote Sensing Symposium*, 2018, pp. 5097–5100. DOI: 10.1109/IGARSS.2018.8517649.

[38] M. Lodigiani, N. Delmonte, and M. Pasian, "A novel pifa antennas design with capacitive load for glacier monitoring applications," in *2022 16th European Conference on Antennas and Propagation (EuCAP)*, 2022, pp. 1–3. DOI: 10.23919/EuCAP53622.2022.9769261.

[39] C. Rowell and R. D. Murch, "A capacitively loaded pifa for compact mobile telephone handsets," *IEEE Transactions on Antennas and Propagation*, vol. 45, no. 5, pp. 837–842, 1997. DOI: 10.1109/8.575634.

[40] R. Fragnier, L. Feat, R. Contreres, *et al.*, "Collocated compact uhf and l-band antenna for nanosatellite argos program," in *2019 13th European Conference on Antennas and Propagation (EuCAP)*, 2019, pp. 1–4.

[41] O. Louhichi, D. Bechevet, and S. Tedjini, "Methodology for uhf pifa design in harsh environment," in *2011 IEEE International Symposium on Antennas and Propagation (APSURSI)*, 2011, pp. 1201–1204. DOI: 10.1109/APS.2011.5996500.

[42] C. Y. Chiu, K. M. Shum, and C. H. Chan, "A tunable via-patch loaded pifa with size reduction," *IEEE Transactions on Antennas and Propagation*, vol. 55, no. 1, pp. 65–71, 2007. DOI: 10.1109/TAP.2006.888389.

[43] C. Fierz, R. L. Armstrong, Y. Durand, *et al.*, *The International Classification for Seasonal Snow on the Ground* (Technical documents in hydrology, no. 83, IACS contribution no.1). UNESCO-IHP, Paris, 2009.

[44] T. C. Grenfell and S. G. Warren, "Representation of a nonspherical ice particle by a collection of independent spheres for scattering and absorption of radiation," *Journal of Geophysical Research*, vol. 104, no. D24, pp. 31 697–31 709, 1999. DOI: 10.1029/1999JD900496.

[45] T. Aoki, A. Hachikubo, and M. Hori, "Effects of snow physical parameters on shortwave broadband albedos," *Journal of Geophysical Research*, vol. 108, no. D19, p. 4616, 2003. DOI: 10.1029/2003JD003506.

[46] C. Mätzler, "Relation between grain size and correlation length of snow," *Journal of Glaciology*, vol. 48, no. 162, pp. 461–466, 2002. DOI: 10.3189/172756502781831287.

[47] A. Denoth, "Snow dielectric measurements," *Advances in Space Research*, vol. 9, no. 1, pp. 233–243, 1989. DOI: 10.1016/0273-1177(89)90491-2.

[48] C. Matzler, "Microwave permittivity of dry snow," *IEEE Transactions on Geoscience and Remote Sensing*, vol. 34, no. 2, pp. 573–581, 1996. DOI: 10.1109/36.485133.

[49] T. Takeuchi, Y. Nohguchi, K. Kawashima, and K. Izumi, "Measurement of snow-hardness distribution," *Annals of Glaciology*, vol. 26, pp. 27–30, 1998. DOI: 10.3189/1998AoG26-1-27-30.

[50] M. de Quervain, "Die festigkeitseigenschaften der schneedecke und ihre messung," *Geofisica Pura e Applicata*, vol. 18, pp. 179–191, 1950. DOI: 10.1007/BF02000325.

[51] K. Kawashima, T. Endo, and Y. Takeuchi, "A portable calorimeter for measuring liquid-water content of wet snow," *Annals of Glaciology*, vol. 26, pp. 103–106, 1998. DOI: 10.3189/1998AoG26-1-103-106.

[52] H. S. Boyne and D. J. Fisk, "A laboratory comparison of field techniques for measurement of the liquid water fraction of snow," *CRREL Special Report*, vol. 90, no. 3, 1990.

[53] A. Denoth, A. Foglar, P. Weiland, *et al.*, "A comparative study of instruments for measuring the liquid water content of snow," *Journal of Applied Physics*, vol. 56, no. 7, pp. 2154–2160, 1984. DOI: 10.1063/1.334215.

[54] D. McClung and P. Schaerer, *The Avalanche Handbook*. Mountaineers Books, 2006.

[55] B. J. Mason, "Snow crystals. ukichiro nakaya. harvard university press," *Journal of Glaciology*, vol. 2, no. 16, p. 444, 1954. DOI: 10.3189/S0022143000016956.

[56] L. Kenneth G., "Explaining the formation of thin ice crystal plates with structure-dependent attachment kinetics," *Journal of Crystal Growth*, vol. 258, no. 1, pp. 168–175, 2003. DOI: 10.1016/S0022-0248(03)01496-9.

[57] L. A. Barrie, "Snow formation and processes in the atmosphere that influence its chemical composition," in *Seasonal Snowpacks*, T. D. Davies, M. Tranter, and H. G. Jones, Eds., Springer Berlin Heidelberg, 1991, pp. 1–20. DOI: 10.1007/978-3-642-75112-7_1.

[58] Y. Furukawa and J. Wettlaufer, "Snow and ice crystals," *Physics Today - PHYS TODAY*, vol. 60, Dec. 2007. DOI: 10.1063/1.2825081.

[59] V. Tonchev and V. Stoyanova, "Snow crystals: A case study in spontaneous structure formation," *Crystallography Reviews*, vol. 28, no. 4, pp. 298–300, 2022. DOI: 10.1080/0889311X.2022.2104839.

[60] A. Carbone, B. M. Chiaia, B. Frigo, and C. Türk, "Snow metamorphism: A fractal approach," *Phys. Rev. E*, vol. 82, p. 036 103, 3 2010. DOI: 10.1103/PhysRevE.82.036103.

[61] R. A. Sommerfeld and E. LaChapelle, "The classification of snow metamorphism," *Journal of Glaciology*, vol. 9, no. 55, pp. 3–18, 1970. DOI: 10.3189/S0022143000026757.

[62] B. R. Pinzer and M. Schneebeli, "Snow metamorphism under alternating temperature gradients: Morphology and recrystallization in surface snow," *Geophysical Research Letters*, vol. 36, no. 23, 2009. DOI: doi.org/10.1029/2009GL039618.

[63] R. Brown, P. Satyawali, M. Lehning, and P. Bartelt, "Modeling the changes in microstructure of snow during metamorphism," *Cold Regions Science and Technology*, vol. 33, no. 2, pp. 91–101, 2001. DOI: 10.1016/S0165-232X(01)00032-5.

[64] M. Hallikainen, F. Ulaby, and M. Abdelrazik, "Dielectric properties of snow in the 3 to 37 ghz range," *IEEE Transactions on Antennas and Propagation*, vol. 34, no. 11, pp. 1329–1340, 1986. DOI: 10.1109/TAP.1986.1143757.

[65] A. Denoth, "The pendular-funicolar liquid transition and snow metamorphism," *Journal of Glaciology*, vol. 28, no. 99, pp. 357–364, 1982. DOI: 10.3189/S0022143000011692.

[66] A. Denoth, "Wet snow pendular regime: The amount of water in ring-shaped configurations," *Cold Regions Science and Technology*, vol. 30, no. 1-3, pp. 13–18, 1999. DOI: 10.1016/S0165-232X(99)00007-5.

[67] J. H. Bradford, J. T. Harper, and J. Brown, "Complex dielectric permittivity measurements from ground-penetrating radar data to estimate snow liquid water content in the pendular regime," *Water Resources Research*, vol. 45, no. 8, 2009. DOI: 10.1029/2008WR007341.

[68] S. Ivy-Ochs, "Glacier variations in the european alps at the end of the last glaciation," *Cuadernos de Investigación Geográfica*, vol. 41, no. 2, pp. 295–315, 2015. DOI: 10.18172/cig.2750.

[69] C. Wirsig, J. Zasadni, M. Christl, N. Akçar, and S. Ivy-Ochs, "Dating the onset of lgm ice surface lowering in the high alps," *Quaternary Science Reviews*, vol. 143, pp. 37–50, 2016. DOI: 10.18172/cig.2750.

[70] G. Monegato, G. Scardia, I. Hajdas, F. Rizzini, and A. Piccin, *Scientific Reports*,

[71] J. Seguinot, S. Ivy-Ochs, G. Jouvet, M. Huss, M. Funk, and F. Preusser, "Modelling last glacial cycle ice dynamics in the alps," *The Cryosphere*, vol. 12, no. 10, pp. 3265–3285, 2018. DOI: 10.5194/tc-12-3265-2018.

[72] J. Sjolte, F. Adolphi, B. M. Vinther, *et al.*, "Seasonal reconstructions coupling ice core data and an isotope-enabled climate model – methodological implications of seasonality, climate modes and selection of proxy data," *Climate of the Past*, vol. 16, no. 5, pp. 1737–1758, 2020. DOI: 10.5194/cp-16-1737-2020.

[73] C. Buizert, "The ice core gas age-ice age difference as a proxy for surface temperature," *Geophysical Research Letters*, vol. 48, no. 20, e2021GL094241, 2021. DOI: https://doi.org/10.1029/2021GL094241.

[74] H. Bader, "The significance of air bubbles in glacier ice," *Journal of Glaciology*, vol. 1, no. 8, pp. 443–451, 1950. DOI: 10.3189/S002214300001279X.

[75] A. Fountain and J. Walder, "Water flow through temperate glaciers," *Reviews of Geophysics*, vol. 36, Aug. 1998. DOI: 10.1029/97RG03579.

[76] T. Irvine-Fynn and B. Hubbard, "Glacier hydrology and runoff," in Mar. 2017, pp. 1–18, ISBN: 9780470659632. DOI: 10.1002/9781118786352.wbieg0709.

[77] M. Bennett, "Glaciers and glaciation by benn, d. i. and evans, d. j. a.," *Boreas*, vol. 40, Jul. 2011. DOI: 10.1111/j.1502-3885.2011.00212.x.

[78] R. Alley, "K.m. cuffey and w.s.b. paterson. 2010. the physics of glaciers. fourth edition. amsterdam, etc., academic press.," *Journal of Glaciology*, vol. 57, no. 202, pp. 383–384, 2011. DOI: 10.3189/002214311796405906.

[79] T. Schultz, R. Muller, D. Gross, and A. Humbert, "Modelling the transformation from snow to ice based on the underlying sintering process," *PAMM*, vol. 20, no. 1, e202000212, 2021. DOI: 10.1002/pamm.202000212.

[80] J. Geissler, C. Mayer, J. Jubanski, U. Munzer, and F. Siegert, "Analyzing glacier retreat and mass balances using aerial and uav photogrammetry in the otztal alps, austria," *The Cryosphere*, vol. 15, no. 8, pp. 3699–3717, 2021. DOI: 10.5194/tc-15-3699-2021.

[81] E. Berthier, H. Vadon, D. Baratoux, *et al.*, "Surface motion of mountain glaciers derived from satellite optical imagery," *Remote Sensing of Environment*, vol. 95, pp. 14–28, Mar. 2005. DOI: 10.1016/j.rse.2004.11.005.

[82] J. Corripio, "Snow surface albedo estimation using terrestrial photography," *International Journal of Remote Sensing - INT J REMOTE SENS*, vol. 25, Dec. 2004. DOI: 10.1080/01431160410001709002.

[83] E. Heucke, "A light portable steam-driven ice drill suitable for drilling holes in ice and firn," *Geografiska Annaler: Series A, Physical Geography*, vol. 81, no. 4, pp. 603–609, 1999. DOI: https://doi.org/10.1111/1468-0459.00088.

[84] G. Church, A. Bauder, M. Grab, and H. Maurer, "Ground-penetrating radar imaging reveals glacier's drainage network in 3d," *The Cryosphere*, vol. 15, no. 8, pp. 3975–3988, 2021. DOI: 10.5194/tc-15-3975-2021.

[85] H. Hausmann and M. Behm, "Imaging the structure of cave ice by ground-penetrating radar," *The Cryosphere*, vol. 5, no. 2, pp. 329–340, 2011. DOI: 10.5194/tc-5-329-2011.

[86] A. Neven, V. Dall'Alba, P. Juda, J. Straubhaar, and P. Renard, "Ice volume and basal topography estimation using geostatistical methods and ground-penetrating radar measurements: Application to the tsanfleuron and scex rouge glaciers, swiss alps," *The Cryosphere*, vol. 15, no. 11, pp. 5169–5186, 2021. DOI: 10.5194/tc-15-5169-2021.

[87] C. Colombero, C. Comina, E. De Toma, D. Franco, and A. Godio, "Ice thickness estimation from geophysical investigations on the terminal lobes of belvedere glacier (nw italian alps)," *Remote Sensing*, vol. 11, no. 7, 2019. DOI: 10.3390/rs11070805.

[88] C. Ogier, D.-J. van Manen, H. Maurer, *et al.*, "Ground penetrating radar in temperate ice: Englacial water inclusions as limiting factor for data interpretation," *Journal of Glaciology*, 2023. DOI: 10.1017/jog.2023.68.

[89] T. Murray, A. Booth, and D. M. Rippin, "Water-content of glacier-ice: Limitations on estimates from velocity analysis of surface ground-penetrating radar surveys," *Journal of Environmental and Engineering Geophysics*, vol. 12, no. 1, pp. 87–99, 2007. DOI: 10.2113/JEEG12.1.87.

[90] K. Pavelka, J. Šedina, E. Matouskova, I. Hlaváčová, and W. Korth, "Examples of different techniques for glaciers motion monitoring using insar and rpas," *European Journal of Remote Sensing*, vol. 52, pp. 219–232, Mar. 2019. DOI: 10.1080/22797254.2018.1559001.

[91] G. d. Q. Robin, S. Evans, and J. T. Bailey, "Interpretation of radio echo sounding in polar ice sheets," *Philosophical Transactions of the Royal Society of London. Series A, Mathematical and Physical Sciences*, vol. 265, no. 1166, pp. 49–64, 1969. DOI: 10.1098/rsta.1969.0063.

[92] G. d. Q. Robin, "Radio-echo sounding: Glaciological interpretations and applications," *Journal of Glaciology*, vol. 15, no. 73, pp. 49–64, 1975. DOI: 10.3189/S0022143000034262.

[93] K. Austin, J. G. Anthony, and M. M. Rexford, "The in-situ dielectric constant of polar firn revisited," *Cold Regions Science and Technology*, vol. 23, no. 3, pp. 245–256, 1995. DOI: 10.1016/0165-232X(94)00016-Q.

[94] O. Eisen, U. Nixdorf, F. Wilhelms, and H. Miller, "Electromagnetic wave speed in polar ice: Validation of the common-midpoint technique with high-resolution dielectric-profiling and gamma-density measurements," *Annals of Glaciology*, vol. 34, pp. 150–156, 2002. DOI: 10.3189/172756402781817509.

[95] M. Lodigiani, L. Silvestri, and M. Pasian, "Glacier monitoring with dual-receiver radar architecture: Preliminary experimental results," in *IGARSS 2022 - 2022 IEEE International Geoscience and Remote Sensing Symposium*, 2022, pp. 3794–3797. DOI: 10.1109/IGARSS46834.2022.9883574.

[96] H. Vickers, E. Malnes, and M. Eckerstorfer, "A synthetic aperture radar based method for long term monitoring of seasonal snowmelt and wintertime rain-on-snow events in svalbard," *Frontiers in Earth Science*, vol. 10, 2022. DOI: 10.3389/feart.2022.868945.

[97] F. Techel and C. Pielmeier, "Point observations of liquid water content in wet snow - investigating methodical, spatial and temporal aspects," *The Cryosphere*, vol. 5, no. 2, pp. 405–418, 2011. DOI: 10.5194/tc-5-405-2011.

[98] C. Marin, G. Bertoldi, V. Premier, *et al.*, "The relationship between the multi-temporal sentinel-1 backscattering and the snow melting dynamics in alpine regions," in *2019 13th European Conference on Antennas and Propagation (EuCAP)*, 2019, pp. 1–5.

[99] C. Marin, G. Bertoldi, V. Premier, *et al.*, "Use of sentinel-1 radar observations to evaluate snowmelt dynamics in alpine regions," *The Cryosphere*, vol. 14, pp. 935–956, 2020. DOI: 10.5194/tc-14-935-2020.

[100] M. Pasian, P. F. Espín-López, V. Premier, C. Notarnicola, and C. Marin, "Identification of multi-temporal snow melting patterns with microwave radars," in *2020 14th European Conference on Antennas and Propagation (EuCAP)*, 2020, pp. 1–5. DOI: 10.23919/EuCAP48036.2020.9135545.

[101] M. Lehning, P. Bartelt, B. Brown, T. Russi, U. Stöckli, and M. Zimmerli, "Snowpack model calculations for avalanche warning based upon a network of weather and snow stations," *Cold Regions Science and Technology*, vol. 30, pp. 145–157, Dec. 1999. DOI: 10.1016/S0165-232X(99)00022-1.

[102] M. Lehning, C. Fierz, B. Brown, and B. Jamieson, "Modeling snow instability with the snow-cover model snowpack," *Annals of Glaciology*, vol. 38, pp. 331–338, 2004. DOI: 10.3189/172756404781815220.

[103] K. G. Kjelgård and T. S. Lande, "Evaluation of uwb radar module for snow water equivalent monitoring," in *2022 52nd European Microwave Conference (EuMC)*, 2022, pp. 87–90. DOI: 10.23919/EuMC54642.2022.9924383.

[104] J. H. H. Eriksrød, K. G. Kjelgård, and T. S. Lande, "Complex dielectric constant of wet snow using bi-static synthetic aperture radar," in *2020 14th European Conference on Antennas and Propagation (EuCAP)*, 2020, pp. 1–4. DOI: 10.23919/EuCAP48036.2020.9135720.

[105] J. H. H. Eriksrød, K. G. Kjelgård, and T. B. Lande, "A 3d-printed saddle reflector for upwards-looking bi-static sar snow radar," in *2019 16th European Radar Conference (EuRAD)*, 2019, pp. 97–100.

[106] J. H. H. Eriksrød, K. G. Kjelgård, and T. S. Lande, "In-situ snowpack inspection using bi-static radar," in *2019 13th European Conference on Antennas and Propagation (EuCAP)*, 2019, pp. 1–5.

[107] J. H. H. Eriksrød, K. G. Kjelgård, M. Tommer, J. F. Burkhart, and T. Lande, "Bi-static environmental sar radar imager," in *2017 IEEE Nordic Circuits and Systems Conference (NORCAS): NORCHIP and International Symposium of System-on-Chip (SoC)*, 2017, pp. 1–6. DOI: 10.1109/NORCHIP.2017.8124979.

Acknowledgments

Monitoring of the cryosphere is fundamental for understanding climatic dynamics and predicting impacts on our planet. This is important not only from a climate change perspective but also in terms of hydrology, tourism and risk management. In order to have a complete view of the cryospheric situation, merging together the results from different type of analysis is needed. For this reason, collaborations with other research institutes, universities, or specialized organization is fundamental.
During these last three years of Ph.D., my team and I have the opportunity to collaborate with a lot of Italian colleagues in the framework of the Agenzia Spaziale Europea (ASI) project: "CRIOSAR: Applicazioni SAR multifrequenza alla criosfera", grant agreement n. ASIN.2021-12-U.0. In particular:

- Carlo Marin, Riccardo Barella, Valentina Premier, Riccardo Parin and Claudia Notarnicola from the Institute of Earth Observation - Eurac Research, Bolzano, South Tyrol

- Biagio Di Mauro, Roberto Garzonio, Roberto Colombo from UNIMIB and from the Institute of Polar Science (ISP) of the National Research Council (CNR)

- the Institute of Applied Physics (IFAC) "Nello Carrara" and the Institute for electromagnetic sensing of the environment (IREA), part of CNR

The wet snow campaign in Sodankylä-Tähtelä, Finland, has received the Transnational Access from the European Union's Horizon 2020 project INTERACT, under grant agreement No. 871120. In particular, Juha Lemmetyinen (FMI), Anna Kontu (FMI-ARC) and Leena Leppänen (University of Lapland) helped us from different perspectives, organizing the access to the facilities and giving tracks on the scientific activities. A particular thank also to Roberta Pirazzini (FMI), for the work done together and for the ospitality at the Arctic site.
Glacier monitoring campaigns were done in collaboration with Fondazione Montagna Sicura -Fondation Montagne Sûre, a research institute of Courmayeur, Aosta Valley, in particular with Fabrizio Troilo, Paolo Perret, Jean Pierre Fosson. Moreover, also Francesco Zucca (UNIPV) collaborates in this project.
The work done at the University of Oslo was in the framework of the Erasmus+ Traineeship program. In particular I would like to thank my supervisor there Kristian G. Kjelgård and Tor Sverre Lande.

The work reported in this thesis was done together with my teammates: Lorenzo Silvestri (University of Pavia UNIPV), Pedro Fidel Espin-Lopez (Centre Tecnològic de Telecomunicacions de Catalunya CTTC), Nicolò Delmonte (UNIPV) and my supervisor Marco Pasian.